Catalysis of the electrochemical water oxidation to oxygen

Proefschrift

ter verkrijging van

de graad van Doctor aan de Universiteit Leiden,

op gezag van Rector Magnificus prof. mr. C. J. J. M. Stolker,

volgens besluit van het College voor Promoties

te verdedigen op donderdag 19 november 2015

klokke 11.15 uur

door

Oscar Alfonso Díaz Morales

geboren te Caracas in 1984

Promotiecommissie:

Promotor:	Prof. Dr. M.T.M. Koper
Co-promotor:	Dr. F. Calle-Vallejo
Overige Leden:	Prof. Dr. J. Brouwer
	Prof. Dr. Y. Shao-Horn (Massachusetts Institute of Technology)
	Prof. Dr. J. Reek (Universiteit van Amsterdam)
	Dr. W. Smith (Technische Universiteit Delft)
	Prof. Dr. H.de Groot
	Dr. D. Hetterscheid

ISBN: 978-94-6259-913-0

This research was sponsored by the BioSolar Cells open innovation consortium, supported by the Dutch Ministry of Economic Affairs, Agriculture and Innovation.

A Hilda Morales

Porque estas páginas llevan impreso el sudor de tu frente, mamá.

Table of Contents

1.Introduction 1

1.1. Overview 1

1.2. Electrocatalysis for the water oxidation reaction 2

1.3. Outline of this thesis 5

REFERENCES 7

2.Evidences for gold oxide decomposition mechanism during the electrochemical water oxidation 9

2.1. Introduction 10

2.2. Experimental and Computational Section 11

2.2.1. Experimental 11

2.2.2. Computational 12

2.3. Results 14

2.3.1. Experimental results 14

2.3.2. Brief summary of literature on the surface oxidation of gold 21

2.3.3. Computational results 23

2.4. Discussion 29

2.5. Conclusions 31

2.6. Acknowledgments 31

REFERENCES 32

3.Electrochemical and spectroelectrochemical characterization of an iridium-based molecular catalyst for oxygen evolution: turnover frequencies, stability and electrolyte effects 35

3.1. Introduction 36

3.2. Experimental Section 39

3.3. Results and Discussion 42

3.3.1. Effect of electrolyte anions 42

3.3.2. Effect of the pH on the catalytic activity of the molecular complex 46

3.3.3. The stability of the molecular catalyst: SERS and OLEMS experiments. 49
3.4. Conclusions 53
3.5. Acknowledgments 53
REFERENCES 54
4.Guidelines for the rational design of nickel – based double hydroxide electrocatalysts for the oxygen evolution reaction 59
4.1. Introduction 60
4.2. Computational and Experimental Details 61
4.2.1. DFT calculations 61
4.2.2. Chemicals 64
4.2.3. Cleaning procedure 65
4.2.4. Synthesis of the Nickel Double Hydroxides 65
4.2.5. Characterization 66
4.3. Results and Discussion 67
4.4. Conclusions 76
4.5. Acknowledgments 77
REFERENCES 77
5.The importance of nickel oxyhydroxide deprotonation on its activity towards electrochemical water oxidation 81
5.1. Introduction 82
5.2. Experimental Section 83
5.3. Results and Discussion 86
5.4. Conclusions 96
5.5. Acknowledgments 96
REFERENCES 96
6.Iridium-based double perovskites for efficient water oxidation in acid media 101
6.1. Introduction 102
6.2. Experimental Section 104
6.2.1. Chemicals 104

6.2.2. Synthesis and characterization of the iridium-based catalysts 104
6.2.3. Electrochemical experiments 104
6.3. Results and Discussion 106
6.4. Conclusions 114
6.5. Acknowledgments 114
REFERENCES 114
Summary 119
Samenvatting 123
List of publications 127
Curriculum Vitae 129
Appendix A: Supplementary Material for Chapter 2 131
Appendix B: Supplementary Material for Chapter 3 133
Appendix C: Supplementary Material for Chapter 4 141
Appendix D: Supplementary Material for Chapter 5 155
Appendix E: Supplementary Material for Chapter 6 161

Chapter 1

Introduction

1.1. Overview

This work was performed in the framework of the project C1.8 of the BioSolar Cells open innovation consortium that focuses on studying the mechanism of water oxidation catalysis on both oxide and molecular catalysts. The fundamental insights obtained from the water oxidation electrocatalysis can be potentially used to develop devices to convert solar energy into fuels (artificial photosynthesis).

To develop our fundamental understanding of water oxidation, this thesis presents a (spectro)electrochemical study of the water oxidation reaction (also known as oxygen evolution reaction, OER), which is the anodic reaction in the water splitting process ($H_2O \rightarrow H_2 + 1/2O_2$).[1-4] This process will have important economic and environmental implications in the near future because it is one of the most promising alternatives to store solar energy, which is one of the fundamental steps in the development of a sustainable energy-based society.[1,3,5-8] The sun is by far the largest exploitable energy resource, which irradiates the earth in one hour with enough power ($4.3x10^{21}$ J) to supply the needs of the whole planet in one year.[1] However, the daily, seasonal and regional intermittence of solar light makes the large scale utilization of this resource unfeasible.[1,3,8,9] Therefore, in a society where solar energy is meant to be the major powering source, there must exist efficient technologies to store the irradiated solar power and that can straightforwardly dispatch it to the end user on demand.[1,6,10]

Conversion of solar energy into fuels (hydrocarbons, alcohols, hydrogen, etc.) is a very attractive approach to perform the solar energy storage, which can be potentially integrated in a distribution system to overcome the availability problem.[1,3,5,6] The water splitting process plays a central role in the solar-to-fuel conversion process because in all

approaches for the generation of solar fuels, water is oxidized to oxygen releasing protons that in combination with the photo-generated electrons are used to drive the fuel production.[1,3,5,6,9-11] This clearly points out the importance of the water splitting process for the solar energy-to-fuel conversion process towards the development of a sustainable society, and underscores the relevance of the studies performed in this thesis.

The solar-to-fuel conversion requires the oxidation of water to oxygen. However, the kinetics for this reaction is slow, reducing significantly the efficiency of the generation of fuels.[2,4,5,9,11] The next section will revisit the thermodynamic reasons behind the slow kinetics of the water oxidation reaction and will outline the research challenges in order to develop better catalysts.

1.2. Electrocatalysis for the water oxidation reaction

The oxidation of water to oxygen is a complex electrochemical reaction involving the transfer of four electrons and four protons, and the most accepted mechanism through which the reaction proceeds is summarized in equations (1) – (4) for the reaction occurring in acid media, and in equations (5) – (8) for the case of alkaline media.[4,12,13]

In acid media:

$$H_2O + * \rightarrow OH_{ads} + H^+ + e^- \quad (1)$$

$$OH_{ads} \rightarrow O_{ads} + H^+ + e^- \quad (2)$$

$$O_{ads} + H_2O \rightarrow OOH_{ads} + H^+ + e^- \quad (3)$$

$$OOH_{ads} \rightarrow O_2 + H^+ + e^- + * \quad (4)$$

In alkaline media:

$$OH^- + * \rightarrow OH_{ads} + e^- \quad (5)$$

$$OH_{ads} + OH^- \rightarrow O_{ads} + H_2O + e^- \quad (6)$$

$$O_{ads} + OH^- \rightarrow OOH_{ads} + e^- \quad (7)$$

$$OOH_{ads} + OH^- \rightarrow O_2 + H_2O + e^- + * \quad (8)$$

The * in equations (1) – (8) denotes a catalytically active surface site.

Koper revisited the thermodynamic aspects that limit the kinetics of the oxygen reduction reaction (ORR) and its anodic counterpart, the oxygen evolution reaction.[14] His major conclusion was that when all the separate steps involved in the reaction mechanism have the same zero free energy, the overall reaction may proceed at the thermodynamic equilibrium potential of 1.23 V vs. RHE. However, it is known that the binding energies of the intermediates involved in the ORR/OER are strongly correlated,[12,13] and the difference between the binding energy of the OH intermediate and the OOH is a constant value (*ca.* 3.04 – 3.2 *eV*), that exceeds the ideal condition of 2.46 *eV*. This fact introduces a thermodynamic limitation that hinders the optimization process to sub-optimal catalysts with non-zero (thermodynamic) overpotential[14] as it is shown in Figure 1.

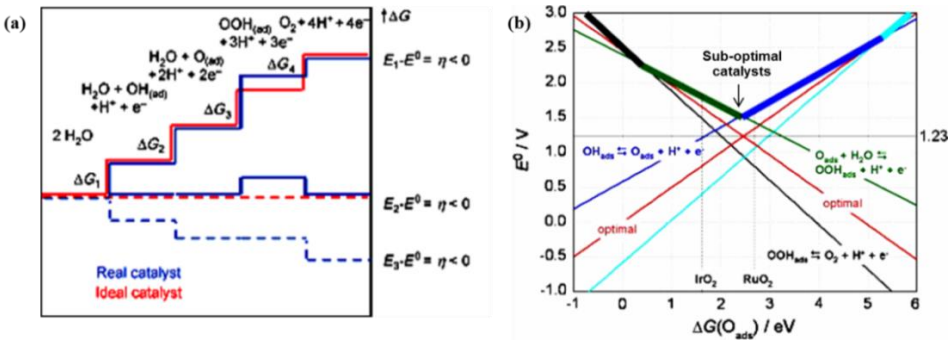

Figure 1. a) Chemisorption energy of the intermediates (horizontal lines) of the OER versus the reaction coordinate. Blue lines and red lines indicate energetics of a real (typical) catalyst and an ideal catalyst, respectively, at three different electrode potentials. Dashed lines indicate energetics at the electrode potential where all thermochemical barriers disappear ("thermochemical overpotential"); ΔG_i denotes the free reaction energy of the two elementary reaction steps. The red ideal case corresponds to a catalyst that can drive the reaction with zero (thermodynamic) overpotential. Figure adapted from reference 4. b) Plot of the equilibrium potentials for the reaction described in equations (1) – (4) for the OER in acid media as a function of the chemisorption energy of oxygen on the catalysts $\Delta G(O_{ads})$. The relative positions of the best OER catalysts in acid media (RuO_2 and IrO_2) are shown as reference. Figure adapted from reference 14.

The major future challenge in electrocatalysis for OER and ORR is to find materials able to circumvent the thermodynamic scaling relationship between the reaction intermediates, in order to stabilize the hydroperoxo species without affecting the individual stabilities of the hydroxyl and oxygen. Man *et al*. have suggested the design of three-dimensional active sites that can further stabilize the OOH intermediates without affecting the other reactive species on the surface.[15] A recent joint theoretical-experimental work from the groups of Ktril and Rossmeisl reported an attempt to break the thermodynamic limitations for the OER reaction.[16] Their computational DFT results indicated that the incorporation of nickel or cobalt in the structure of RuO_2 catalysts activates a proton donor-acceptor functionality on the conventionally inactive bridge surface sites of the ruthenia, and this enhances the OER activity of RuO_2. The predicted OER onset potential for these compounds is in the range of 0.1 – 0.3 V. They prepared the Ni and Co modified RuO_2 materials and measured the activity for oxygen evolution, and their experimental results showed that the current densities attributed to OER at 1.6 V vs. RHE on the modified ruthenia can be up to 30-fold higher than the values measured on the unmodified material.

Electrocatalysts based on transition metal oxides are among the most extensively studied materials due to their inherent chemical stability under the working conditions for the water oxidation reaction.[4,17,18] Iridium and ruthenium oxides are the most active catalysts for the water oxidation reaction in acid media.[17,19,20] IrO_2 is the only one having long term stability for acid-based electrolysis, and it is the material of use for OER anodes in acid-based industrial processes. [21,22] However, iridium is one of the rarest metals on the earth so it is prohibitively expensive to be used for large-scale applications like solar light harvesting for the generation of sustainable energy. For the electrochemical oxidation of water in alkaline media there are cheaper alternatives to IrO_2, based on earth abundant 3d transition metal oxides, which have higher catalytic activity towards OER than the expensive iridium oxide option[19,23-27]. However, the lack of efficient separation membranes suitable to work in alkaline electrolyzers and the low conductivity of the electrolytes typically used in such devices reduces the efficiency of solar-to-fuel.

Molecular catalysts have also been used as OER catalysts, in an attempt to mimic the natural photosynthetic compounds.[4,11,28,29] These compounds are relatively easy to tailor both electronically and structurally to obtain fundamental understanding on how these factors affect the activity, which is not straightforward in the case of metal oxides. There are large number of compounds that can drive the water oxidation reaction at high rate, which translate into high values for the turnover frequency (TOF) and the turnover number (TON). Sun's group reported recently a family of ruthenium-based molecular compounds with a TOF of 300 mol O_2 $mol_{catalyst}^{-1}$ s^{-1}, which is one of the few molecular catalysts able to catalyze the OER at a comparable rate to the natural photosynthesis II system.[30] Actually, there is a great variety of molecular catalysts based on Ir, Mn, Fe, Co that can also drive the electrochemical water oxidation at relatively high rates.[28,29] One of the major drawbacks in the utilization of OER molecular catalysts is their high tendency to decompose during the process, leading to the formation of the corresponding metal oxide, which then acts as the real active catalyst towards OER.[11,29,31,32] Moreover, the OER activity of these compounds is typically measured by using sacrificial oxidants, which makes it difficult to properly define the OER overpotential, and complicates the definition of clear benchmarking criteria.

1.3. Outline of this thesis

This thesis addresses the various experimental factors affecting the kinetics of the water oxidation reaction, not only by looking at the catalyst but also by revisiting the role of the electrolyte in the reaction kinetics. Our approach allows us to propose some guidelines for the rational development of catalysts able to efficiently catalyze the electrochemical water oxidation reaction, both in acid and alkaline media.

We start in chapter 2 by a spectroelectrochemical study of the water oxidation reaction on gold electrodes in acid media, to understand the surface processes that take place in the metal oxide, prior the actual oxygen evolution, and to obtain insight about the role of the 3D structure of the oxide in the overall reaction. The results of this study allows us to propose a model for the oxygen evolution reaction where the gold oxide formed on the

electrode surface is not innocent in the electrocatalytic water oxidation, but decomposes to produce oxygen in the overall water oxidation process. Still, gold is a poor catalyst for the water oxidation, and hence it is used as electrode material to support the other OER catalysts studied in this thesis.

In chapter 3 we present a spectroelectrochemical study of the electrolyte influence on the OER activity of an iridium-based molecular catalyst immobilized on a gold electrode in acid media. This chapter shows a systematic way to correlate the OER activity measured in homogeneous catalysis experiments with the activity of heterogeneous catalysts, to provide clear benchmarking criteria. We provide evidence that the molecular catalyst does not decompose to iridium oxide during the water oxidation reaction but it becomes activated by a reversible dimerization process.

We also study the electrocatalysis towards OER in alkaline media on earth-abundant materials. Chapter 4 presents a study of the OER electrocatalysis on nickel double hydroxides doped with 3d transition metals immobilized on gold in alkaline media. The results of this study demonstrate that the nature of the active site in the double hydroxides is strongly dependent on the dopant incorporated in the compound. The study provides guidelines that can be employed for the rational design of nickel-based water oxidation catalysts in alkaline media.

Chapter 5 continues the study of the OER electrocatalysis in alkaline media. This chapter presents a spectroelectrochemical study on the effect of pH on the catalytic activity of nickel oxyhydroxide. We provide evidence of a deprotonation process of the NiOOH towards a negatively charge surface intermediate (oxo / superoxo species) that strongly affects its catalytic activity towards OER. The evidence in this chapter shows once more that the development of good OER anodes should take into consideration the synergy of the OER catalyst with the electrolyte.

Finally, in chapter 6 we return to the acid-based OER electrocatalysis. We present a new type of OER catalyst based on iridium double perovskites to drive the reaction in acid media. These compounds contain three times less iridium than the IrO_2 benchmarking

catalyst and exhibit more than 3-fold higher catalytic activity, which makes them the most active catalysts for OER in acid media reported to date.

REFERENCES

(1) Lewis, N. S.; Nocera, D. G. *Proc. Natl. Acad. Sci. U. S. A.* **2006**, *103*, 15729.

(2) Trotochaud, L.; Boettcher, S. W. *Scripta Mater.* **2014**, *74*, 25.

(3) Cook, T. R.; Dogutan, D. K.; Reece, S. Y.; Surendranath, Y.; Teets, T. S.; Nocera, D. G. *Chem. Rev.* **2010**, *110*, 6474.

(4) Dau, H.; Limberg, C.; Reier, T.; Risch, M.; Roggan, S.; Strasser, P. *ChemCatChem* **2010**, *2*, 724.

(5) Bensaid, S.; Centi, G.; Garrone, E.; Perathoner, S.; Saracco, G. *ChemSusChem* **2012**, *5*, 500.

(6) Crabtree, G. W.; Dresselhaus, M. S.; Buchanan, M. V. *Phys. Today* **2004**, *57*, 39.

(7) Hoffert, M. I.; Caldeira, K.; Jain, A. K.; Haites, E. F.; Harvey, L. D. D.; Potter, S. D.; Schlesinger, M. E.; Schneider, S. H.; Watts, R. G.; Wigley, T. M. L.; Wuebbles, D. J. *Nature* **1998**, *395*, 881.

(8) Kärkäs, M. D.; Verho, O.; Johnston, E. V.; Åkermark, B. *Chem. Rev.* **2014**, 11863.

(9) Fabbri, E.; Habereder, A.; Waltar, K.; Kötz, R.; Schmidt, T. J. *Catalysis Science & Technology* **2014**, *4*, 3800.

(10) Crabtree, G. W.; Lewis, N. S. *Phys. Today* **2007**, *60*, 37.

(11) Joya, K. S.; Joya, Y. F.; Ocakoglu, K.; van de Krol, R. *Angew. Chem. Int. Ed.* **2013**, *52*, 10426.

(12) Rossmeisl, J.; Logadottir, A.; Norskov, J. K. *Chem. Phys.* **2005**, *319*, 178.

(13) Rossmeisl, J.; Qu, Z. W.; Zhu, H.; Kroes, G. J.; Norskov, J. K. *J. Electroanal. Chem.* **2007**, *607*, 83.

(14) Koper, M. T. M. *J Electroanal Chem* **2011**, *660*, 254.

(15) Man, I. C.; Su, H.-Y.; Calle-Vallejo, F.; Hansen, H. A.; Martinez, J. I.; Inoglu, N. G.; Kitchin, J.; Jaramillo, T. F.; Norskov, J. K.; Rossmeisl, J. *Chemcatchem* **2011**, *3*, 1159.

(16) Halck, N. B.; Petrykin, V.; Krtil, P.; Rossmeisl, J. *PCCP* **2014**, *16*, 13682.

(17) Matsumoto, Y.; Sato, E. *Materials Chemistry and Physics* **1986**, *14*, 397.

(18) Trasatti, S. *J. Electroanal. Chem.* **1980**, *111*, 125.

(19) McCrory, C. C.; Jung, S.; Peters, J. C.; Jaramillo, T. F. *J Am Chem Soc* **2013**, *135*, 16977.

(20) Lee, Y.; Suntivich, J.; May, K. J.; Perry, E. E.; Shao-Horn, Y. *J. Phys. Chem. Lett.* **2012**, *3*, 399.

(21) Hayfield, P. C. S. *Platinum Metals Rev.* **1998**, *42*, 116.

(22) Antolini, E. *ACS Catal.* **2014**, *4*, 1426.

(23) Gong, M.; Dai, H. *Nano Res.* **2014**, 1.

(24) Gong, M.; Li, Y.; Wang, H.; Liang, Y.; Wu, J. Z.; Zhou, J.; Wang, J.; Regier, T.; Wei, F.; Dai, H. *J Am Chem Soc* **2013**, *135*, 8452.

(25) Grimaud, A.; May, K. J.; Carlton, C. E.; Lee, Y. L.; Risch, M.; Hong, W. T.; Zhou, J.; Shao-Horn, Y. *Nat Commun* **2013**, *4*, 2439.

(26) Lu, Z.; Xu, W.; Zhu, W.; Yang, Q.; Lei, X.; Liu, J.; Li, Y.; Sun, X.; Duan, X. *Chem Commun (Camb)* **2014**, *50*, 6479.

(27) Suntivich, J.; May, K. J.; Gasteiger, H. A.; Goodenough, J. B.; Shao-Horn, Y. *Science* **2011**, *334*, 1383.

(28) Limburg, B.; Bouwman, E.; Bonnet, S. *Coordination Chemistry Reviews* **2012**, *256*, 1451.

(29) Hetterscheid, D. G. H.; Reek, J. N. H. *Angew. Chem. Int. Ed.* **2012**, *51*, 9740.

(30) Duan, L.; Bozoglian, F.; Mandal, S.; Stewart, B.; Privalov, T.; Llobet, A.; Sun, L. *Nat Chem* **2012**, *4*, 418.

(31) Huang, J.; Blakemore, J. D.; Fazi, D.; Kokhan, O.; Schley, N. D.; Crabtree, R. H.; Brudvig, G. W.; Tiede, D. M. *Physical Chemistry Chemical Physics* **2014**, *16*, 1814.

(32) Blakemore, J. D.; Mara, M. W.; Kushner-Lenhoff, M. N.; Schley, N. D.; Konezny, S. J.; Rivalta, I.; Negre, C. F. A.; Snoeberger, R. C.; Kokhan, O.; Huang, J.; Stickrath, A.; Tran, L. A.; Parr, M. L.; Chen, L. X.; Tiede, D. M.; Batista, V. S.; Crabtree, R. H.; Brudvig, G. W. *Inorg Chem* **2013**, *52*, 1860.

Chapter 2

Evidences for gold oxide decomposition mechanism during the electrochemical water oxidation

ABSTRACT

In this chapter we study through a multiplicity of experimental and theoretical techniques the electrochemical evolution of oxygen on gold, the metal on which water splitting was initially discovered more than two centuries ago. The evidence obtained with a combination of *in situ* surface-enhanced Raman spectroscopy, online electrochemical mass spectrometry and density functional theory calculations suggests the existence of several mechanisms for the evolution of O_2 on Au electrodes, depending on the electrode potential. Significantly, at approximately 2.0 V vs. RHE the first O_2 that is evolved consists of two oxygens from the surface oxide, suggesting an oxide decomposition or oxide disproportionation step. At somewhat higher potentials, O_2 is formed by a combination of oxygen from the oxide lattice and oxygen provided by water. The oxide decomposition step implies a more three-dimensional mechanism for oxygen evolution than previously suggested mechanisms, which involve only surface-adsorbed intermediates.

This chapter has been published in: Diaz-Morales, O.; Calle-Vallejo, F.; de Munck, C. and Koper M.T.M. *Chemical Science* **2013**, 4, 2334-2343.

2.1. Introduction

The first recorded experiment on water electrolysis was carried out by Adriaan Paets van Troostwijk and Jan Rudolph Deiman in Haarlem, The Netherlands, in 1789.[1,2] Paets van Troostwijk and Deiman used an electrostatic machine invented by Martinus van Marum to discharge an electric potential difference between two gold electrodes in a Leyden jar filled with water. Hydrogen evolved on one gold electrode, and oxygen evolved on the other gold electrode.

Almost two hundred and twenty five years later, water splitting is considered as an important part of what many consider to be the only sustainable solution to the world's energy problem.[3,4] Using sunlight to generate photo-excited electrons and holes would allow the photo-electrocatalytic synthesis of hydrogen and oxygen. Hydrogen would be the fuel to store the sun's energy, and may be converted back into electricity in a fuel cell, using the reverse reaction to water electrolysis. It is generally recognized that one of the key fundamental bottlenecks in making the (photo-)electrochemical generation of fuels a viable technology lies in the poor kinetics of the anode reaction, *i.e.* the water oxidation to oxygen.

The best and most stable inorganic catalysts for water splitting are oxides.[5,6] In spite of decades of research into the oxygen-evolving activities of a large variety of oxides, the suggested mechanisms for oxide-catalyzed water splitting are surprisingly simple and "two-dimensional", focused on reaction intermediates that exist directly at the oxide-electrolyte interface.[5,7,8] However, explicit spectroscopic evidence for such pathways is still largely missing. One possible exception is a recent study by Yeo et al.[9] who observed a vibrational signal near 820 cm^{-1} using Surface-Enhanced Raman Spectroscopy (SERS) during the oxygen evolution on gold both in acid and alkaline media. They attributed this signal to the formation of a surface-bound hydroperoxy intermediate.

In this chapter, we return to the electrode material originally used by Paets van Troostwijk and Deiman, and discuss the possibility of a new mechanism for the oxygen

evolution on gold electrodes covered by a thin oxide, based on a combination of electrochemistry, *in situ* Surface-Enhanced Raman Spectroscopy, online electrochemical mass spectrometry (OLEMS), and first-principles density functional theory (DFT) calculations. Our model is significantly different from the models advocated in the literature and supported in the recent SERS work of Yeo et al. The key ingredient of our model is that we assume that the thin but distinctly three-dimensional nature of the gold oxide is intimately involved in the mechanism, and that oxygen is evolved not through the coupling of surface intermediates, but as the result of the decomposition of the unstable three-dimensional surface oxide releasing molecular oxygen into the solution. Such a new mechanism, if correct, could suggest novel strategies towards developing better inorganic water splitting catalysts.

2.2. Experimental and Computational Section

2.2.1. Experimental

All glassware was thoroughly cleaned before starting experiments by boiling in 1:10 mixture of 30% H_2O_2 / concentrated H_2SO_4 to remove organic contaminations, and was subsequently boiled five times in Millipore Milli-Q water (resistivity >18.2 MΩ cm). Electrolyte solutions were prepared with Suprapur (Merck) reagents and Milli-Q water. Dissolved oxygen in solutions was removed prior to measurements by purging with argon (purity grade 5.0) for at least 30 min, and the argon was kept flowing above solution during experiments. Experiments with ^{18}O enriched water were performed with 98% ^{18}O water (GMP standard, purchased from CMR).

In situ Surface Enhanced Raman Spectroscopy (SERS) was performed with a confocal Raman microscope (LabRam HR, Horiba Yobin Yvon) with a 50X objective. A He/Ne laser (633 nm) was used as excitation source. Backscattered light was filtered by a 633 nm edge filter, directed to the spectrograph and to the detector. Details of the setup can be found in reference 10. The electrochemical SERS experiments were made with an Ivium potentiostat/galvanostat (IviumStat), using a home-made electrochemical cell with a small

electrolyte volume necessary for the $H_2{}^{18}O$ experiments. The electrochemical cell has one compartment and three electrodes, a gold wire as counter electrode, reversible hydrogen electrode (RHE) as reference electrode (all potentials in this work are reported versus this reference electrode unless otherwise stated) and a roughened gold surface as working electrode. The working electrode was mechanically polished to mirror finish using alumina with different grain sizes to 0.3 μm, rinsed with Milli-Q water and ultrasonicated during 15 min to remove all residuals of mechanical polishing. Next, the gold electrode was electrochemically roughened by 25 oxidation-reduction cycles (ORC) in 0.1 M KCl. The ORC were performed between -0.30 and 1.20 V vs. SCE, during which the potential was held for 30 seconds at the negative limit and for 1.3 seconds at the positive limit, a method reported to give a brownish surface that is SERS active.[11]

Online Electrochemical Mass Spectrometry (OLEMS) experiments were performed using an EvoLution mass spectrometer system (European Spectrometry systems Ltd). The setup has a mass detector (Prisma QMS200, Pfeiffer) which was brought to vacuum using both a turbo molecular pump (TMH-071P, Pfeiffer, flow rate 60 L s^{-1}) and a rotary vane pump (Duo 2.5, Pfeiffer; flow rate 2.5 m^3 h^{-1}). During measurements, the pressure inside the mass detector chamber was around 10^{-6} mbar. Volatile reaction products were collected from electrode interface by a small inlet tip positioned close (~10 μm) to electrode surface using a micrometric screw system and a camera.[12] The inlet tip is made with a porous Teflon cylinder (Porex®) mounted in a Kel-F holder. The inlet is connected to the mass detector through a PEEK capillary. Before use, the inlet tip was cleaned during 15 min with a solution 0.2 M $K_2Cr_2O_7$ in 2 M H_2SO_4 and rinsed thoroughly with Milli-Q water.

2.2.2. Computational

All adsorption energies were calculated by means of DFT simulations using the Vienna Ab-initio Simulation Package (VASP)[13]. The exchange and correlation parts of the total energies were estimated with the Perdew-Burke-Ernzerhof (PBE) functional.[14] The Au surfaces were represented by supercells in which the lattice constant was 4.18 Å, corresponding to an interatomic distance of 2.95 Å. Four atomic layers were used to

represent the surfaces, of which the topmost two and the adsorbates were fully allowed to relax whereas the bottom layers were fixed at the bulk equilibrium distances. The vertical separation between successive slabs was always more than 15 Å and dipole corrections were applied. In the search for optimal geometries the kinetic energy cut-off of the plane-wave basis set was 450 eV. The Brillouin zones of the 2×2 and √3×√3 (111) supercells were sampled with 6×6×1 Monkhorst-Pack grids,[15] which guaranteed convergence of binding energies within a range of 0.05 eV. The Fermi level was smeared with the Methfessel-Paxton approach[16] with an electronic temperature of 0.2 eV, and all energies were extrapolated to T = 0 K. The relaxations of the atoms were carried out with the quasi-Newton minimization scheme, until the maximum force on any atom was below 0.05 eV $Å^{-1}$. Ionic cores were described by Projector Augmented Wave (PAW) potentials.[17] All energies reported here are free energies calculated from DFT, vibrational analyses to estimate zero-point energies and vibrational frequencies, and thermodynamic tables to estimate entropy corrections to gas-phase species, through the expression: $\Delta G = \Delta E_{DFT} + \Delta ZPE - T\Delta S$, as described elsewhere.[18,19] Besides, we took into account the contribution of vibrational entropies to the free energies of oxygenated adsorbates and lattice species. The DFT energies of adsorption of *O, *OH, and *OOH (ΔG_O, ΔG_{OH}, and ΔG_{OOH}), were calculated with respect to hydrogen and water, as shown in Reactions (1) to (3) and expressed mathematically in equation (4) to (6):

$$* + H_2O \rightarrow *O + H_2 \quad (1)$$

$$* + H_2O \rightarrow *OH + 1/2\,H_2 \quad (2)$$

$$* + 2H_2O \rightarrow *OOH + 3/2\,H_2 \quad (3)$$

$$\Delta G_O = G_{*O} + G_{H_2} - G_* - G_{H_2O} \quad (4)$$

$$\Delta G_{OH} = G_{*OH} + 1/2\,G_{H_2} - G_* - G_{H_2O} \quad (5)$$

$$\Delta G_{OOH} = G_{*OOH} + 3/2\,G_{H_2} - G_* - 2G_{H_2O} \quad (6)$$

where * stands for an adsorption site on the electrode. Note that these definitions capitalize on the equilibrium between protons, electrons and hydrogen gas in aqueous media ($1/2\,H_2 \rightarrow H^+ + e^-$) to avoid two well-known problems: first the calculation of solvated protons, the appropriate energies of which cannot be obtained within the standard DFT formalism; and second the use of the value of the absolute standard hydrogen electrode potential, a number with large uncertainty in the literature, with reported values ranging from 4.28 to 4.85 V (See references 18,20,21 and references therein).

The energies of different surface states are computed with increasing potential on the Reversible Hydrogen Electrode (RHE) scale by thin-layer oxides. In these calculations, oxygenated species (*O, *OH, *OOH) occupy substitutional positions in the top layer of Au (111) lattices and distort the normal configuration of the atoms due to the differences in Au-Au and Au-O distances.

2.3. Results

2.3.1. Experimental results

Figure 1a shows the linear-sweep voltammetry (0.001 V s^{-1}) of water oxidation on a polycrystalline gold electrode in 1.0 M $HClO_4$, together with an enlargement of the onset of the anodic current, and Figure 1b shows the cyclic voltammogram of the gold electrode recorded between 0 and 1.8 V vs. RHE. These results show that the formation of gold surface (hydr)oxides starts at *ca.* 1.3 V and that the onset of continuous anodic current is at *ca.* 1.9 V vs. RHE. *In situ* SERS experiments during electrochemical water oxidation in aqueous solution on gold surfaces in 1.0 M $HClO_4$ were performed in order to confirm the signal around 820 cm^{-1} observed by Yeo et al.[9] The potential-dependent vibrational spectra acquired in normal water under steady state conditions are shown in Figure 1c. The spectra exhibit the characteristic features previously reported.[22] The sharp signal at *ca.* 935 cm^{-1} corresponds to the stretching vibration of Cl-O due to perchlorate anions. The perchlorate signal does not depend on the electrode potential, and only starts decreasing at very positive potentials at which the oxide layer is thick enough to affect the surface enhancement. Both

observations suggest that the observed perchlorate is in the double layer near the gold surface, but that it is not adsorbed. The broad signal centered around 580 cm^{-1} is related to the Au-O vibration of the gold surface oxide, in agreement with earlier observations by Desilvestro and Weaver[22] and Yeo et al.[9] Remarkably, we also observe a shoulder on this broad band at *ca.* 650 cm^{-1}, that has not been observed in previous works.

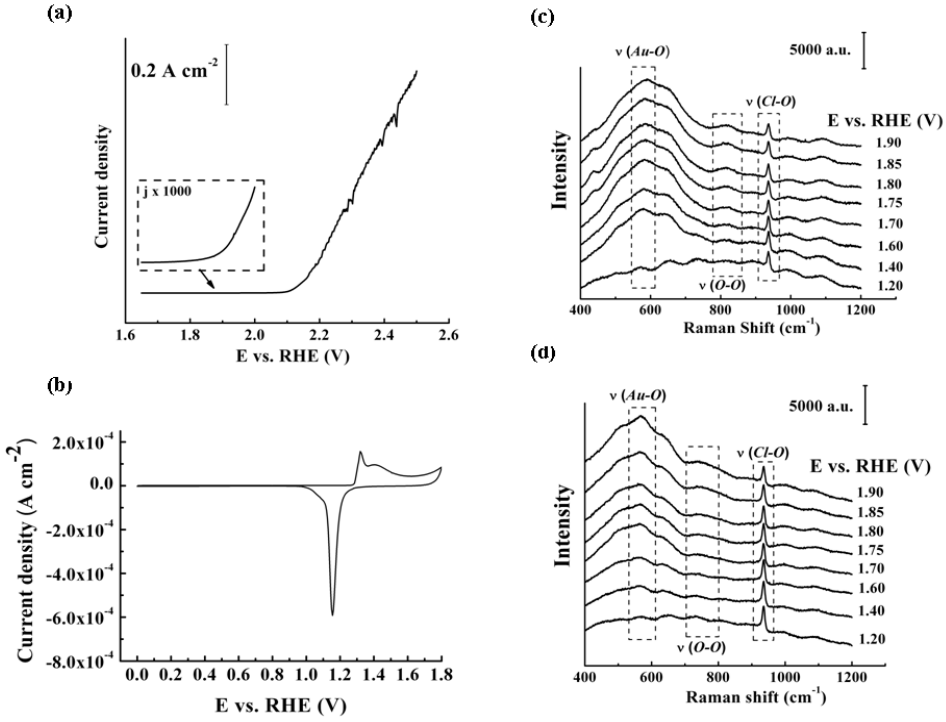

Figure 1. a) Linear sweep voltammetry for oxygen evolution reaction on gold electrode at 0.001 V s^{-1}. The current below 2.0 V, multiplied by a factor of 1000, is shown as inset in the voltammogram. b) Cyclic voltammetry for gold electrode showing the "surface oxide" formation, acquired at 0.05 V s^{-1}. c) SERS spectra for oxygen evolution acquired at constant potential in ^{16}O water, d) Same as b) but experiments performed in ^{18}O water. The experiments were performed in aqueous solution of pH = 1.

According to Desilvestro and Weaver, [22] $Au(OH)_3$ and Au_2O_3 exhibit Raman bands at 650 and 635 cm^{-1}, respectively. As Desilvestro and Weaver have noted, the broadness of the gold-oxide band suggests "a wide multiplicity of surface oxide structures formed simultaneously, possibly involving different coordination geometries and hydration states of the gold atoms." In alkaline media, Desilvestro and Weaver observed the stretching frequency of Au-OH at around 425 cm^{-1}, shifting to higher frequencies with more positive potential, indicating the formation of gold surface oxides.

In agreement with Yeo et al.,[9] we also observe a signal around 810 cm^{-1} that starts appearing at potentials positive of 1.4 V, and that was attributed to an OOH species adsorbed on the gold (oxide). From a comparison to the voltammetric data in Figure 1a, we conclude that this vibrational signal is observed at least 0.4 V less positive than the onset of water oxidation. Yeo et al. state that "it is not surprising that OOH species are observed before visible commencement of O_2 gas evolution because the elementary steps of the OER process occur sequentially over a range of potentials starting from 1.1 V (vs. Ag/AgCl)". However, we do consider this surprising. DFT calculations of OOH adsorption on gold, gold oxides, and many other materials suggest that this species is highly unstable,[7,8,19] and therefore should decompose into O_2 rapidly. In the sequence of the elementary steps of the currently accepted OER mechanism, the OOH intermediate is the highest energy intermediate. Its spectroscopic observation over the potential range which essentially corresponds to the formation of the gold surface oxide (compare to the cyclic voltammetry in Figure 1b) is at least unexpected if not unlikely. In order to further elucidate the chemical identity of the species corresponding to this Raman band, spectroelectrochemical experiments were performed in $HClO_4$ solutions made with ^{18}O enriched (98%) water. Figure 1d shows the SERS spectra for water oxidation in ^{18}O water. As expected, the signal corresponding to the perchlorate stretching does not shift when ^{16}O water is replaced by ^{18}O water. On the other hand, the signals corresponding to Au-O vibrations have shifted to lower frequencies due to the isotope effect. Table 1 compares the peak positions in ^{16}O water, in ^{18}O water and in deuterated ^{16}O water, for three potentials. The band ascribed to the Au-O vibration near 580 cm^{-1} exhibits a lowering close to the expected 5.7 % isotope

shift, but the signal around 810 cm^{-1} exhibits a larger frequency shift than expected (*ca*. 10% vs. the expected 5.7%). However, we note that the position of the maximum of this broad peak is difficult to determine (as illustrated in Figure A1 in Appendix A), and moreover for the spectra in ^{18}O water, the broad peak lies on the shoulder of the 560 cm^{-1} feature, an effect that may artificially lower the actual frequency. Experiments were also performed in deuterium oxide (D_2O). For the Au-O band a lowering in frequency is observed, but there was no significant shift in the O-OH signal compared to normal water (see Table 1, the corresponding spectra are shown in Figure A2 in Appendix A). Note that Yeo et al.[9] reported a shifting of that peak to higher frequencies when experiments were performed in deuterium oxide and suggested that to be due to isotopic effects. Although such a positive shift is opposite to the expected shift using the harmonic oscillator model, they attributed the small increase in frequency to the coupling between O-O and O-D modes. However, our results do not confirm this small shift.

Table 1. Vibrational frequencies for the Au-O and O-OH peaks as function of potential in pH 1 solution prepared respectively in ^{16}O, ^{18}O water and D_2O.

E vs. RHE (V)	ν / cm^{-1}					
	Au-O			O-OH		
	^{16}O water	^{18}O water	D_2O	^{16}O water	^{18}O water	D_2O
1.7	584	562	578	811	734	808
1.8	586	564	579	812	738	812
1.9	589	567	581	810	734	810

In order to probe the involvement of the gold surface oxide in the generation of molecular oxygen during OER, online electrochemical mass spectrometry (OLEMS) experiments were performed. Figure 2 shows the results for oxygen evolution from normal water, confirming that the anodic current is mirrored by the detection of oxygen in the mass

spectrometer. From the enlargement of the $^{32}O_2$ signal, we conclude that oxygen evolution starts at *ca.* 2.0 V, and it is difficult to claim that oxygen is evolved below that potential. In a separate experiment, the gold electrode was oxidized in a two-electrode cell filled with ^{18}O water at 2.0 V so as to generate an ^{18}O enriched gold oxide on the gold.

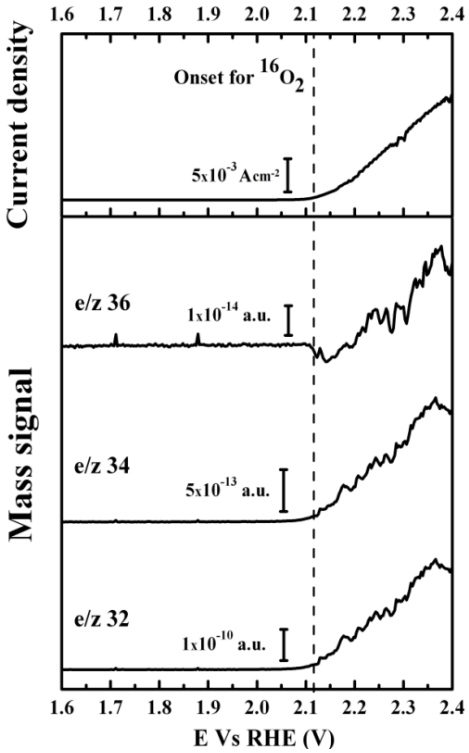

Figure 2. Linear sweep voltammetry for oxygen evolution reaction on a gold electrode in a 1 M $HClO_4$ solution prepared with ^{16}O water. b) OLEMS signals during oxygen evolution corresponding to different isotopes of dioxygen ($^{16}O_2$, $^{16}O^{18}O$ and $^{18}O_2$) as a function of applied potential. Scans were made at 0.001 V s^{-1}.

Next, the thus generated gold oxide electrode was transferred to an ^{16}O aqueous electrolyte. Figure 3a shows the resulting current-potential profile during the positive linear scan, alongside the signals recorded in the mass spectrometer corresponding to various

isotopes of dioxygen (namely $^{16}O_2$, $^{16}O^{18}O$ and $^{18}O_2$ species) produced during oxygen evolution (figure 3b). In agreement with Figure 2b, no dioxygen is detected in the mass spectrometer at potentials lower than 2.0 V but as can be seen in figure 3b, $^{18}O_2$ is the first oxygen product evolved from the gold oxide layer with no apparent increase in signal corresponding to $^{16}O_2$. This would indicate that a kind of oxide decomposition mechanism is operative, at least in the very early stages of the oxygen evolution reaction. Previous similar online mass spectrometry experiments conducted with RuO_2 and IrO_2 electrodes in (partially) isotopically labeled water has indicated an oxygen exchange (or Mars-Van Krevelen-type) mechanism, but has not provided evidence for the oxide decomposition mechanism (or disproportionation mechanism, see Discussion) suggested by Figure 3. [23-25]

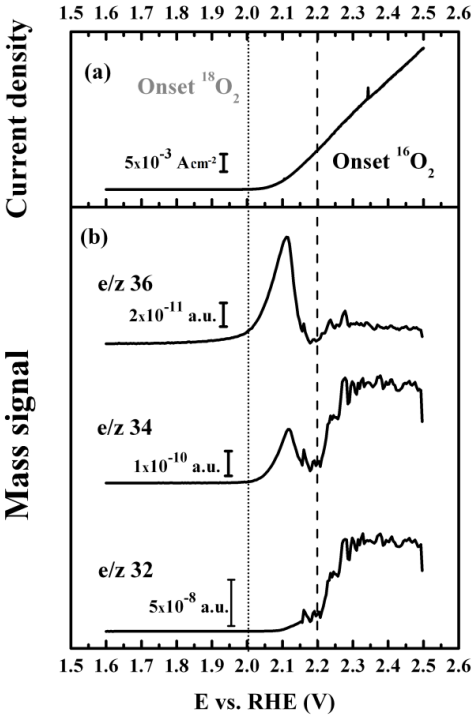

Figure 3. Linear sweep voltammetry for oxygen evolution reaction on ^{18}O gold oxide performed in a 1 M $HClO_4$ solution prepared with ^{16}O water. b) OLEMS signals during oxygen evolution on the gold electrode corresponding to different isotopes of dioxygen ($^{16}O_2$, $^{16}O^{18}O$ and $^{18}O_2$) as function of potential. Scans were made at 0.001 V s^{-1}.

Since it is to be expected that the nature of the oxide layer formed on gold depends on the gold surface structure, we have determined the oxygen-evolving activities of three low-index gold single-crystal surfaces. Figure 4 shows the cyclic voltammetry of the three electrodes for 0 < E < 1.75 V, in good agreement with the ones reported in the literature,[26,27] and the Tafel plots of the same electrodes for 1.85 < E < 2.16 V. The Tafel plots clearly show two different slopes, 112-163 mV/dec for E < 2.0 V, for which we do not observe oxygen in the mass spectrometer, and 42-46 mV/dec for E > 2.0 V, corresponding to the potential region of oxygen evolution. The latter Tafel slope agrees well with the values reported many decades ago.[28] Interestingly, there is a clear structure sensitivity, the Au(110) surface being the most active surface, and the Au(100) surface being the least active, although we realize that under surface oxide forming and oxygen-evolving conditions, these surfaces no longer exhibit their nominal structure.

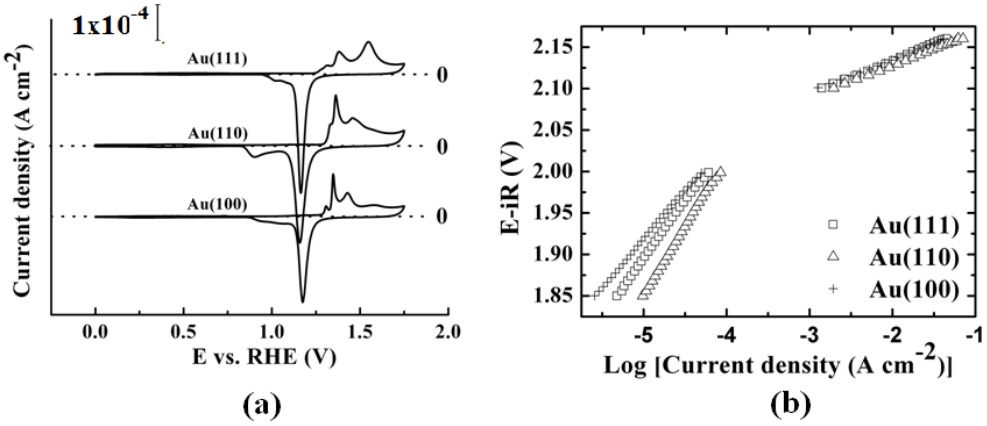

Figure 4. a) Cyclic voltammetry for the three low-index gold single crystals in 1 M $HClO_4$ solution prepared with ^{16}O water, Scan rate: 0.05 V s^{-1}. b) Tafel plot obtained from a liner sweep voltammetry to oxygen evolution potentials with the three low-index gold single crystals. Scan rate: 0.001 V s^{-1}.

Finally, in Figure 5 we plot the charge measured in the reduction of gold oxide between 0.8 and 1.3 V as a function of the positive limit potential in a previous linear-sweep voltammogram. The charge is expressed in monolayer equivalents, where one monolayer is 390 $\mu C \cdot cm^{-2}$. [29] This plot is very similar to others available in the literature[30], and is included here to illustrate that there appears to be a leveling off in oxide-layer growth between 1.5 and 2 V, and that oxygen evolution starts, at *ca.* 2.0 V, after the completion of an oxide layer of 3 ML equivalents.

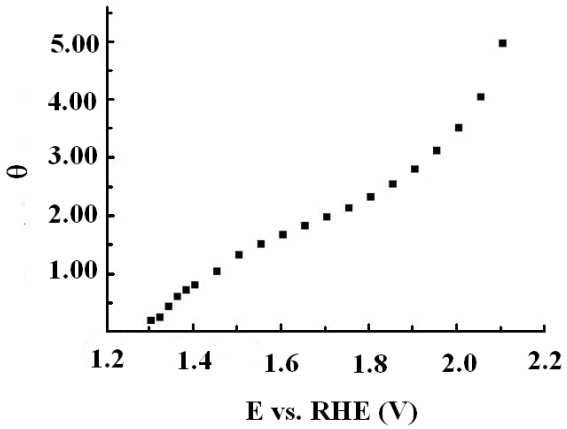

Figure 5. Oxygen coverage on a gold electrode as a function of positive potential limit during anodic polarization.

2.3.2. Brief summary of literature on the surface oxidation of gold

Before we discuss the computational results, it is useful to briefly summarize some of the most relevant experimental results from the extensive literature of electrochemical gold surface oxide formation. First of all, gold is the only metal that is thermodynamically stable at potentials above the potential of the water oxidation. Pourbaix diagrams of gold typically consider only two stable forms of gold oxide or hydroxide, *i.e.* gold(III) oxide and hydroxide[31,32]:

$$2Au + 3H_2O \rightleftharpoons Au_2O_3 + 6\left(H^+ + e^-\right) \qquad E^0 = 1.51V \tag{7}$$

$$Au + 3H_2O \rightleftharpoons Au\left(OH\right)_3 + 3\left(H^+ + e^-\right) \qquad E^0 = 1.46V \tag{8}$$

Note that these two reactions imply:

$$Au_2O_3 + 3H_2O \rightleftharpoons 2Au\left(OH\right)_3 \qquad \Delta G \approx -0.31\text{eV} \tag{9}$$

In fact, hydrous Au_2O_3 is often considered equivalent to gold(III) hydroxide. $Au(OH)_3$ is a planar compound, not soluble in water. Gold oxides with oxidation states other than Au(III) are unstable and extremely rare[33]. Previous claims of Au_2O and AuO in fact turned out to be mixtures of Au and Au_2O_3.[34]

Several authors have attempted to characterize the oxidation state of gold oxides grown electrochemically. Using *ex situ* X-ray Photoelectron Spectroscopy (XPS), Peuckert et al.[34] studied thin oxide layers on Au(100), and Juodkazis et al.[35] studied thin oxide layers on polycrystalline gold, both in sulfuric acid electrolyte. Au(III) was the only Au oxidation state observed. According to Peuckert et al.,[34] initially a $Au(OH)_3$ layer is formed, and from 2.0 V the layer is further deprotonated or dehydrated to gold oxyhydroxide AuOOH ("meta gold acid"), which is supposed to initiate more rapid film growth. Near 2.0 V, the $Au(OH)_3$ is suggested to consist of "beyond two" [34] or "three" [35] monolayers. Thermal decomposition of electrochemically prepared AuOOH does not lead to anhydrous Au_2O_3 but to decomposition into a mixture of Au and Au_2O_3 with the concomitant formation of molecular oxygen O_2.[34] Interestingly, Peuckert et al. find evidence for molecular oxygen "trapped" or "dissolved" in thick oxide layers, the nature of which has remained unclear. A similar kind of molecular oxygen or peroxide occluded in intergrain voids of Au_2O_3 grown in the gas phase was observed by exposing polycrystalline gold to activated oxygen.[36] Moreover, *in situ* EXAFS studies by Weiher[37] detected only Au(III) in electrochemically grown gold oxide layers, and concluded that electrochemical Au_2O_3 is highly disordered.

Detailed electrochemical studies of oxide layers grown on (single-crystalline) gold electrodes have shown that the initial adsorption of OH to the gold surface at *ca.* 1.3 V is reversible, but is rapidly followed by further oxidation including place exchange between gold and oxygen atoms, leading to a quasi three-dimensional hydroxy-oxide film.[27,38,39] According to Conway, at 1.6 V AuOH is further oxidized to a AuO surface film. From quartz crystal microbalance and ellipsometry measurements, Xia and Birss[40] have concluded that the thin ("compact") oxide layer consists of AuO below 1.5 V, and of a mixture of AuO and Au_2O_3 above 1.5 V. Up to three monolayers of this thin Au_2O_3 (α-oxide) layer can be formed before a thicker oxide (β-oxide) film forms.

2.3.3. Computational results

The foregoing brief summary of the interpretation of the experimental results suggests that although surface oxide formation on gold electrodes has been extensively studied, there is currently no universally accepted interpretation for all the observed features, especially those observed at higher potentials. Therefore, we have undertaken a DFT-based computational study of the surface thermodynamics of electrochemical gold, which suggests that the Au(111) surface experiences, at least, the five changes listed below as the potential is successively increased, and as illustrated in Figure 6 (analogous analyses can in principle be made for other surface facets). It is important to remark at this point that PBE, the xc-functional used in our calculations, typically overbinds adsorbates with respect to the experimentally observed values[41] and hence we expect to find deviations on the order of ~0.2 V in the computed values when compared to the experiments presented here and in references. [27,34,38]

1. *OH adsorption: At 1.05 V vs. RHE the adsorption of *OH becomes thermodynamically favorable on the Au(111) surface. The reaction that describes the process is given in equation (2). The quoted potential corresponds to a *OH coverage of 1/3 ML, modeled in a $\sqrt{3}\times\sqrt{3}$ (111) supercell. In this case we added a correction of -0.55 eV to the free energy accounting for the solvation of the *OH groups, similar to that recommended by Tripkovic et al for Pt(111) under ORR conditions.[42]

2. Gold(III) hydroxide formation: At 1.17 V vs. RHE the oxidation of the surface is such that a thin layer of $Au(OH)_3$ is formed at the surface of the electrode. The reaction that describes the process is given in equation (10).

$$Au_4{}^*(OH)_2 + H_2O \rightarrow Au(OH)_3 + 3Au + (H^+ + e^-) \quad (10)$$

where $Au_4{}^*(OH)_2$ denotes a 2×2 (111) supercell of Au with 2 *OH groups adsorbed on it (*i.e.* the coverage is ½ ML). Moreover, the Au atoms that are freed during this reaction and the following reactions are supposed to be incorporated into the bulk or to accumulate in Au islands at the surface, which will in turn be oxidized. Therefore, we consider it likely that this reaction would be responsible for the onset of Au(111) surface roughening, as it involves the formation of a monolayer of surface hydroxide.

3. AuOOH formation: at 1.28 V vs. RHE the hydroxide ($Au(OH)_3$) turns into an oxyhydroxide. The reaction that describes this process is given in equation (11).

$$Au(OH)_3 + Au + H_2O \rightarrow 2Au(OOH) + 3(H^+ + e^-) \quad (11)$$

It is to be noted here that in both oxyhydroxide and hydroxide the formal gold oxidation state is Au^{3+} and, therefore, they differ mainly in their degree of hydration. We also calculated AuOOH in the hydroperoxide structure; however this compound is less stable than its oxyhydroxide isomer by *ca.* 0.75 eV/OOH.

4. Oxide Formation: at 1.54 V vs. RHE the oxyhydroxide is further dehydrated to Au_2O_3 (modeled in a 5×2 (111) supercell). We chose Au_2O_3 in our model, as several studies referred to above have concluded that the Au(III) oxidation state is dominant, but several other oxides can in principle be formed, including AuO_2, as reported by Pourbaix,[32] as well as other non-stoichiometric oxides. The reaction that describes the oxidation process is given in equation (12).

$$5AuOOH \rightarrow 2Au_2O_3 + Au + 2O_2 + 5(H^+ + e^-) \quad (12)$$

5. Catalytic Oxygen Evolution: at 1.95 V vs. RHE the oxide surface starts the actual catalysis of the oxygen evolution reaction (OER). The overall process is given by the reaction: $2H_2O \rightarrow O_2 + 4\left(H^+ + e^-\right)$. The onset potential is estimated from the potential-determining step (PDS), *i.e.* the step in the mechanism that corresponds to the thermodynamically least favorable step in the mechanism and that thereby determines the minimum value of the onset potential of the reaction. According to the model by Man et al[19], which is based on values of the adsorption energies of *O, *OH, and *OOH, the PDS in our case is the following:

$$*OH \rightarrow *O + \left(H^+ + e^-\right) \qquad (13)$$

On the other hand, the predicted OER onset potentials for $Au(OH)_3$ and AuOOH are 2.22 V and 2.39 V, respectively. Regardless of the active phase generating oxygen, oxidized surfaces containing Au^{3+} are expected to have large overpotentials for OER and to be located on the leg of the volcano curve corresponding to weak oxygen adsorption, as proposed by Man et al.[19]

We note at this point that the conclusions of the experimental works by Conway et al.[38] with Au(111) electrodes in 0.01M $HClO_4$ are rather similar to our proposal in Figure 6. They suggest that a water adlayer will turn into an *OH adlayer on Au(111) electrodes at potentials around 1.2 V vs. RHE. Moreover, the process will turn into a surface oxidation leading to $Au(OH)_3$ at potentials between 1.2 and 1.35 V vs. RHE. Besides, at potentials over 1.55 V vs. RHE they proposed that the surface will be composed of AuOOH as an oxyhydroxide capable of evolving oxygen catalytically. We conclude at this point that the (111) surface undergoes several stoichiometric and structural changes as the potential is anodically raised before it starts evolving oxygen catalytically, and that the hydration of the surface compounds decreases as the potential is increased. Also note from Figure 6 that the configuration of the Au atoms in the Au(111) surface changes as the gold(III) hydroxide phase is formed, suggesting that, as mentioned, at this point an electrochemical surface roughening could be introduced.

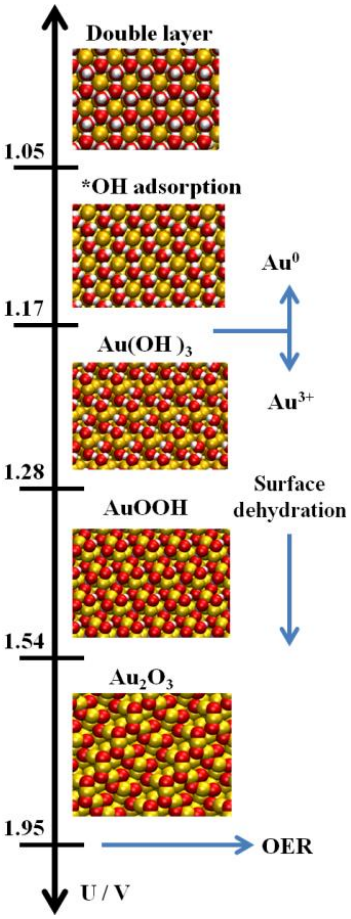

Figure 6. Schematics of the different stable surface states with increasing potential on a Au(111) electrode, as estimated from the DFT calculations. The double layer region is followed by *OH adsorption at 1.05 V vs. RHE, gold(III) hydroxide formation at 1.17 V, initial dehydration to form an oxyhydroxide 1.28 V, further dehydration to form a surface oxide at 1.54 V, and catalytic oxygen evolution at 1.95 V.

A second objective of our DFT calculations is to perform a vibrational analysis of possible intermediates, primarily aimed at the SERS signal at 810 ± 50 cm^{-1}. From a theoretical point of view, one can support the experimental claim that the signal corresponds to a stretching of O-O bonds at the surface on the basis of the vibrational frequencies of *O, *O_2, *OH, and *OOH on Au(111) and (211), and the values are shown

in Table 2. Note that the (211) facets are stepped surfaces with short (111) terraces and (100) steps.

Table 2. Selected vibrational frequencies of various species on their most stable adsorption sites on Au(111) and (211). In general, the vibrational frequencies decrease when the coordination number of the metal site is reduced. In all cases, only the closest frequencies to 810 ± 50 cm^{-1} are provided.

Species	ν / cm^{-1}	
	111	211
*O	361	449
$*O_2$	1278	1064
*OH	808	729
*OOH	860	823

From Table 2 we observe that, except for the vibrational frequencies of *O, those of the other adsorbates decrease upon reduction of the coordination number of the metal site to which the adsorbate is bound: the coordination number of the metal atoms at (111) surfaces is 9, whereas it is 7 at the step edge of (211) surfaces. Since the (111) is the most closed-packed surface of all fcc metal surfaces, its vibrational frequencies can be regarded as an upper bound for the Raman peaks, whereas those at the steps may be taken as a lower bound. Based on this approximation, only *OOH adsorbates fall in the appropriate range of frequencies found in the experiments (810 ± 50 cm^{-1}). Moreover, a glimpse at O-O stretching frequencies of some related gas-phase compounds such as O_2 (DFT: 1549 cm^{-1}, reported: 1580 cm^{-1} [43]), H_2O_2 (DFT: 914 cm^{-1}, reported: 864 cm^{-1} [43]), Au_2O_2 (DFT: 991 cm^{-1}), and AuOOH (DFT: 872 cm^{-1}), reveals that the O-O bond in question is single and that the oxygen atoms should be coordinated to Au and H atoms.

In order to discard that *OH groups could be responsible for the observed Raman signal, we also calculated the vibrational frequencies of *OH and *OOH on several Au facets, and the results are shown in Table 3. The arithmetic averages of the frequencies (754 ± 43 cm^{-1} and 824 ± 26 cm^{-1}) serve as a rough estimate of the expected centers of the peaks and confirm that only O-O stretching is expected at the experimental range of frequencies (810 ± 50 cm^{-1}).

Table 3. Vibrational frequencies of *OH and *OOH adsorbates on various Au surfaces. The coordination numbers (CN) are provided in each case to facilitate the observation of the trends. In both cases, a decrease in CN is well correlated with a decrease in the vibrational frequencies.

facet / adsorbates	ν / cm^{-1}	
	*OOH	*OH
111 (CN = 9)	860	808
100 (CN = 8)	801	767
211 (CN = 7)	823	729
110 (CN = 6)	810	712
Average	824	754
Standard deviation	26	43

Moreover, we calculated the vibrational frequencies of $Au(OH)_3$ (928 cm^{-1}), AuOOH (945 cm^{-1}) and Au_2O_3 (600 cm^{-1}) to verify that *OH and *O groups belonging to thin-layer structures in oxidized Au(111) do not exhibit any vibrations in the region around 810 ± 50 cm^{-1}. It is also noteworthy that the expected frequency of 810 ± 50 cm^{-1} does not appear when *OOH is adsorbed on oxidized Au atoms as shown in Table 4, where one can see that the O-O stretching frequencies of *OOH adsorbed on $Au(OH)_3$, AuOOH and Au_2O_3 are over 930 cm^{-1}. On the other hand, those of rough Au(111) (simulated as a 2x2

(111) unit cell with a missing row of Au atoms in the top layer) and pristine Au(111) are near 850 cm^{-1}.

Table 4. O-O stretching frequencies of *OOH adsorbates on various surface compounds of Au. When Au atoms are oxidized, the frequency of the O-O stretching increases, and as seen before in Table 3, *OOH adsorbed on under-coordinated Au atoms have lower O-O frequencies.

surface species	ν_{O-O} / cm^{-1}
Au(111)	860
Au(111) (rough)	840
$Au(OH)_3$	976
AuOOH	996
Au_2O_3	939

The observations in Tables 2 to 4 suggest that the frequency around 810 ± 50 cm^{-1} belongs to an O-O stretching from oxygen atoms bound on one side to a gold atom and on the other to a hydrogen, and that those Au atoms are not oxidized and have low coordination numbers. This in turn suggests that the formation of $Au(OH)_3$ and the other subsequent oxidation products should be accompanied by a noticeable roughening of the surface and by disproportion reactions that create Au islands. These observations are in agreement with the STM results of Schneeweiss and Kolb[39] and with the general mechanism of gold oxide formation proposed by Angerstein-Kozlowska and Conway.[27,38]

2.4. Discussion

The results presented in the previous sections are strongly suggestive of a mechanism for oxygen evolution that is considerably different from previous mechanisms suggested in the literature.[6-8] The combined electrochemistry and online mass spectrometry experiments

suggest that the first oxygen evolves at the transition from the α- to the β-oxide, after three monolayers of $Au(OH)_3$ or hydrous Au_2O_3 oxide have been formed. Our OLEMS results show that the first oxygen that evolves consists completely of oxygen atoms from the oxide. This would be consistent with Peuckert's[33] suggestion that the AuOOH that starts to be formed at 2.0 V is not stable but decomposes according to the overall reaction:

$$6\,\mathrm{AuOOH}\,(\alpha-\mathrm{oxide}) \rightarrow \mathrm{Au_2O_3}(\beta-\mathrm{oxide}) + 4\mathrm{Au} + 3\,\mathrm{O_2} + 3\,\mathrm{H_2O} \qquad (14)$$

This Au_2O_3 is not exactly the same as that formed below 2.0 V as it is used to build up the thicker β-oxide[39]. As mentioned in section 2.3.2, below 2.0 V a hydrous form of Au_2O_3 exists on the surface. Equation (15) is essentially a dehydration reaction accompanied by oxygen evolution, due to lack of hydrogen. The Au in equation (16) will be either oxidized very rapidly, or it will make part of the underlying Au substrate, as the gold oxide layer is very thin. In fact, equation (17) can also be considered a disproportionation reaction, in which a lower valence hydrous metal oxide disproportionates into a higher valence metal oxide and the metal, under the release of water and dioxygen. The oxidized gold surface is very rough, covered by non-ordered oxide, and the roughening process seems to be initiated by the formation of the gold(III) hydroxide. The SERS and DFT results presented here (and those by Yeo *et al.*[9]) would indicate that O_2 does not form all of a sudden, but a precursor is existent already within the oxide, probably somehow related to highly non-ordered structure. The idea of such a peroxidic species existing within the oxide layer is in fact not new.[33, 35] This species is released as the more stable molecular oxygen as soon as the transition to the β-oxide occurs.

In brief, the key ingredients of this new model for oxygen evolution are: (i) peroxide or O-O species already exists within the thin 3D non-ordered oxide, (ii) the first oxygen that is released evolves from this species (which is not a pure surface species) as a result of a change in hydration state of the oxide film, by oxide decomposition or oxide disproportionation, at least initially at the onset potential. Of course, after this initial oxygen release, or at higher potentials, other mechanisms may also be involved, more similar to the

oxygen exchange mechanisms concluded from earlier online mass spectrometry measurements.[23-25]

2.5. Conclusions

In search for a more atomic-level understanding of the mechanism(s) through which water splits electrochemically, we have revisited the electrocatalysis of O_2 evolution on gold electrodes through a variety of experimental techniques and DFT calculations. *In situ* SERS measurements showed the appearance of a peak located at 810 cm^{-1} at potentials over 1.4 V vs. RHE, while the OER only starts at potentials around 2.0 V vs. RHE. Isotopic labeling and DFT calculations help assigning this peak to an O-O stretching of *OOH species presumably incorporated into a highly disordered surface oxide. DFT calculations confirm that the oxidation of the electrode as the potential is successively increased should be accompanied by a significant roughening and dehydration of the surface. OLEMS measurements show the existence of an oxide-layer depletion mechanism at early stages (~2.0 V vs. RHE) of the OER. This initial evolution of oxygen consisting of two oxygen atoms from the surface oxide suggests an oxide decomposition or oxide disproportionation step. At higher electrode potentials (~2.05 V vs. RHE), O_2 is evolved from a combination of oxygen atoms from the surface oxide and water. These results show that electrocatalytic surfaces for oxygen evolution may undergo dynamic changes during the advance of the reactions, that several pathways are possible for a given reaction at different potentials, and that, most significantly, the oxygen evolved on a gold electrode at the onset potential appears to be the product of an oxide decomposition step.

2.6. Acknowledgments

This research is financed in part by the BioSolar Cells open innovation consortium, supported by the Dutch Ministry of Economic Affairs, Agriculture and Innovation**.** Financial support from the Netherlands Organization for Scientific Research (NWO) and the National Research School Catalysis (NRSC) is gratefully acknowledged. We also acknowledge the Stichting Nationale Computerfaciliteiten (National Computing

Facilities Foundation, NCF) for the use of their supercomputer facilities, with financial support from the NWO. Dr. F. Calle-Vallejo is kindly acknowledged for his computational contributions to the project. Special thanks to C. de Munck for his assistance with the OLEMS experiments.

REFERENCES

(1) de Levie, R. *J. Electroanal. Chem.* **1999**, *476*, 92.

(2) Paets van Troostwijk, A.; Deiman, J. R. *Obs. Phys.* **1789**, *35*, 369.

(3) Dau, H.; Limberg, C.; Reier, T.; Risch, M.; Roggan, S.; Strasser, P. *Chemcatchem* **2010**, *2*, 724.

(4) Lewis, N. S.; Nocera, D. G. *Proc. Natl. Acad. Sci. U. S. A.* **2006**, *103*, 15729.

(5) Matsumoto, Y.; Sato, E. *Materials Chemistry and Physics* **1986**, *14*, 397.

(6) Trasatti, S. *J. Electroanal. Chem.* **1980**, *111*, 125.

(7) Rossmeisl, J.; Logadottir, A.; Norskov, J. K. *Chem. Phys.* **2005**, *319*, 178.

(8) Rossmeisl, J.; Qu, Z. W.; Zhu, H.; Kroes, G. J.; Norskov, J. K. *J. Electroanal. Chem.* **2007**, *607*, 83.

(9) Yeo, B. S.; Klaus, S. L.; Ross, P. N.; Mathies, R. A.; Bell, A. T. *ChemPhysChem* **2010**, *11*, 1854.

(10) Lai, S. C. S.; Kleyn, S. E. F.; Rosca, V.; Koper, M. T. M. *Journal of Physical Chemistry C* **2008**, *112*, 19080.

(11) Gao, P.; Gosztola, D.; Leung, L. W. H.; Weaver, M. J. *J. Electroanal. Chem.* **1987**, *233*, 211.

(12) Wonders, A. H.; Housmans, T. H. M.; Rosca, V.; Koper, M. T. M. *J Appl Electrochem* **2006**, *36*, 1215.

(13) Kresse, G.; Furthmuller, J. *Phys. Rev. B* **1996**, *54*, 11169.

(14) Perdew, J. P.; Burke, K.; Ernzerhof, M. *Phys. Rev. Lett.* **1996**, *77*, 3865.

(15) Monkhorst, H. J.; Pack, J. D. *Phys. Rev. B* **1976**, *13*, 5188.

(16) Methfessel, M.; Paxton, A. T. *Physical Review B* **1989**, *40*, 3616.

(17) Kresse, G.; Joubert, D. *Phys. Rev. B* **1999**, *59*, 1758.

(18) Nørskov, J. K.; Rossmeisl, J.; Logadottir, A.; Lindqvist, L.; Kitchin, J. R.; Bligaard, T.; Jónsson, H. *The Journal of Physical Chemistry B* **2004**, *108*, 17886.

(19) Man, I. C.; Su, H.-Y.; Calle-Vallejo, F.; Hansen, H. A.; Martinez, J. I.; Inoglu, N. G.; Kitchin, J.; Jaramillo, T. F.; Norskov, J. K.; Rossmeisl, J. *Chemcatchem* **2011**, *3*, 1159.

(20) Tripkovic, V.; Bjorketun, M. E.; Skulason, E.; Rossmeisl, J. *Phys. Rev. B* **2011**, *84*.

(21) Trasatti, S. *Pure Appl. Chem.* **1986**, *58*, 955.

(22) Desilvestro, J.; Weaver, M. J. *Journal of Electroanalytical Chemistry and Interfacial Electrochemistry* **1986**, *209*, 377.

(23) Wohlfahrt-Mehrens, M.; Heitbaum, J. *Journal of Electroanalytical Chemistry and Interfacial Electrochemistry* **1987**, *237*, 251.

(24) Fierro, S. p.; Nagel, T.; Baltruschat, H.; Comninellis, C. *Electrochem. Commun.* **2007**, *9*, 1969.

(25) Macounova, K.; Makarova, M.; Krtil, P. *Electrochem. Commun.* **2009**, *11*, 1865.

(26) Conway, B. E. *Prog. Surf. Sci.* **1995**, *49*, 331.

(27) Angersteinkozlowska, H.; Conway, B. E.; Hamelin, A.; Stoicoviciu, L. *Electrochimica Acta* **1986**, *31*, 1051.

(28) Barnartt, S. *J. Electrochem. Soc.* **1959**, *106*, 991.

(29) Trasatti, S.; Petrii, O. A. *Journal of Electroanalytical Chemistry* **1992**, *327*, 353.

(30) Laitinen, H. A.; Chao, M. S. *J. Electrochem. Soc.* **1961**, *108*, 726.

(31) Nicol, M. *Gold Bulletin* **1980**, *13*, 46.

(32) Pourbaix, M. *Atlas of Electrochemical Equilibria in Aqueous Solutions*; Second English ed.; National Association of Corrosion Engineers: Houston, Texas, 1974.

(33) Puddephatt, R. *The Chemistry of Gold*; Elsevier: New York, 1978.

(34) Peuckert, M.; Coenen, F. P.; Bonzel, H. P. *Surf. Sci.* **1984**, *141*, 515.

(35) Juodkazis, K.; Juodkazyte, J.; Jasulaitiene, V.; Lukinskas, A.; Sebeka, B. *Electrochem. Commun.* **2000**, *2*, 503.

(36) Stadnichenko, A. I.; Koshcheev, S. V.; Boronin, A. I. *Moscow University Chemistry Bulletin* **2007**, *62*, 343.

(37) Weiher, N., Freie Universitaet, 2003.

(38) Angersteinkozlowska, H.; Conway, B. E.; Hamelin, A.; Stoicoviciu, L. *Journal of Electroanalytical Chemistry* **1987**, *228*, 429.

(39) Schneeweiss, M. A.; Kolb, D. M. *Solid State Ionics* **1997**, *94*, 171.

(40) Xia, S. J.; Birss, V. I. *J. Electroanal. Chem.* **2001**, *500*, 562.

(41) Hammer, B.; Hansen, L. B.; Norskov, J. K. *Phys. Rev. B* **1999**, *59*, 7413.

(42) Tripkovic, V.; Skulason, E.; Siahrostami, S.; Norskov, J. K.; Rossmeisl, J. *Electrochim. Acta* **2010**, *55*, 7975.

(43) Nakamoto, K. *Infrared and Raman spectra of Inorganic and Coordination Compounds*; 4th ed.; John Wiley & Sons: Milwaukee, 1986.

Chapter 3

Electrochemical and spectroelectrochemical characterization of an iridium-based molecular catalyst for oxygen evolution: turnover frequencies, stability and electrolyte effects

ABSTRACT

We present a systematic electrochemical and spectroelectrochemical study of the catalytic activity for water oxidation of an iridium-N-dimethylimidazolin-2-ylidene (Ir-NHC-Me_2) complex adsorbed on a polycrystalline gold electrode. The work aims to understand the effect of the electrolyte properties (anions and acidity) on the activity of the molecular catalyst and check its stability towards decomposition. Our results show that the iridium complex displays a very strong dependence on the electrolyte properties such that large enhancements in catalytic activity may be obtained by adequately choosing pH and anions in the electrolyte. The stability of the adsorbed compound was investigated *in situ* by Surface Enhanced Raman Spectroscopy and Online Electrochemical Mass Spectrometry showing that the catalyst exhibits good stability under anodic conditions, with no observable evidence for the decomposition to iridium oxide.

This chapter has been published in: Diaz-Morales, O.; Hersbach, T. J. P., Hetterscheid, D. G. H; Reek, J. N. H and Koper M.T.M. *J. Am. Chem. Soc.* **2014**, 136, 10432-10439.

3.1. Introduction

Since the discovery of the ruthenium blue dimer system by Meyer[1], many molecular water oxidation catalysts have been published in literature[2-4]. Especially ruthenium based systems have been extensively studied,[5-20] but also manganese,[21-23] iron,[24,25] cobalt,[26-28] copper[29-31] and iridium[32-42] catalysts have been addressed. The catalytic activity of these systems for water oxidation is usually studied using sacrificial stoichiometric reagents.[43] Detailed (spectro-)electrochemical studies of dissolved or immobilized catalytic complexes for water oxidation are still rare. The use of sacrificial oxidants makes difficult to properly define the thermodynamic driving force for the water oxidation reaction. An unequivocal comparison between different systems is often hampered by varying reaction conditions and the associated lack of a clearly defined oxidation potential. The importance of controlling the oxidation potential in evaluating charge transfer rates follows from the Marcus theory for electron transfer reactions, in which the thermodynamic driving force η features prominently.[44] Knowing the reaction rate or Turnover Frequency (TOF) at a well-specified overpotential is also mandatory for assessing the suitability and efficiency of the catalyst in relation to its application in a future device.

In homogeneous catalysis studies of the water oxidation reaction, Cerium Ammonium Nitrate (CAN) is frequently used as a chemical oxidant, and its corresponding oxidation potential follows from the Nernst equation:

$$E_{eq} = E^0 + \frac{RT}{nF}\ln\left(\frac{[Ce^{4+})]}{[Ce^{3+}]}\right) \qquad (1)$$

where E^0 is the standard redox potential of the couple Ce^{3+}/Ce^{4+}, *i.e.* 1.72 V vs. SHE,[45] R the gas constant, T temperature, n=1 the number of electrons transferred, F the Faraday constant and $[Ce^{4+}]$, $[Ce^{3+}]$ are, respectively, the activities of Ce^{4+} and Ce^{3+} in solution. Experiments are usually performed by adding solutions of cerium(IV) so that the initial concentration of cerium(III) is zero, under which conditions the oxidation potential is poorly defined (theoretically, it is infinitely high). Moreover, the oxidation potential will

actually change (*i.e.*, lower) as the reaction progresses, since Ce^{4+} is converted into Ce^{3+} so that their concentrations change in time.

An additional complication of using CAN is that, since the nitrate coordinating to cerium(IV) is partly displaced by water, the actual structure of CAN is poorly defined and very acidic conditions are employed as the Ce^{4+} coordinated aqua ligands readily deprotonate.[46] DFT calculations have shown that the resulting cerium hydroxide is best described as a Ce(III) complex with a hydroxyl radical coordinated.[17] This can possibly lead to undesirable pathways involving transfer of hydroxyl radicals that are not relevant to water oxidation. Furthermore, Berlinguette and coworkers showed that part of the dioxygen evolved during ruthenium mediated water oxidation with CAN, contains oxygen atoms that are derived from nitrate rather than from water.[46] Another popular oxidant is periodate, which is stable at milder conditions compared to CAN[43]; however, it contains atomic oxygen that undergoes fast exchange equilibrium with water. For that reason, O-atom labeling studies cannot confirm whether the dioxygen produced derives from water or periodate.[47] In a recent theoretical study, we showed that atomic oxygen transfer from periodate to the iridium catalyst under study is very facile, and by *in situ*-MS spectroscopy we identified catalytic species that point to the occurrence of such non relevant elementary steps[48].

In addition to the sometimes poorly understood identity of the chemical oxidant under reactive conditions, identification of the active catalyst can be an issue. This has almost exclusively been carried out using sacrificial reagents. On basis of electrochemical experiments, it was claimed by the groups of De Groot and Lin that iridium complexes bearing cyclopentadienyl ligands may be stable, as no time dependence of the observed catalytic activity was observed.[49,50] On the other hand, Crabtree and coworkers reported the complete deterioration of $[IrC_p^*(OH_2)_3]^{2+}$ (C_p^* = pentamethylcyclopentadienyl), leading to the formation of an amorphous phase of iridium oxide on the electrode.[51-53] In agreement with the former studies, our group[54] as well as others[55] showed using DFT calculations that iridium catalysts bearing the Cp* ligand can be active for catalytic water oxidation and those catalyst would be sufficiently stable. Crabtree and coworkers published that the Cp*

ligand is readily lost and that binuclear molecular complexes bearing the remaining organic ligands are the true active species, using sacrificial periodate as a chemical oxidant[56]. Others have shown that complete deterioration of molecular systems leading to formation of iridium oxide nanoparticles can take place,[32,57,58] yet this seems to be a relative sluggish reaction[33] which is strongly dependent on the iridium concentration employed. It was also shown that these nanoparticles contain significant amounts of cerium. It is not clear to which extent these phenomena are dependent on the chemical oxidants used, and whether this chemistry can actually be translated meaningfully to the electrochemically driven dioxygen evolution reaction.

In contrast to catalytic oxidation by stoichiometric oxidants, oxidation by electrochemical techniques allows for better defined reaction conditions. The relevant oxidation potential is directly related to the applied electrode potential, leaving no doubt about the thermodynamic driving force. Provided that the electrode material used to apply the oxidizing potential is stable under the conditions of water oxidation, there are no negative or unknown side effects of chemically unstable oxidants. Furthermore, if the molecular catalyst is immobilized on the inert electrode surface, mass transport of the catalyst may be ignored and the identity and stability of the immobilized catalyst may be probed by surface sensitive spectro-electrochemical techniques. Such studies are also more meaningful in relation to real application of water oxidation catalysis in the production of solar fuels.

In this work, we perform an electrochemical and spectro-electrochemical study of the water oxidation reaction using the recently introduced IrCp*-N-dimethylimidazolin-2-ylidene catalyst, immobilized on polycrystalline gold electrodes. We use steady state voltammetry to demonstrate the significant influence of the electrolyte composition in terms of pH and anion identity on the TOF of the catalyst. We show *in situ* Surface Enhanced Raman Spectroscopy (SERS) evidences that the adsorbed catalyst does not form IrO_x nanoparticles. Moreover, we show by the combination of electrochemical experiments with on-line electrochemical mass spectroscopy (OLEMS) that the adsorbed catalyst

produces only O_2 under reactive conditions, and no CO_2, testifying to the stability of the organic ligands.

3.2. Experimental Section

All glassware was thoroughly cleaned before starting experiments by boiling in a 1:3 mixture of concentrated HNO_3/concentrated H_2SO_4 to remove organic contaminations after which it was boiled five times in water. The water used for cleaning glassware and preparing solutions was demineralized and ultrafiltrated by a Millipore Milli-Q system (resistivity > 18.2 MΩ cm and TOC < 5ppb). When not in use, the glassware was stored in an aqueous solution of 0.5 M H_2SO_4 and 1 g/L $KMnO_4$. To clean the glassware from permanganate solution, it was rinsed thoroughly with water and then immersed in a solution 1:1 of concentrated H_2SO_4 and 30% H_2O_2 to remove all particles of MnO_2, after which it was rinsed with water again and boiled five times in water.

Electrolyte solutions were prepared with high quality chemicals, $HClO_4$ (VWR, Normatom), H_2SO_4 (Merck, Ultrapur), HNO_3 (Merck, Suprapur), H_3PO_4 (Merck, Suprapur), NaH_2PO_4 (Merck, Suprapur), $NaClO_4$ (Merck, Emsure) and NaOH (Sigma-Aldrich, trace metals). Dissolved oxygen in solutions was removed prior to measurements by purging with argon (purity grade 5.0) for at least 30 min, and the argon was kept flowing above the solution during experiments. Experiments with ^{18}O enriched water were performed with 98% ^{18}O water (GMP standard, from CMR) and experiments in deuterated media used D_2O (Sigma-Aldrich, 99.9 atom % D).

Electrochemical measurements were carried out in a home-made three-electrode and two compartment cell with the reference electrode separated by a Luggin capillary. The working electrode was a homemade gold rotating disk electrode RDE (ϕ = 4.6 mm), a gold wire was used as counter electrode and a reversible hydrogen electrode (RHE) was used as a reference; a platinum wire was connected to the reference electrode through a capacitor of 10 μF, acting as a low-pass filter to reduce the noise in the low current measurements. All experiments were performed in hydrodynamic conditions at 1500 RPM, using a home-made rotator. Electrochemical measurements were performed with a potentiostat

PGSTAT12 (Metrohm- Autolab). Before and between measurements, the RDE electrode was first polished with 0.3 μm and 0.05 μm alumina paste (Buehler Limited). Subsequently the electrode was ultrasonicated for 5 minutes to remove polishing particles.

The molecular catalyst used in this work is iridium-N-dimethylimidazolin-2-ylidene, which was synthesized by Hetterscheid and Reek,[32] with the structure shown in Figure 1. This compound was dissolved in water to give a solution with nominal concentration of $1x10^{-3}$ M (catalyst solution). Na-exchanged Nafion solution was prepared by mixing one part of Nafion (5% wt., Sigma-Aldrich) with one part of NaOH 0.05 M. The solution to drop cast on the electrode was prepared by mixing one part of catalyst solution with one part of Na-exchanged Nafion; 5 μL of this solution was drop casted on the gold working electrodes and dried under vacuum conditions. Currents in this work will be reported as $I_{Normalized}$, which is the measured current divided by the amount (in μmol) of catalyst drop casted on the electrode, considering the nominal concentration of solution used and volume added.

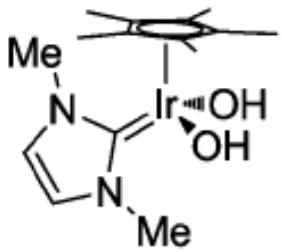

Figure 1. Structure of the iridium-N-dimethylimidazolin-2-ylidene complex.[32]

In situ Surface Enhanced Raman Spectroscopy (SERS) was performed with a confocal Raman microscope (LabRam HR, Horiba Yobin Yvon) with a 50X objective. A He/Ne laser (633 nm) was used as excitation source. Backscattered light was filtered by a 633 nm edge filter, directed to the spectrograph and to the detector. Details of the setup can be found in references 59 and 60. Electrochemical SERS experiments were made with a

μAutolab Type III potentiostat/galvanostat (Metrohm-Autolab), using a home-made electrochemical cell with a small electrolyte volume necessary for the $H_2{}^{18}O$ experiments. The electrochemical cell has one compartment and three electrodes, a gold wire as counter electrode, Ag/AgCl (sat. KCl) as reference electrode (potentials were recalculated and reported versus RHE) and a roughened gold surface as working electrode. Prior to each measurement, the working electrode was mechanically polished to mirror finish using aqueous diamond pastes (Buehler Limited) with different grain sizes to 0.25 μm, rinsed with Milli-Q water and ultrasonicated during 5 min to remove all residuals of mechanical polishing. Next the gold electrode was electrochemically roughened by 25 oxidation-reduction cycles (ORC) in a 0.1 M solution of KCl. The ORC were performed between -0.30 and 1.20 V vs. SCE, during which the potential was held for 30 seconds at the negative limit and for 1.3 seconds at the positive limit, a method reported to give a brownish surface that is SERS active.[61] SERS measurements were carried out drop casting the iridium complex without Na-exchanged Nafion, to avoid the appearance of strong signals in the spectrum, signals related to $R–HSO_3$ groups in Nafion.

Online Electrochemical Mass Spectrometry (OLEMS) experiments were performed using an EvoLution mass spectrometer system (European Spectrometry systems Ltd). The setup has a mass detector (Prisma QMS200, Pfeiffer) which was brought to vacuum using both a turbo molecular pump (TMH-071P, Pfeiffer, flow rate 60 L s^{-1}) and a rotary vane pump (Duo 2.5, Pfeiffer; flow rate 2.5 m^3 h^{-1}). During measurements, the pressure inside the mass detector chamber was around 10^{-6} mbar. Volatile reaction products were collected from electrode interface by a small inlet tip positioned close (~10 μm) to electrode surface using a micrometric screw system and a camera.[62] The inlet tip is made with a porous Teflon cylinder (Porex®) mounted in a Kel-F holder. The inlet is connected to the mass detector through a PEEK capillary. Before use, the inlet tip was cleaned during 15 min with a solution 0.2 M $K_2Cr_2O_7$ in 2 M H_2SO_4 and rinsed thoroughly with water. The electrochemical cell used for these experiments is a two compartment cell with three electrodes, using a gold bead electrode and a gold wire as working and counter electrode, respectively; the reference electrode was a RHE separated from the main cell by a Luggin capillary. Before each measurement, the working electrode was electrochemically cleaned;

the electrode was first oxidized in dilute sulfuric acid by applying 10 V for 30 s, using a graphite bar as counter electrode. Subsequently the gold oxide formed was removed by dipping the working electrode in a 6 M HCl solution for 30 s.

3.3. Results and Discussion

3.3.1. Effect of electrolyte anions

In a previous communication we reported[32] the catalytic activity towards oxygen evolution for the Ir-NHC-Me_2 catalyst in aqueous solution, using cerium(IV) ammonium nitrate as chemical oxidant ($E^0_{Ce(IV)/Ce(III)}$ = 1.72 V vs. SHE [45]) and showed that under the investigated conditions the complex exhibits a turnover frequency[2] of 0.34 mol O_2 $mol_{catalyst}^{-1}$ s^{-1}, which was among the highest catalytic activities reported for an iridium based water oxidation molecular catalyst at the time. Here, we report the electrocatalytic activity of the complex immobilized on a gold surface including the effect of working conditions, such as electrolyte anions and pH.

Figure 2 shows the current-potential profiles obtained during water oxidation catalyzed by the iridium-N-dimethylimidazolin-2-ylidene on gold at pH 1 in electrolytes with different anions. The catalytic activity decreases in the order $HClO_4$ > H_2SO_4> H_3PO_4 > HNO_3. The pH in each solution was verified with a pH meter and it was found that it was 1.0 $\pm$ 0.1, so that we can exclude any pH effect in Figure 2.

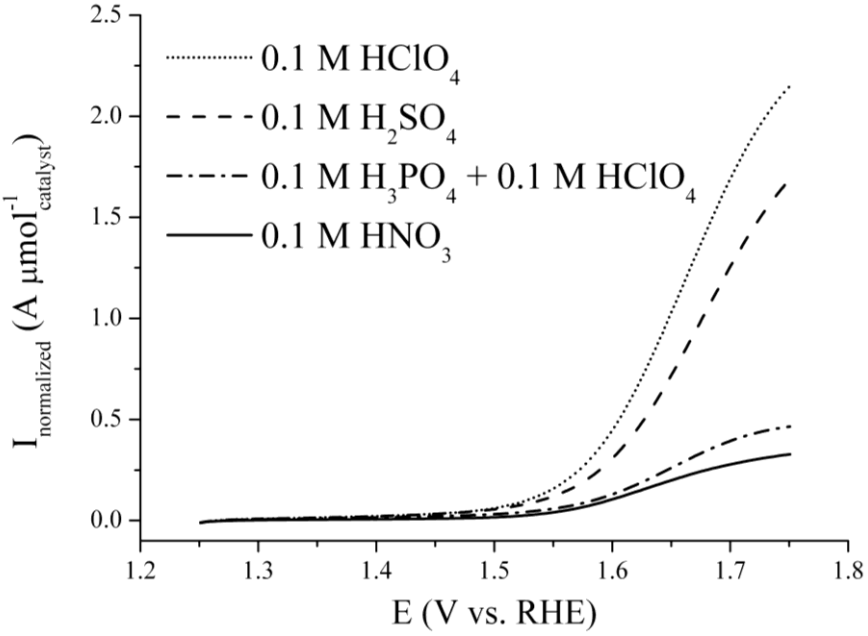

Figure 2. Current-potential profile for water oxidation catalyzed by iridium-N-dimethylimidazolin-2-ylidene immobilized on a gold rotating disk electrode, obtained under hydrodynamic conditions at pH 1 in different electrolytes. Scan rate: 0.005 V s^{-1}. Rotation rate: 1500 RPM.

The trend observed in Figure 2 shows the importance of the electrolyte anion for the water oxidation catalysis. The varying strength of the coordination of the anions to the iridium center of the molecular complex is the most likely explanation for the trend. It has been reported that metallic iridium binds NO quite strongly,[63] leading to poisoning of the electrode surface during nitrite reduction. Furthermore, the evidences reported by Ison *et al.*[64] show that nitrate and sulfate actually coordinate to iridium species bearing N-heterocyclic carbenes and pentamethylcyclopentadienyl ligands. Therefore, we assume that, of the anion shown in Figure 1, the nitrate anion binds to the iridium centers the strongest, so that it blocks their access for water oxidation. This was experimentally verified in aqueous solution for the iridium catalyst studied in this work with electro-spray ionization mass spectrometry (ESI-MS) in nitrate and sulfate media (see Figures B1-B2 in Appendix B). Following the same reasoning, perchlorate should coordinate the weakest, and is indeed

known to absorb rather weakly on electrode surfaces[65-68] so it is expected that catalytic activity shows its maximum in this medium. The other anions show intermediate activities which suggest that they can bind to the iridium sites but not as strong as nitrate does. It has been reported that iridium electrodes can reduce nitrate in sulfuric acid media,[69] which suggest bisulphate should adsorb less strongly than nitrate on iridium surfaces, in agreement with the higher catalytic activity for oxygen evolution in sulfuric media. Sulfate anions adsorbs weaker than phosphate species;[67] therefore, it is reasonable that bisulphate (lower charge) adsorbs more weakly than dihydrogenphosphate, explaining the higher catalytic activity in sulfuric acid media compared to phosphoric acid.

The results above show that when studying the catalytic activity of iridium-based molecular catalysts using nitrate salts of cerium (IV) as chemical oxidant, one should be aware the inhibitory effect of nitrate. Kinetic parameters such as turnover frequency or turnover number for water oxidation measured in that way may therefore be lower than their optimal values.

Turnover frequencies extracted from the electrochemical experiments with the immobilized catalyst in Figure 1 are summarized in Table 1 and compared to the value reported in solution.[32] The TOFs were taken at the standard equilibrium potential for the couple Ce^{4+}/Ce^{3+}, 1.72 V vs. SHE[45] or 1.66 V vs. RHE at pH 1, as that was the chemical oxidant used for the homogeneous experiment. We note however that the real oxidation potential in homogeneous experiments is different, due to lack of Ce^{3+} at the beginning of the experiment, as explained in the Introduction. Electrochemical currents were converted into turnover frequencies using Faraday's law, *i.e.* TOF = $I_{normalized}$ / 4*F*, assuming 100% faradaic efficiency for the reaction (1):

$$2H_2O \rightarrow O_2 + 4H^+ + 4e^- \qquad (1)$$

Table 1. Turnover frequency for water oxidation by iridium-N-dimethylimidazolin-2-ylidene in solution and immobilized on the gold electrode surface.

	Turnover frequency (mol O_2 [mol catalyst]$^{-1}$ s^{-1})	
Anion	**Catalyst in solution[2] pH= 0.8**	**Immobilized catalyst pH=1, *E*= 1.66 V vs. RHE**
Perchlorate	----------	2.9 $\pm$ 0.2
Hydrogen sulfate	----------	2.2 $\pm$ 0.2
Dihydrogen phosphate	----------	1.1 $\pm$ 0.4
Nitrate	0.34	0.8 $\pm$ 0.1

The reported turnover frequency for the molecular complex in solution[2] is in reasonable agreement with the value reported in this work using the immobilized catalyst, but we emphasize that a quantitative comparison is not meaningful for the reasons mentioned in the Introduction. Also, one should consider the difference in concentration of nitrate used in each case; the results in this work were obtained in 0.1 M solution of nitric acid, meaning a nominal concentration of 0.1 M in nitrate, while the kinetic data reported for the catalyst in solution[2] were obtained in 0.09 M of $(NH_4)_2Ce(NO_3)_6$. In the latter case, the nominal concentration of nitrate in solution will depend on how labile the nitrate groups in the cerium complex are. The nitrate concentration may be almost six times higher than used in this work, having a corresponding effect on the catalytic activity.

Turnover frequencies in table 1 send a clear message in terms of the conditions that should be used to study the catalytic activity for oxygen evolution of molecular catalysts in solution: in selecting the chemical oxidant to drive the reaction, one should consider the effect of the anions because they may and actually will affect the kinetic data obtained. The best option is not to use chemical oxidants at all and drive the reaction electrochemically at controlled pH, in which case the overpotential will be properly defined along the experiment.

3.3.2. Effect of the pH on the catalytic activity of the molecular complex

Figure 3 shows the current-potential profile for water oxidation in perchlorate solutions at different pH. Interestingly, there is a maximum in activity at a pH close or higher than 3, while the activity is almost negligible in alkaline pH. Figure 3 suggests the existence of a pH for which the activity reaches a maximum value between pH 3 and 11, but the intermediate pH's are not achievable in perchlorate media due to the poor buffering capacity of this electrolyte. Additional experiments were performed in phosphate buffer to study the catalytic activity at intermediate pH and results are summarized in Figure 4, showing that in phosphate media the maximum appears to be located around pH 4.

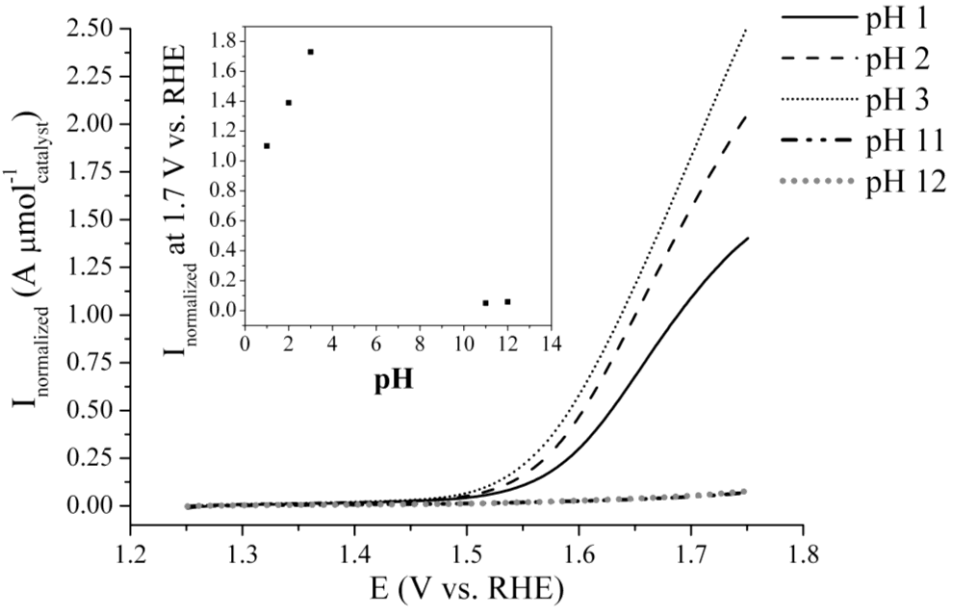

Figure 3. Current-potential profile for water oxidation catalyzed by iridium-N-dimethylimidazolin-2-ylidene immobilized on gold, obtained under hydrodynamic conditions at different pH in perchlorate media. Scan rate: 0.005 V s^{-1}. Rotation rate: 1500 RPM. Insert: Current (activity) measured at 1.7 V vs. RHE.

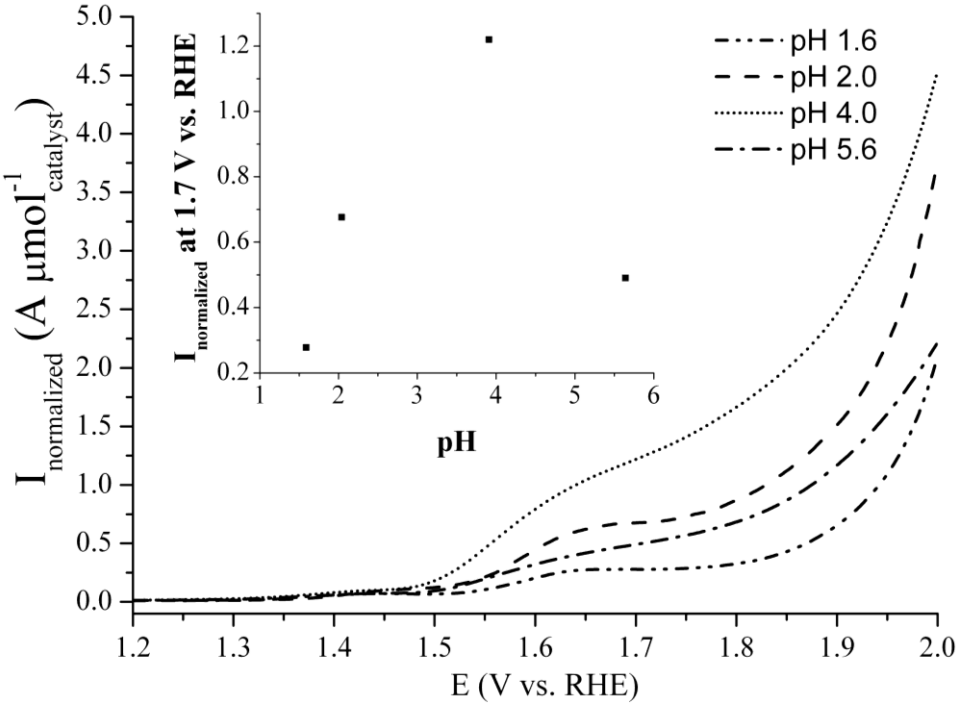

Figure 4. Current-potential profiles for water oxidation catalyzed by iridium-N-dimethylimidazolin-2-ylidene immobilized on gold, obtained with phosphate buffer at different pH. Scan rate: 0.001 V s^{-1}. Insert: Current (activity) measured at 1.7 V vs. RHE.

Nakagawa *et al.*[70] studied the catalytic activity of mesoporous iridium oxide as a function of pH, in phosphate buffer; their results showed that it does not depend on pH. Therefore, the strong pH dependence of the catalytic activity of the complex observed in Figure 3 and 4 supports the idea that the organometallic structure of the catalyst remains intact under the anodic working conditions, meaning that the active form of the catalyst is not iridium oxide as it has been reported in the literature[56,71] for similar molecular catalysts. In addition, the pH dependence of the catalytic activity suggests the importance of decoupled proton-electron transfer steps in the overall OER mechanism.[72]

The above results show that the catalytic activity of a given molecular compound for water oxidation can be tuned by carefully controlling the pH and anions. In the specific case studied here, the activity of iridium-N-dimethylimidazolin-2-ylidene complex for oxygen evolution, reported to be among the highest reported[32], can be enhanced *ca.* 20 times by working in perchlorate media at a pH close to 3.

3.3.3. The stability of the molecular catalyst: SERS and OLEMS experiments.

In situ surface enhanced Raman spectra with the Ir-NHC-Me_2 complex immobilized on roughened gold were acquired in 0.1 M $HClO_4$ in a potential region prior to water oxidation as a function of the applied potential, as summarized in Figure 5.

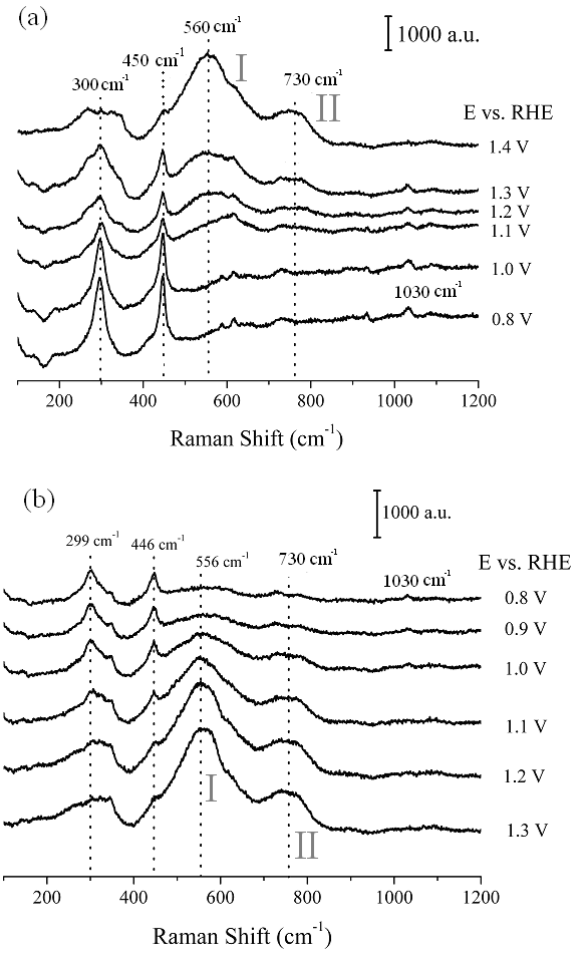

Figure 5. SERS spectra of by iridium-N-dimethylimidazolin-2-ylidene on gold, acquired under potentiostatic conditions in 0.1 M $HClO_4$: a) Spectra obtained by increasing the potential stepwise from 0.8 to 1.4 V vs. RHE. b) Spectra acquired after a) and by decreasing the potential stepwise back to 0.8 V vs. RHE.

The spectra in Figure 5a show two peaks located at *ca.* 300 cm^{-1} and 450 cm^{-1} at low potential which remain visible at positive potentials albeit with lower intensity. These peaks did not show isotope shifts in deuterated or ^{18}O media (see Figure B3 in Appendix B) which suggest that the vibration modes do not involve protons or oxygen atoms. Raman spectra were also obtained for the Di-μ-chloro-bis[chloro(pentamethylcyclopentadienyl)iridium(III)], and the Di-chloro-N-dimethylimidazolin-2-ylidene-(penthamethylcyclopentadienyl)iridium(III) complexes in normal Raman mode (see Figure B4 in Appendix B). The spectra of the first compound shows two peaks at *ca.* 450 cm^{-1} and 460 cm^{-1}, which merges into one at *ca.* 450 cm^{-1} for the N-dimethylimidazolin-2-ylidene compound, which has only one Cp^* ligand. Other metal-cyclopentadienyl complexes like ruthenocene and osmocene are reported[73] to show bending of the cyclopentadienyl ring in the region around 450 cm^{-1}. Comparison of the normal Raman spectra of Di-μ-chloro-bis[chloro(pentamethylcyclopentadienyl) iridium(III)], and Di-chloro-N- dimethylimidazolin-2-ylidene-(penthamethylcyclopentanienyl)iridium(III) with the surface enhanced Raman in Figure 5 in combination with the evidence reported for the metalocenes, let us conclude that the peak at 450 cm^{-1} corresponds to the bending vibration of the iridium-Cp^* bond. Neither the Di-μ-chloro-bis[chloro(pentamethylcyclopentadienyl) iridium(III)] compound nor the Di-chloro-N-dimethylimidazolin-2-ylidene-(penthamethylcyclopentanienyl) iridium(III) complex showed Raman peaks at 300 cm^{-1}, suggesting that the observed peak in Figure 4 does not correspond to vibrational modes of the absorbed complex, although we cannot make a proper assignment of the peak at 300 cm^{-1} based on our results.

Regarding to the Cp^* moiety, Crabtree *et al.*[56] reported that for an iridium-based molecular catalyst similar to the complex studied in this work, the Cp^* acts a sacrificial placeholder that is lost in the activation process of the catalyst. The evidence in that work shows that the activation process involves the formation of a planar bis-μ-oxo Di-iridium(IV) compound and the computational DFT calculations showed that this activated form of the catalyst has four Raman active vibrational modes in the regions 717-722 cm^{-1} and 525-532 cm^{-1}. Those modes are expected to be sensitive to oxygen isotope labeling, showing a shift between 28-41 cm^{-1}.

The peaks I and II in Figure 5a agree with the expected vibrations for the μ-oxo dimer proposed by Crabtree *et al*. and, as can be observed in Figure B3 in Appendix B, both peaks show sensitivity to oxygen labeling. The isotopic shifts in $^{18}OH_2$, $^{16}OH_2$ and D_2O are summarized in Table B1 in Appendix B. The shift observed in the ^{18}O labeled water also fits with that predicted for the μ-oxo dimer. Furthermore, the observed lack of an isotope shift in deuterated media would imply that the vibrational mode does not involve any protonated species.

Figure 5b shows that the peak corresponding to the Ir-Cp^* vibration (peak at *c.a.* 450 cm^{-1}) is regenerated when the potential is set back to the original values, suggesting that the dimerization process is reversible with potential and that the Cp^* is not irreversibly lost during activation process of the complex, as stated by Crabtree et al.

SER spectra of chemically synthesized IrO_x nanoparticles[70] drop casted on a gold electrode were also measured and are shown in Figure C5 of Appendix C, corresponding well with the spectra reported in the literature.[74,75] These spectra are clearly different from the spectra obtained for the iridium-N-dimethylimidazolin-2-ylidene compound, suggesting that the latter is not decomposed to iridium oxide.

The stability of the molecular complex was also confirmed by OLEMS, monitoring *in situ* the production of O_2 and CO_2 during the experiment in order to check whether the organic moieties in the complex oxidize during the catalytic oxygen evolution. Figure 6 shows the current signal and the mass signals for O_2 (m/z 32) and CO_2 (m/z 44).

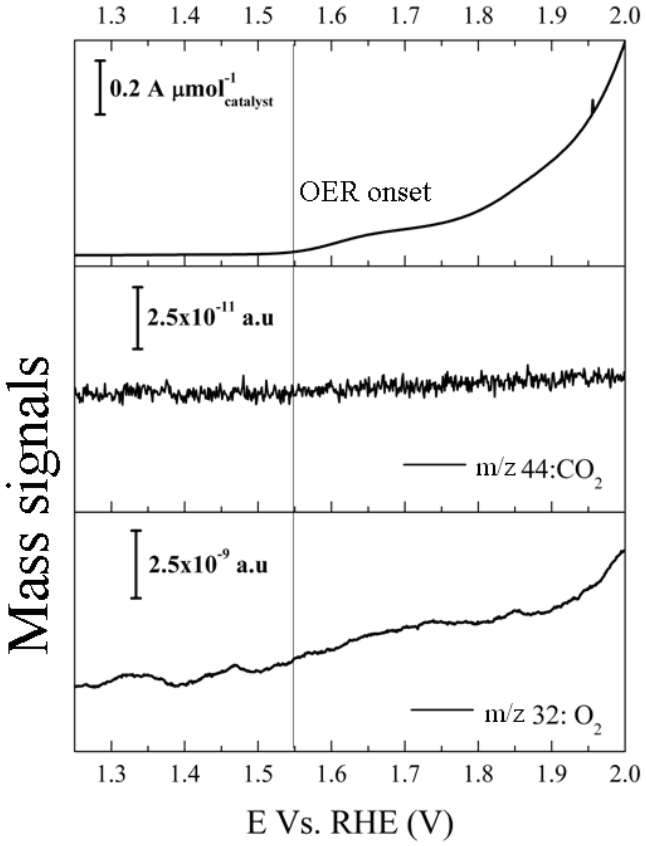

Figure 6. OLEMS signal acquired during electrochemical water oxidation in 0.1 M $HClO_4$ and catalyzed by iridium-N-dimethylimidazolin-2-ylidene on gold. Scan rate: 0.001 V s^{-1}

Figure 6 allows estimating the onset potential for the water oxidation on the iridium-N-dimethylimidazolin-2-ylidene complex as the potential at which the signal m/z 32 starts rising: *ca.*1.55 V vs. RHE. The most important feature that can be observed in Figure 6 is the lack of a potential dependence of the mass signal of CO_2; the signal is almost flat in the potential region corresponding to water oxidation. These results show that the iridium-N-dimethylimidazolin-2-ylidene compound forms negligible amounts of carbon dioxide under oxidizing conditions, suggesting that the organic moieties are stable. Combined with the

results obtained by SERS and pH dependence, we can conclude that the molecular complex studied in this work does not form iridium oxide during the catalytic reaction.

3.4. Conclusions

We studied the effect of working conditions on the activity and stability of an iridium-N-dimethylimidazolin-2-ylidene molecular catalyst adsorbed on gold by using a variety of electrochemical and spectroelectrochemical techniques. The advantage of studying immobilized molecular catalysts lies in the better defined thermodynamic driving force through the applied electrode potential, and in the ability to use spectroelectrochemical techniques to assess catalyst stability and to obtain molecular-level insight into the reaction mechanism. The turnover rate towards water oxidation of the iridium-based organometallic compound, which we define as the reaction rate per adsorbed catalyst molecule at a pre-defined electrode potential, is strongly dependent on the nature of the electrolyte anions, which may be ascribed to a competition between the anion and water for coordination, and on the electrolyte pH, with an optimal pH close to 4 and with hardly any activity in alkaline media. By suitably tuning pH and electrolyte, the TOF for water oxidation can be enhanced by a factor of 20. *In situ* SERS experiments showed that the active state of the molecular catalyst may involve a bis-μ-oxo iridium dimer that is reversibly formed when the potential is scanned to positive values. The SERS and online electrochemical mass spectrometry experiments together with the pH dependence show that the iridium-based molecular complex does not decompose into iridium oxide during the oxygen evolution reaction. As a final more general conclusion, it is essential to clearly define electrolyte pH, electrolyte anion (or electrolyte composition in general), and thermodynamic driving force (electrode potential) in any meaningful comparison of turnover frequencies between different molecular water splitting catalysts.

3.5. Acknowledgments

This work was also supported by the Netherlands Organization for Scientific Research (NWO) and in part by the BioSolar Cells open innovation consortium, supported by the Dutch Ministry of Economic Affairs, Agriculture and Innovation. Dr. D. Hetterscheid and

Prof. Dr. J. Reek are kindly acknowledged for the synthesis of the iridium complex and its MS / NMR characterization. Special thanks to T. Hersbach for his assistance with the spectroelectrochemical experiments.

REFERENCES

(1) Gersten, S. W.; Samuels, G. J.; Meyer, T. J. *J. Am. Chem. Soc.* **1982**, *104*, 4029.

(2) Hetterscheid, D. G. H.; Reek, J. N. H. *Angew. Chem. Int. Ed.* **2012**, *51*, 9740.

(3) Wasylenko, D. J.; Palmer, R. D.; Berlinguette, C. P. *Chem. Commun.* **2013**, *49*, 218.

(4) Sala, X.; Romero, I.; Rodriguez, M.; Escriche, L.; Llobet, A. *Angewandte Chemie-International Edition* **2009**, *48*, 2842.

(5) Wasylenko, D. J.; Ganesamoorthy, C.; Koivisto, B. D.; Henderson, M. A.; Berlinguette, C. P. *Inorg. Chem.* **2010**, *49*, 2202.

(6) Wasylenko, D. J.; Ganesamoorthy, C.; Henderson, M. A.; Koivisto, B. D.; Osthoff, H. D.; Berlinguette, C. P. *J. Am. Chem. Soc.* **2010**, *132*, 16094.

(7) Concepcion, J. J.; Tsai, M. K.; Muckerman, J. T.; Meyer, T. J. *J. Am. Chem. Soc.* **2010**, *132*, 1545.

(8) Concepcion, J. J.; Jurss, J. W.; Norris, M. R.; Chen, Z. F.; Templeton, J. L.; Meyer, T. J. *Inorg. Chem.* **2010**, *49*, 1277.

(9) Concepcion, J. J.; Jurss, J. W.; Brennaman, M. K.; Hoertz, P. G.; Patrocinio, A. O. T.; Iha, N. Y. M.; Templeton, J. L.; Meyer, T. J. *Acc. Chem. Res.* **2009**, *42*, 1954.

(10) Duan, L. L.; Araujo, C. M.; Ahlquist, M. S. G.; Sun, L. C. *Proc. Natl. Acad. Sci. U. S. A.* **2012**, *109*, 15584.

(11) Duan, L. L.; Bozoglian, F.; Mandal, S.; Stewart, B.; Privalov, T.; Llobet, A.; Sun, L. C. *Nat. Chem.* **2012**, *4*, 418.

(12) Nyhlen, J.; Duan, L. L.; Akermark, B.; Sun, L. C.; Privalov, T. *Angewandte Chemie-International Edition* **2010**, *49*, 1773.

(13) Duan, L. L.; Fischer, A.; Xu, Y. H.; Sun, L. C. *J. Am. Chem. Soc.* **2009**, *131*, 10397.

(14) Kaveevivitchai, N.; Chitta, R.; Zong, R. F.; El Ojaimi, M.; Thummel, R. P. *J. Am. Chem. Soc.* **2012**, *134*, 10721.

(15) Boyer, J. L.; Polyansky, D. E.; Szalda, D. J.; Zong, R. F.; Thummel, R. P.; Fujita, E. *Angewandte Chemie-International Edition* **2011**, *50*, 12600.

(16) Yamazaki, H.; Hakamata, T.; Komi, M.; Yagi, M. *J. Am. Chem. Soc.* **2011**, *133*, 8846.

(17) Yoshida, M.; Masaoka, S.; Abe, J.; Sakai, K. *Chemistry-an Asian Journal* **2010**, *5*, 2369.

(18) Lopez, I.; Ertem, M. Z.; Maji, S.; Benet-Buchholz, J.; Keidel, A.; Kuhlmann, U.; Hildebrandt, P.; Cramer, C. J.; Batista, V. S.; Llobet, A. *Angewandte Chemie-International Edition* **2014**, *53*, 205.

(19) Maji, S.; Vigara, L.; Cottone, F.; Bozoglian, F.; Benet-Buchholz, J.; Llobet, A. *Angewandte Chemie-International Edition* **2012**, *51*, 5967.

(20) Mola, J.; Dinoi, C.; Sala, X.; Rodriguez, M.; Romero, I.; Parella, T.; Fontrodona, X.; Llobet, A. *Dalton Transactions* **2011**, *40*, 3640.

(21) Karlsson, E. A.; Lee, B. L.; Akermark, T.; Johnston, E. V.; Karkas, M. D.; Sun, J. L.; Hansson, O.; Backvall, J. E.; Akermark, B. *Angewandte Chemie-International Edition* **2011**, *50*, 11715.

(22) Limburg, J.; Vrettos, J. S.; Liable-Sands, L. M.; Rheingold, A. L.; Crabtree, R. H.; Brudvig, G. W. *Science* **1999**, *283*, 1524.

(23) Limburg, J.; Vrettos, J. S.; Chen, H. Y.; de Paula, J. C.; Crabtree, R. H.; Brudvig, G. W. *J. Am. Chem. Soc.* **2001**, *123*, 423.

(24) Fillol, J. L.; Codola, Z.; Garcia-Bosch, I.; Gomez, L.; Pla, J. J.; Costas, M. *Nat. Chem.* **2011**, *3*, 807.

(25) Ellis, W. C.; McDaniel, N. D.; Bernhard, S.; Collins, T. J. *J. Am. Chem. Soc.* **2010**, *132*, 10990.

(26) Wasylenko, D. J.; Ganesamoorthy, C.; Borau-Garcia, J.; Berlinguette, C. P. *Chem. Commun.* **2011**, *47*, 4249.

(27) Yin, Q. S.; Tan, J. M.; Besson, C.; Geletii, Y. V.; Musaev, D. G.; Kuznetsov, A. E.; Luo, Z.; Hardcastle, K. I.; Hill, C. L. *Science* **2010**, *328*, 342.

(28) Dogutan, D. K.; McGuire, R.; Nocera, D. G. *J. Am. Chem. Soc.* **2011**, *133*, 9178.

(29) Barnett, S. M.; Goldberg, K. I.; Mayer, J. M. *Nat. Chem.* **2012**, *4*, 498.

(30) Zhang, M. T.; Chen, Z. F.; Kang, P.; Meyer, T. J. *J. Am. Chem. Soc.* **2013**, *135*, 2048.

(31) Chen, Z. F.; Meyer, T. J. *Angewandte Chemie-International Edition* **2013**, *52*, 700.

(32) Hetterscheid, D. G. H.; Reek, J. N. H. *Chem. Commun.* **2011**, *47*, 2712.

(33) Hintermair, U.; Hashmi, S. M.; Elimelech, M.; Crabtree, R. H. *J Am Chem Soc* **2012**, *134*, 9785.

(34) Brewster, T. P.; Blakemore, J. D.; Schley, N. D.; Incarvito, C. D.; Hazari, N.; Brudvig, G. W.; Crabtree, R. H. *Organometallics* **2011**, *30*, 965.

(35) Parent, A. R.; Blakemore, J. D.; Brudvig, G. W.; Crabtree, R. H. *Chem. Commun.* **2011**, *47*, 11745.

(36) Blakemore, J. D.; Schley, N. D.; Balcells, D.; Hull, J. F.; Olack, G. W.; Incarvito, C. D.; Eisenstein, O.; Brudvig, G. W.; Crabtree, R. H. *J. Am. Chem. Soc.* **2010**, *132*, 16017.

(37) Petronilho, A.; Rahman, M.; Woods, J. A.; Al-Sayyed, H.; Muller-Bunz, H.; MacElroy, J. M. D.; Bernhard, S.; Albrecht, M. *Dalton Transactions* **2012**, *41*, 13074.

(38) Lalrempuia, R.; McDaniel, N. D.; Muller-Bunz, H.; Bernhard, S.; Albrecht, M. *Angewandte Chemie-International Edition* **2010**, *49*, 9765.

(39) McDaniel, N. D.; Coughlin, F. J.; Tinker, L. L.; Bernhard, S. *J. Am. Chem. Soc.* **2008**, *130*, 210.

(40) Bucci, A.; Savini, A.; Rocchigiani, L.; Zuccaccia, C.; Rizzato, S.; Albinati, A.; Llobet, A.; Macchioni, A. *Organometallics* **2012**, *31*, 8071.

(41) Savini, A.; Bellachioma, G.; Bolano, S.; Rocchigiani, L.; Zuccaccia, C.; Zuccaccia, D.; Macchioni, A. *Chemsuschem* **2012**, *5*, 1415.

(42) Savini, A.; Bellachioma, G.; Ciancaleoni, G.; Zuccaccia, C.; Zuccaccia, D.; Macchioni, A. *Chem. Commun.* **2010**, *46*, 9218.

(43) Parent, A. R.; Crabtree, R. H.; Brudvig, G. W. *Chem. Soc. Rev.* **2013**, *42*, 2247.

(44) Marcus, R. A. *Angewandte Chemie International Edition in English* **1993**, *32*, 1111.

(45) West, R. *Handbook of Chemistry and Physics*; 53rd ed.; CRC Press Cleveland, 1972.

(46) Wasylenko, D. J.; Ganesamoorthy, C.; Henderson, M. A.; Berlinguette, C. P. *Inorg. Chem.* **2011**, *50*, 3662.

(47) Pecht, I.; Luz, Z. *J. Am. Chem. Soc.* **1965**, *87*, 4068.

(48) Hetterscheid, D. G. H.; Reek, J. N. H. *Eur. J. Inorg. Chem.* **2014**, *2014*, 742.

(49) Joya, K. S.; Subbaiyan, N. K.; D'Souza, F.; de Groot, H. J. M. *Angewandte Chemie-International Edition* **2012**, *51*, 9601.

(50) deKrafft, K. E.; Wang, C.; Xie, Z. G.; Su, X.; Hinds, B. J.; Lin, W. B. *Acs Applied Materials & Interfaces* **2012**, *4*, 608.

(51) Huang, J.; Blakemore, J. D.; Fazi, D.; Kokhan, O.; Schley, N. D.; Crabtree, R. H.; Brudvig, G. W.; Tiede, D. M. *PCCP* **2014**, *16*, 1814.

(52) Blakemore, J. D.; Mara, M. W.; Kushner-Lenhoff, M. N.; Schley, N. D.; Konezny, S. J.; Rivalta, I.; Negre, C. F. A.; Snoeberger, R. C.; Kokhan, O.; Huang, J.; Stickrath, A.; Tran, L. A.; Parr, M. L.; Chen, L. X.; Tiede, D. M.; Batista, V. S.; Crabtree, R. H.; Brudvig, G. W. *Inorg. Chem.* **2013**, *52*, 1860.

(53) Blakemore, J. D.; Schley, N. D.; Olack, G. W.; Incarvito, C. D.; Brudvig, G. W.; Crabtree, R. H. *Chem. Sci.* **2011**, *2*, 94.

(54) Venturini, A. B., A.; Reek, J. N. H.; Hetterscheid, D. G. H. *Chemistry - A European Journal* **2014**, *chem.201303796*.

(55) Zhou, M.; Balcells, D.; Parent, A. R.; Crabtree, R. H.; Eisenstein, O. *Acs Catal* **2012**, *2*, 208.

(56) Hintermair, U.; Sheehan, S. W.; Parent, A. R.; Ess, D. H.; Richens, D. T.; Vaccaro, P. H.; Brudvig, G. W.; Crabtree, R. H. *J. Am. Chem. Soc.* **2013**, *135*, 10837.

(57) Hong, D. C.; Murakami, M.; Yamada, Y.; Fukuzumi, S. *Energ Environ Sci* **2012**, *5*, 5708.

(58) Grotjahn, D. B.; Brown, D. B.; Martin, J. K.; Marelius, D. C.; Abadjian, M. C.; Tran, H. N.; Kalyuzhny, G.; Vecchio, K. S.; Specht, Z. G.; Cortes-Llamas, S. A.; Miranda-Soto, V.; van Niekerk, C.; Moore, C. E.; Rheingold, A. L. *J. Am. Chem. Soc.* **2011**, *133*, 19024.

(59) Diaz-Morales, O.; Calle-Vallejo, F.; de Munck, C.; Koper, M. T. M. *Chemical Science* **2013**, *4*, 2334.

(60) Lai, S. C. S.; Kleyn, S. E. F.; Rosca, V.; Koper, M. T. M. *The Journal of Physical Chemistry C* **2008**, *112*, 19080.

(61) Gao, P.; Gosztola, D.; Leung, L. W. H.; Weaver, M. J. *J. Electroanal. Chem.* **1987**, *233*, 211.

(62) Wonders, A. H.; Housmans, T. H. M.; Rosca, V.; Koper, M. T. M. *J Appl Electrochem* **2006**, *36*, 1215.

(63) Duca, M.; van der Klugt, B.; Koper, M. T. M. *Electrochim. Acta* **2012**, *68*, 32.

(64) Feng, Y.; Jiang, B.; Boyle, P. A.; Ison, E. A. *Organometallics* **2010**, *29*, 2857.

(65) Borkowska, Z.; Slimming, U. *Journal of Electroanalytical Chemistry and Interfacial Electrochemistry* **1991**, *312*, 237.

(66) Clavilier, J.; Van Huong, C. N. *Journal of Electroanalytical Chemistry and Interfacial Electrochemistry* **1977**, *80*, 101.

(67) Silva, F.; Martins, A. *J. Electroanal. Chem.* **1999**, *467*, 335.

(68) Angerstein-Kozlowska, H.; Conway, B. E.; Hamelin, A.; Stoicoviciu, L. *Electrochim. Acta* **1986**, *31*, 1051.

(69) Dima, G. E.; de Vooys, A. C. A.; Koper, M. T. M. *J. Electroanal. Chem.* **2003**, *554–555*, 15.

(70) Nakagawa, T.; Beasley, C. A.; Murray, R. W. *J. Phys. Chem. C* **2009**, *113*, 12958.

(71) Limburg, B.; Bouwman, E.; Bonnet, S. *Coord. Chem. Rev.* **2012**, *256*, 1451.

(72) Koper, M. T. M. *Chemical Science* **2013**, *4*, 2710.

(73) Lokshin, B. V.; Aleksanian, V. T.; Rusach, E. B. *J. Organomet. Chem.* **1975**, *86*, 253.

(74) Musić, S.; Popović, S.; Maljković, M.; Skoko, Z.; Furić, K.; Gajović, A. *Mater. Lett.* **2003**, *57*, 4509.

(75) Thanawala, S.; Georgiev, D. G.; Baird, R. J.; Auner, G. *Thin Solid Films* **2007**, *515*, 7059.

Chapter 4

Guidelines for the rational design of nickel – based double hydroxide electrocatalysts for the oxygen evolution reaction

ABSTRACT

The oxygen evolution reaction (OER) is one of the major bottlenecks hindering the implementation of a global economy based on solar fuels. The current limitations may only be overcome with cost-effective, active and stable electrocatalysts. It is known that Ni-based catalysts exhibit remarkable catalytic activities for the OER in alkaline media. In this joint theoretical-experimental study, we provide a thorough characterization of Ni-based double hydroxides with Cr, Mn, Fe, Co, Cu and Zn at the atomic scale that not only explains the reasons for their high activity but also provides simple design principles for the enhancement of their electrocatalytic properties. Our approach, based on the local symmetry and composition of the active sites, helps rationalize the effect of dopants on the catalytic activity of $Ni(OH)_2$ and, particularly, gives insights of the different roles of iron, chromium and manganese in the superior catalytic activity of NiFe, NiCr and NiMn double hydroxides, which reduce the OER potential to reach 0.5 mA cm^{-2} by 230 mV, 190 mV and 160 mV compared to IrO_2 nanoparticles, the state-of-the-art benchmarking catalysts, with 90% Faradaic efficiency for O_2 generation.

The content of this chapter has been published in: Diaz-Morales, O.; Ledezma-Yanez, I.; Koper, M.T.M. and Calle-Vallejo, F. *ACS Catalysis* **2015**, 5, 5380-5387

4.1. Introduction

Fossil fuels have played a central role in the development of society since the beginning of the industrial revolution in the 18th century, powering factories and related technologies and transportation networks that drive and sustain modern civilization. However, the world population has tremendously increased since then, with the concomitant increase in energy needs.[1] This has turned the availability of fossil fuels into an issue for future generations. Besides, combustion of fossil fuels is environmentally harmful and is responsible for serious public health problems related to the reduction of air quality.[1-3] Furthermore, recent studies suggest that the increase of the global average temperature should not exceed 2 °C, which may only be achieved by drastic reductions of CO_2 emissions associated to burning coal, oil and natural gas, added to the widespread use of alternative sources of energy.[4] Among those, sunlight is by far the largest exploitable resource.[5] The transformation of solar energy into chemical energy is promising,[3,5-7] as the electrons generated by (photo)-electrochemical oxygen evolution can be used to drive, for instance, the electrochemical reduction of protons or carbon dioxide into fuels. An additional benefit of such process is that water and oxygen are the main byproducts.

Nevertheless, one of the major bottlenecks hampering the application of solar power as a widespread energy source is the slow kinetics of oxygen evolution reaction (OER). The overpotential of this reaction reduces significantly the overall efficiency of energy conversion.[8,9] Numerous catalysts have been studied to accelerate the water oxidation reaction but the most active compounds are based on scarce, hence expensive compounds such as IrO_2 or RuO_2.[10-12] Alternatively, catalysts based on earth-abundant transition metals have been proposed, showing comparable and even higher intrinsic activity towards OER in alkaline media than the iridium or ruthenium-based catalysts.[9,12-17] Those catalysts are mainly based on nickel or cobalt oxides, the activity of which has been rationalized through DFT calculations.[14,18]

Materials based on nickel hydroxide have also been studied, displaying good catalytic activity for oxygen evolution in alkaline media.[13,15,17,19-21] It has been reported that the catalytic activity of nickel hydroxide can be significantly enhanced by modifying it with

other transition metals like chromium or iron,[13,20-22] and the intrinsic catalytic activity of NiFe double hydroxides (from here on DHs) towards oxygen evolution in alkaline media has been shown to be considerably higher than that of iridium-based catalysts.[15,17,23,24] However, there are no systematic attempts to understand the correlation between the activity of nickel-based double hydroxides towards water oxidation and the nature of the added transition metals. Furthermore, comparison between different literature reports on the experimental activity of DHs is not straightforward due to the differences in the way of benchmarking the catalytic activity.[15,21]

We present here a theoretical and experimental study of the electrocatalytic properties of nickel-based double hydroxides with 3d transition metals for the OER in alkaline media. This work gives a systematic study of the effect of transition-metal doping on the activity of nickel-based catalysts. The joint analysis of theoretical and experimental results is generally more accurate and insightful when multiple materials are compared,[18,25] which is why we have established some theoretical trends in catalytic activity for a given family of compounds, synthesized all of them by means of the same method and measured their experimental activities in identical conditions. The trends are rationalized in terms of the local symmetry and composition of the active sites, and aim at providing simple and general design rules in OER electrocatalysis.

4.2. Computational and Experimental Details

4.2.1. DFT calculations

The DFT calculations were performed with the Vienna ab initio simulation package,[26] using the RPBE exchange-correlation functional[27] and ultrasoft pseudopotentials.[28] Such functional and pseudopotentials allow for straightforward comparisons with previous works.[18] The simulations were made with 4-layer slabs: the two top layers were free to move in all directions, while the two bottom layers were fixed at the ground-state bulk distances. The relaxations were carried out with the quasi-Newton scheme for the using as convergence criterion a maximum residual force on any atom of 0.05 eV $Å^{-1}$. In the low-coverage calculations the adsorbates were free to move in all directions, while in certain

high-coverage calculations the x or y directions were constrained. The simulated 2×2 (001) monoxide slabs with a $4 \times 4 \times 1$ k-point mesh and a plane-wave cutoff of 450 eV ensured convergence of the adsorption energies within 0.05 eV. The monoxides were simulated in the rock salt structure. We added 15 Å of vacuum between periodically repeated images and applied dipole corrections. The Methfessel-Paxton method was used to smear the Fermi level[29] with $k_BT = 0.1$ eV, and all energies were extrapolated to 0 K. The gas-phase molecules (H_2, H_2O) were calculated in boxes of 15 Å × 15 Å × 15 Å, $k_BT = 0.001$ eV and a $1 \times 1 \times 1$ k-point mesh. The free energies are approximated as follows: $G = E_{DFT} + ZPE - TS$, where E_{DFT} and ZPE are the total and zero-point electronic energies calculated through DFT, and TS are entropic contributions (only taken into account for gas-phase species). The ZPEs in eV for H_2, H_2O, *O, *OH and *OOH are, respectively, 0.27, 0.56, 0.07, 0.34 and 0.40. The TS corrections in eV for H_2 and $H_2O_{(l)}$ are 0.40 and 0.67 eV,[30,31] respectively. In order to describe the energetics of solvated protons and electrons and to estimate overpotentials we used the computational hydrogen electrode.[31] The procedure for estimating the free energies of adsorption of *O, *OH and *OOH, which are the considered oxygen evolution intermediates, a brief discussion on solvation and the details of the construction of the volcano plots are given in Appendix C and have also been given elsewhere.[18,30] The active sites on the (001) facet are illustrated in Figure 1. The (001) surfaces of the monoxides (MO with M = Ca to Cu) were initially simulated (Figure 1a). Furthermore, the surface layer of a NiO substrate was partially hydrogenated and doped with Cr, Mn, Fe, Co, Ni, Cu and Zn (Figure 1b), so as to model oxyhydroxide (NiMOOH) sites. To date, there are no clear conclusions in the literature about the actual surface morphology of Ni (oxy)hydroxides with and without Fe doping. This holds for theoretical as well as experimental studies. In fact, various authors have claimed that under reaction conditions, different oxyhydroxide phases compose the exposed surfaces. For instance, Bell and coworkers[24] claim that Fe doping enhances the activity of the (0 1 -1 2) plane of γ-NiOOH, while Li and Selloni[32] attribute the activity to the (0 1 -1 5) plane of β-NiOOH.

In any case, the EXAFS experiments of Bell and coworkers[24] reveal valuable information: both metals in NiFeOOH form octahedral complexes of the type NiO_6 and FeO_6. This is the reason why we have used bulk nickel monoxide (NiO) to build our

surfaces, as it contains octahedral metal centers surrounded by six oxygen ligands (NiO_6). Moreover, we have hydrated one of the surface oxygen atoms and doped with Cr, Mn, Fe, Co, Ni, Cu and Zn (Figure 1b) so that the composition of the top layer of a 2×2 unit cell is NiMOOH. In that way, we can reproduce in our model the only two certain experimental observations of Ni oxides under OER conditions: i) the surface is partially dehydrated, so that hydroxides turn into oxyhydroxides. ii) The metal centers form MO_6 and NiO_6 complexes. In broad terms, the use of hydrogenated NiO is as arbitrary as the use of γ-NiOOH or β-NiOOH until further conclusive experimental evidence is obtained. This choice ensures, therefore, that the local symmetry of the catalyst is reproduced, in spite of the lack of precise information on the catalyst's surface morphology. The OER activity of these sites was modeled at a high coverage of oxygenated species (see Figure 1c and full details in Appendix C, Figure C7) and all calculations were spin-unrestricted. For each system, ferromagnetic and antiferromagnetic calculations (with spin alignment planes on the (111) and (100) planes) were carried out. Note that MnO, FeO, CoO and NiO are antiferromagnetic oxides. Particularly, NiO has spin alignment in the (111) plane.[24]

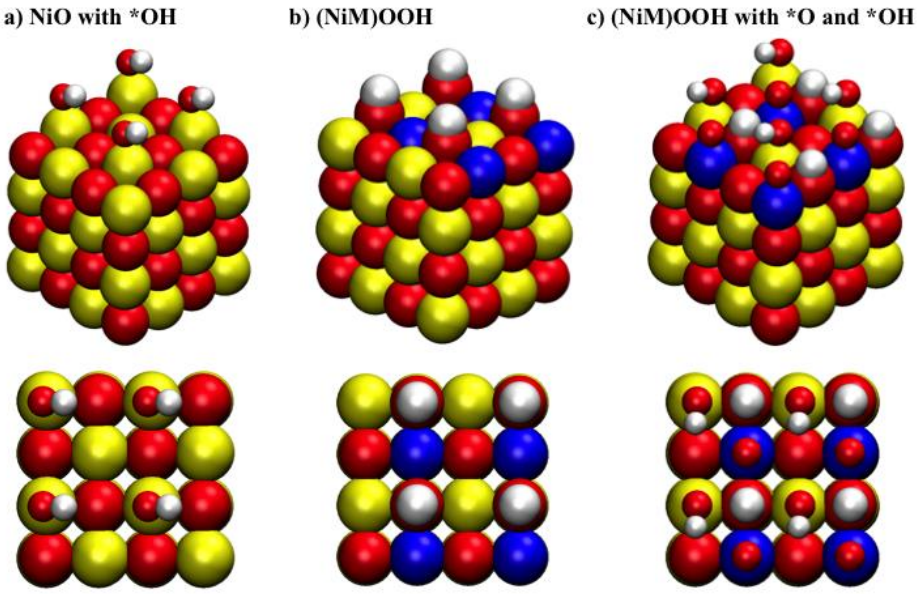

Figure 1. Perspective and top views of the active sites at (001) surface facets of the oxides under study. In this surface facet, octahedral NiO_6 and MO_6 complexes are formed. Ni atoms appear in yellow, oxygen atoms in red, M atoms in blue, where M can be Cr, Mn, Fe, Co, Ni, Cu and Zn; and H atoms in white. For convenience, O and H atoms in the lattice (large) and adsorbed (small) have been drawn with different radii. a) NiO with *OH adsorbed on Ni. b) Clean NiMOOH. This structure contains 50% M in the top layer and one of the oxygen atoms has been hydrogenated. c) The same as in b) with *O on M and *OH on Ni, corresponding to the active sites under OER conditions.

4.2.2. Chemicals

The following reagents were utilized: $Ni(NO_3)_2{\cdot}6H_2O$ (Sigma-Aldrich, purum p.a., crystallized, ≥97.0% (KT)), $Cr(NO_3)_3{\cdot}9H_2O$ (Sigma-Aldrich, puriss. p.a., ≥98.0%), $Mn(NO_3)_2{\cdot}xH_2O$ (Alfa Aesar, metal basis, ≥97.0%), $CoCl_2{\cdot}6H_2O$ (Sigma-Aldrich, purum p.a., crystallized, ≥98.0% (KT)), $Fe(NO_3)_3{\cdot}9H_2O$ (Sigma-Aldrich, ACS reagent, ≥98%), $Cu(NO_3)_2{\cdot}3H_2O$ (Sigma-Aldrich, purum p.a., 98.0-103% (KT)), $Zn(NO_3)_2{\cdot}6H_2O$ (Sigma-Aldrich, reagent grade, 980%), $Na_2CO_3{\cdot}10H_2O$ (Merck, pro analysis), KOH (Sigma-Aldrich, semiconductor grade, pellets, 99.99% trace metals basis), EtOH (Sigma-Aldrich,

puriss. p.a., absolute, ≥99.8% (GC)). Nafion® (Sigma-Aldrich, 5 wt. % in lower aliphatic alcohols and 15-20% water). All chemicals were used as received, unless otherwise stated. The water used in all experiments was deionized and ultrafiltrated by a Millipore Milli-Q system (resistivity > 18.2 MΩ cm and TOC < 5ppb).

4.2.3. Cleaning procedure

The glassware was thoroughly cleaned before the experiments by boiling in a 1:3 mixture of concentrated HNO_3/concentrated H_2SO_4 to remove organic contaminations. After this initial treatment, the glassware was boiled five times in water. When not in use, it was stored in an aqueous solution of 0.5 M H_2SO_4 and 1 g/L $KMnO_4$. To remove the permanganate, the glassware was rinsed thoroughly with water and then immersed in a solution 1:1 of concentrated H_2SO_4 and 30% H_2O_2 to remove all particles of MnO_2. Afterwards, it was rinsed with water again and boiled five times in water.

4.2.4. Synthesis of the Nickel Double Hydroxides

All double hydroxides (DH) were prepared by the co-precipitation route[33], using 0.1 M solutions of $Ni(NO_3)_2$ and $M(NO_3)_n$ (M^{n+}= Cr^{3+}, Mn^{2+}, Fe^{3+}, Co^{2+}, Cu^{2+}, Zn^{2+}) as precursors. The precipitation was performed at 80 °C by dropping 32 mL of the solution with the metals in 1:1 molar ratio over 10 mL of water previously adjusted to pH 9 with 0.1 M Na_2CO_3. The pH was kept approximately constant at 9 during the synthesis by simultaneous dropping of 0.1 M Na_2CO_3 (36 mL). The addition of the Ni^{2+}/M^{n+} solution and the Na_2CO_3 was completed within 1.5 h, after which the suspension was glass-filtered and thoroughly rinsed with water. The powders were subsequently dried overnight at 120 °C and fine-ground.

Nickel(II) hydroxide was prepared by dropping 15 mL of NaOH 2M over 50 mL of $Ni(NO_3)_2$ 0.1 M. The suspension was glass-filtered and thoroughly rinsed with water. The powders were subsequently dried overnight at 120 °C and fine-ground.

4.2.5. Characterization

Powder X-Ray diffraction (XRD) measurements were performed in a Philips X'Pert diffractometer, equipped with the X'Celerator, using Cu-Kα radiation. The collection was done in the range $10° < 2\theta < 100°$ in steps of 0.020° (2θ) with counting time 10 s / step.

Fourier-transformed Infrared (FTIR) measurements were performed using an IRAffinity-1S FTIR spectrophotometer from Shimadzu. The machine is equipped with a high-energy ceramic light source, a temperature-controlled, high-sensitivity DLATGS detector, with a Michelson interferometer (30º incident angle) and a spectral resolution of 0.6 cm^{-1}.

Electrochemical measurements were carried out in a three-electrode, two-compartment cell with the reference electrode separated by a Luggin capillary. The working electrode over which the catalyst was supported was an Au rotating disk electrode (RDE) with a diameter of 4.6 mm, and all experiments were performed at 1500 RPM. The counter electrode was a gold spiral and a reversible hydrogen electrode (RHE) was used as reference electrode. Unless stated, all potentials in this work are referred to RHE scale. A platinum wire was connected to the reference electrode through a capacitor of 10 μF, acting as a low-pass filter to reduce the noise in the low current measurements. Electrochemical measurements were performed with a potentiostat PGSTAT12 (Metrohm - Autolab). Before and between measurements, the RDE electrode was first polished with 0.3 μm and 0.05 μm alumina paste (Buehler Limited). Subsequently, the electrode was ultrasonicated for 5 minutes in water to remove alumina particles. The OER measurements were conducted with cyclic voltammetry at 0.01 V s^{-1} in solutions saturated with Ar, bubbled at least 30 min prior to the electrochemical experiments.

The double hydroxides were immobilized on the electrode by drop-casting inks, using Nafion® as binder agent. We used Na-exchanged Nafion to avoid possible corrosion of the hydroxides due to the strong acidity of the commercially available solution. Alkaline Nafion was prepared according to the procedure reported in the literature,[34] by mixing 2 parts in volume of commercially available 5 wt.% Nafion solution with 1 part of 0.1 M

NaOH, which is reported to have ~ pH 11. The preparation of the inks is similar to previously reported methods to immobilize OER catalysts for RDE experiments,[35,36] with concentrations of 5 mg_{DH} mL_{ink}^{-1} and 1 mg_{Nafion} mL_{ink}^{-1}. The inks were prepared in absolute ethanol, first dispersing the DH within the solvent by sonication for 30 min, subsequently adding the Na-exchanged Nafion, followed by 20 min of further sonication. The catalysts were drop-casted on the Au disk to give a final loading of 75 μg_{DH} cm^{-2}_{disk} and dried in vacuum, where cm^2_{disk} accounts for the geometrical surface area of the disk.

The catalytic activity is reported as current density in mA cm_{oxide}^{-2}, where cm_{oxide}^{2} is the real surface area of the films, calculated from pseudo-capacitance measurements[12,37] in the potential region 0.9 – 1.0 V vs. RHE; the specific capacitance used for this measurement was 60 $\mu F \cdot cm^{-2}$.[37]

4.3. Results and Discussion

The advantageous catalytic[38] and electrocatalytic[10] properties of nickel-containing oxides are well documented. Particularly, recent theoretical studies[18,24,32,39] have shown the high activity of nickel-containing oxides for the OER. In those studies, NiO has been reported to have an activity close to optimal in Sabatier-type analyses. To confirm this observation, in Figure 2 we provide the calculated activities for the entire range of oxides between CaO and CuO. The descriptor used in the figure is the difference between the adsorption energies of *O and *OH, which is advantageous because it tunes simultaneously two adsorption energies (through their difference), instead of only one. Note that the existence of scaling relationships between *O, *OH and *OOH implies proportional variations of their differences.[40] Another advantage of this descriptor is that the points in the right leg of the volcano plot do not show scattering,[18] as evidenced in Figures 2 and 3. Alternatively, parameters different from adsorption energies have been used to describe activity trends on oxides, for instance bulk energetics,[41] and recent work has shown the correspondence between these parameters and adsorption energies.[39]

The trends in Figure 2 follow a volcano-shaped curve with the lowest overpotential corresponding to NiO. Additionally, MnO, CoO, FeO, and CuO are predicted to show fairly

high activities. However, it is not certain whether the active sites of these oxides under OER conditions correspond to those of the pristine oxide. For instance, the presence of oxyhydroxide phases at the potential and pH ranges of interest for the OER has been reported on Co, Ni and Au oxides.[32,42-44]

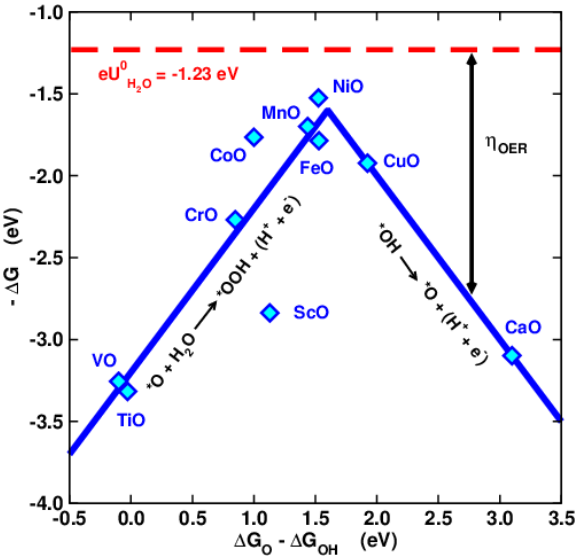

Figure 2. Sabatier-type volcano plot for the pristine (001) surfaces of the monoxides (see Figure 1a) in the range between CaO and CuO. The descriptor in the x-axis is the difference between the adsorption energies of oxygen and hydroxyl. The vertical differences between the red line and the blue lines and points provide an estimation of the oxygen evolution overpotential on the oxides. The potential-limiting steps are provided in black: the left leg of the volcano (strong binding side) is limited by the transformation of *O into *OOH, while the right leg (weak binding side) is limited by the transformation of *OH into *O (following ref.[18]).

Consequently, these observations set up an appropriate background to pose two important questions: first, is the pristine (001) surface with low-adsorbate coverage a good representation of NiO during the OER. Second, why is it possible to improve the activity of NiO by doping/mixing with other oxides, if NiO is already expected to be the most active monoxide? In the following we will address these questions both theoretically and experimentally and show that the answers are intimately related.

The descriptor in the x-axis in Figure 2, that is the difference between the adsorption energies of *O and *OH, marks the top of the activity plot at approximately 1.6 eV. Pristine NiO has a difference of ~1.5 eV, whence its low predicted overpotential. When the NiO surface is further oxidized and hydrated to produce active sites of the NiOOH type, the formal oxidation state of Ni changes from +2 to +3. This is reflected in a considerable weakening of the adsorption energies, so that the descriptor is ~1.84 eV for NiOOH. Note that similar decreases in binding strength have been reported for transition-metal oxides, including those of Ni, as the metal center is oxidized.[40] Hence, the value of the descriptor for pristine NiO is 0.1 eV more negative than required to be at the top of the volcano, whereas the value for the oxyhydroxide is 0.24 eV more positive than optimal. This difference of 0.24 eV from thermodynamic optimality suggests that significant improvements can be made to NiOOH-like active sites in terms of binding to OER intermediates. The design principle in this case is simple: NiOOH needs to be modified so that the difference in the adsorption energies of *O and *OH is decreased by approximately 0.24 eV.

We used this design criterion to assess the OER activity of NiMOOH sites with octahedral symmetry, with M = Cr, Mn, Fe, Co, Cu, and Zn. The results are shown in Figure 3, where NiOOH, NiO (from Figure 2) and IrO_2 (adapted from ref.[18]) are included for the sake of comparison. The figure includes the effect of doping on Ni sites and also the effect of the NiO lattice on the M sites. Figure 3a shows that the doping effects on Ni are modest, and slight increases on the OER overpotential with respect to NiOOH are observed for Mn, Fe, Co, Cu and Zn doping, while Cr doping decreases the overpotential. Thus, taking into account the accuracy of DFT at the GGA level, that is 0.2 eV,[45] it is possible to say that the predicted overpotentials of Ni sites in NiMOOH are similar to that of NiOOH, with only Cr doping reducing the overpotential, but the small differences make it hard to provide more detailed predictions. Note that although NiO is usually antiferromagnetic with spin alignment in the (111) plane,[24] the addition of dopants results in ferrimagnetic configurations and, in some cases, the spin alignments switch to the (100) plane. Therefore, the spin state of the surface is important for the determination of the trends.

On the other hand, the effects of the NiO lattice on the M sites are rather different, depending on the transition metals. Basically, there are two kinds of dopants in the studied group of transition metals: first, Mn and Fe, which possess nearly optimal binding energies and hence reduce the predicted OER overpotential; second, Cr, Co, Cu and Zn, which increase the OER overpotential.

In summary, the addition of Cr, Mn and Fe should enhance the OER activity of NiOOH, while Co, Cu and Zn will have similar or larger overpotentials than NiOOH.

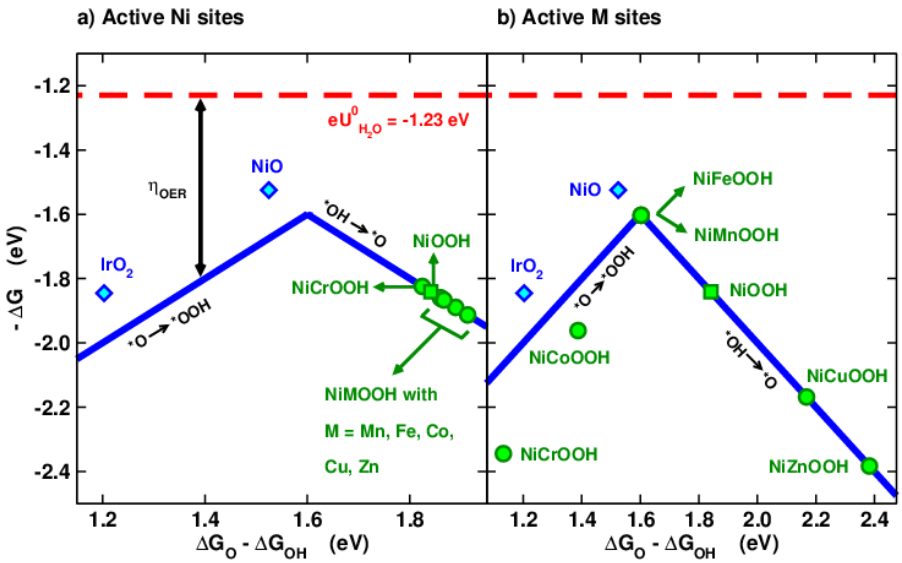

Figure 3. Sabatier-type volcano plots for Ni-based oxyhydroxide sites doped with transition metals (see Figures 1b and 1c). The surfaces were doped with Cr, Mn, Fe, Co, Cu, and Zn. The descriptors and catalytic activities were calculated analogously to those in Figure 2. The vertical differences between the red line and the blue lines and/or the points provide an estimation of the oxygen evolution overpotential on the oxides (η_{OER}). a) Effect of doping on Ni sites. It is observed that doping with Mn, Fe, Co, Cu and Zn causes slight increases in the OER overpotential of Ni sites, while Cr causes a slight decrease. b) Activity of dopants in a NiOOH lattice. The overpotentials are rather different depending on the transition metal and Fe and Mn are near the top of the volcano. Pristine NiO (from Figure 2) and IrO_2 (adapted from ref.[18]) are provided for comparison as blue rhombs, while NiOOH appears as a green square.

The noteworthy enhancing effect of Fe on the catalytic activity of nickel hydroxide has been reported in the literature,[13,20,21] although the explanation for such enhancement is still a matter of debate.[13,24,32,46] Although the ligand effect is well known in metal electrocatalysis and has been systematically quantified and exploited,[47,48] the effect of doping in oxide electrocatalysis is less well documented, as its magnitude and direction depends on the interactions between the host and the guest metals in a stretched lattice, in addition to the interactions of the metals and lattice oxygen.[49,50] In our particular case, we observe that the ligand effect is small on Ni sites (Figure 3a), while it is significant on M sites (Figure 3b). This is intuitive, as M is embedded in a lattice where the M-O distances are different from its pure oxide. Furthermore, our results are in agreement with those of Bell and coworkers,[24] who concluded that the metal site responsible for the significant enhancement of the catalytic activity of NiFeOOH compared to NiOOH is Fe, rather than Ni. We predict the same for NiMnOOH, in which Mn will be the active metal. Conversely, in NiCrOOH, which is the other surface that may reduce the OER overpotential, Ni is the active site, rather than Cr, and the enhancement effect should be lower than that of Fe, based on Figure 3a.

It is also important to note that the active sites in Figure 1c possess full coverage of oxygenated species during the OER. Coverage effects are sometimes important, as lateral adsorbate-adsorbate interactions may weaken or strengthen the adsorption energies.[51] The adsorbates covering the surface can be inferred from volcano plots, considering that a) NiOOH is on the weak side of the volcano in Figure 3, so its potential-limiting step is the transformation of *OH into *O, and the Ni sites should be covered with *OH under OER conditions. The situation is analogous for NiCuOOH and NiZnOOH. b) The potential-limiting step for Cr, Mn, Fe and Co monoxides is the transformation of *O into *OOH. Thus, these M sites at NiMOOH surfaces will normally be covered with *O under OER conditions.

Experimentally, one can start assessing the effect of transition metals on NiO-based catalysts by analogy to well-defined mixed oxides. In this vein, Landon *et al.* have proposed that $NiFe_2O_4$ spinel has a significant role in the enhancement of the catalytic

activity of mixed NiFe oxides.[46] The findings of Li and Selloni controvert this statement, as they found through DFT calculations that $NiFe_2O_4$ is active for the OER, but its activity is noticeably lower than that of Fe-doped Ni oxides.[32] To evaluate these conflicting claims, we induced the thermal decomposition of the NiFe DH so as to obtain the spinel structure, as shown in the XRD pattern in Figure C1 in Appendix C, and measured its catalytic activity towards electrochemical water oxidation. The results are summarized in Figure 4, where it is observed that the onset of the reaction on $NiFe_2O_4$ is located at more positive potentials compared to NiFe DH. We conclude, therefore, that the spinel phase is indeed less active than the double hydroxide and that the active sites in both catalysts must be different.

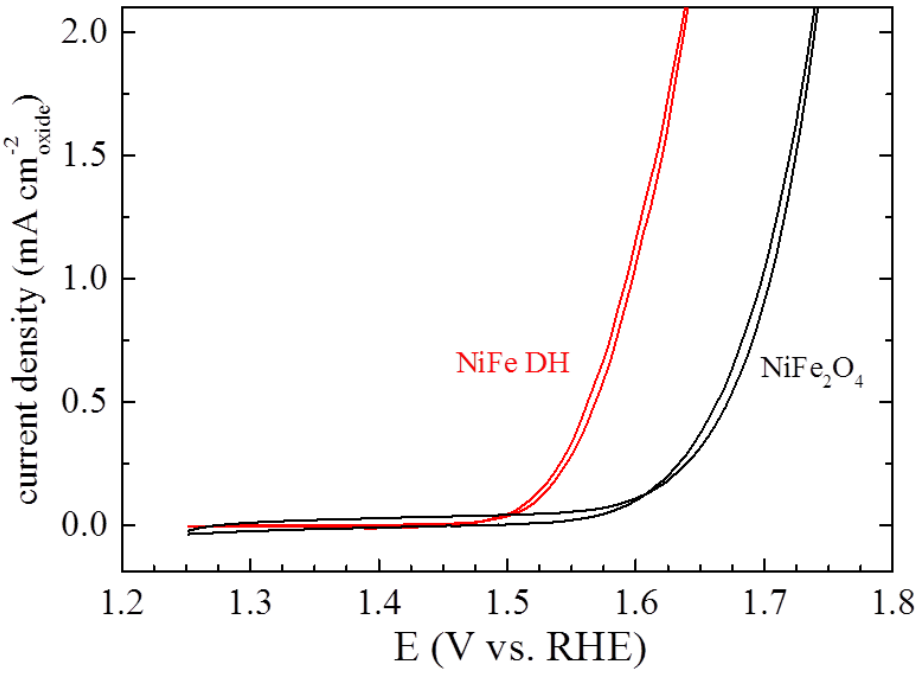

Figure 4. Cyclic voltammetry for the oxygen evolution reaction in 0.1 M KOH of NiFe DH and $NiFe_2O_4$ immobilized on Au. Experiments were performed under hydrodynamic conditions (rotation rate: 1500 RPM, scan rate: 0.01 V s^{-1}). The solid line shows the catalytic activity measured on the NiFe DH and the dashed line shows the activity measured on the $NiFe_2O_4$, obtained after thermal decomposition of the NiFe DH.

The effect of Fe doping on the catalytic activity of NiFe DH was studied for Fe contents in the range 25-75 % (see Figure C3 in Appendix C). We observed that the highest catalytic activity is reached at 50% of Fe doping, so this composition was used to study the doping effects of the other transition metals both experimentally and computationally.

With the theoretical results of Figure 3 in mind, we conducted OER experiments on NiOOH doped with 50% Cr, Mn, Fe, Co, Cu and Zn and on $Ni(OH)_2$, to be used as benchmark. Figure 5 shows the polarization curves obtained for the oxygen evolution on the different catalysts. There is a clear effect of the 3d transition metals in the catalytic activity towards oxygen evolution, measured in terms of current density; in the case of Mn, Cr and Fe, the OER potential to reach 0.5 mA cm^{-2} is reduced by approximately 60, 100 and 130 mV, respectively, compared to $Ni(OH)_2$. On the contrary, Co, Cu and Zn DH's increase the overpotential. Interestingly, NiMn DH is predicted by our theoretical analysis to be as active as NiFe DH. Note, however, that the XRD patterns of the Mn DH (see Figure C2 in Appendix C) suggest that the synthesis method produced a separate phase of $MnCO_3$ and a minor amount of the double hydroxide, which was also confirmed by FTIR measurements (see Figure C4 in Appendix C). Segregation of $MnCO_3$ during the synthesis process may explain the lower than expected catalytic activity observed for the NiMn DH due to a high amount of amorphous sites in the external layers of the hydroxide structure, which are the most catalytically active. It is worth mentioning that the synthesis of the NiCr, NiMn and NiFe was also tried using NaOH as precipitating agent instead of Na_2CO_3 to check the effect of carbonate anion in the catalytic activity of the double hydroxides. Figure C5 in Appendix C shows the polarization curves for OER on the three nickel-based double hydroxide precipitated with sodium hydroxide and sodium carbonate, and it is clear that the catalysts precipitated from Na_2CO_3 have higher OER activity than their counterpart precipitated from NaOH.

Note in passing that in the case of Co-doping, it is observed that $Ni(OH)_2$ segregates from the mixed hydroxide (see Figure C2 in Appendix C). This, however, has no influence in our conclusions, as NiCoOOH is not predicted theoretically to have lower overpotentials than NiOOH.

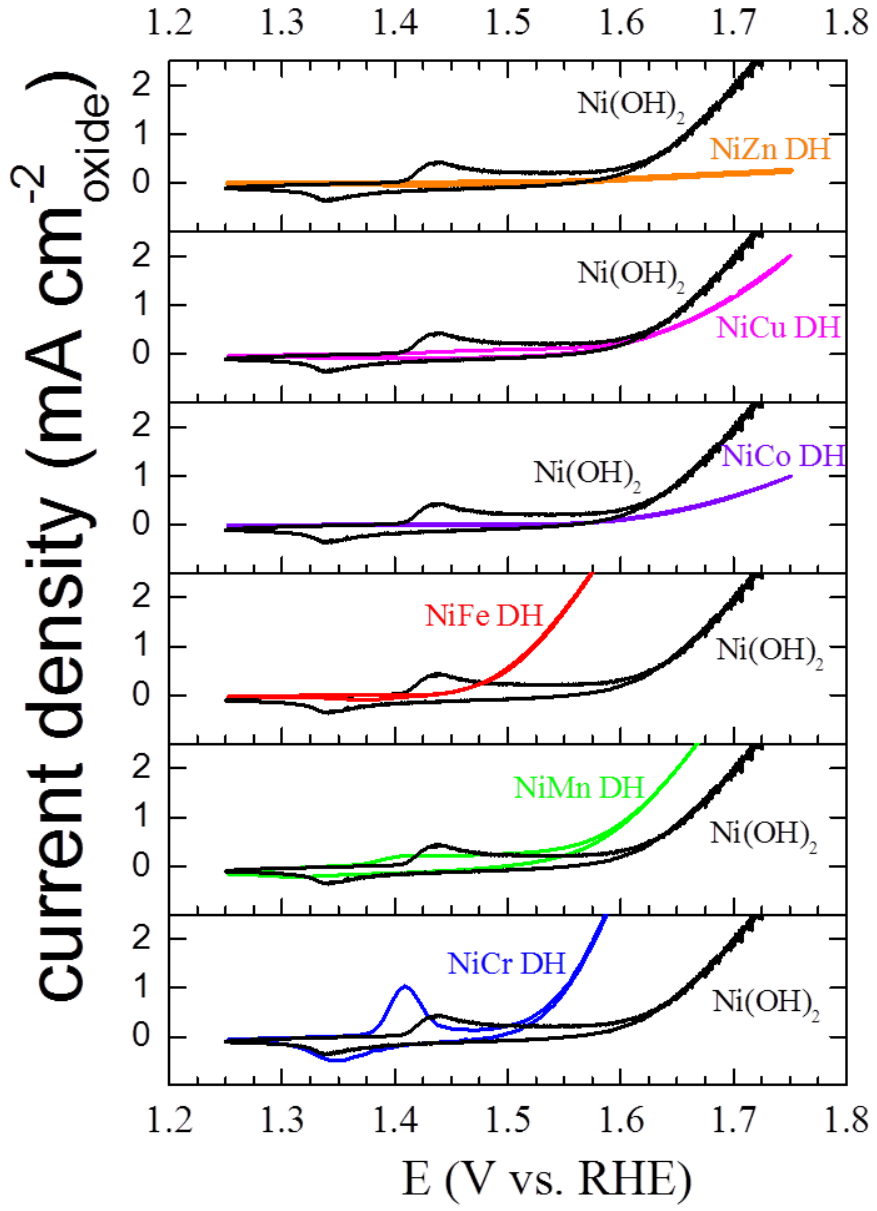

Figure 5. Cyclic voltammetry for the OER in 0.1 M KOH of nickel-based DH immobilized on Au. Experiments were performed under hydrodynamic conditions (rotation rate: 1500 RPM, scan rate: 0.01 V s^{-1}). The solid line shows the activity measured on the DH's and the dashed line shows the activity $Ni(OH)_2$, presented as benchmark of the catalytic activity.

The catalytic activity of the NiFe DH towards electrochemical oxygen evolution in alkaline media was also compared with that of IrO_2, which is normally used as benchmark for this reaction.[12] The double hydroxide possesses higher catalytic activity than the benchmark (see Figure C6 Appendix C) and the activity is comparable to the one reported for NiFe DH supported on carbon nanotubes.[15,22] Importantly, the preparation procedure used in this work is much simpler and can be applied to the elaboration of several other double hydroxides. Such a method might prove advantageous for the large-scale production of catalysts. Moreover, the procedure shows that the enhanced activity of NiFe double hydroxides is mostly due to sites composed of Ni, Fe/Cr and oxygenated species distributed spatially in an octahedral fashion.

We have also estimated the faradaic efficiency towards electrochemical water oxidation catalyzed by NiFe DH by rotating ring-disk electrode (RRDE) measurements.[12] Figure 6 shows that the NiFe catalyst splits water with a faradaic efficiency of >90% at 270 mV of overpotential (see the SI for details about the calculation of the efficiency).

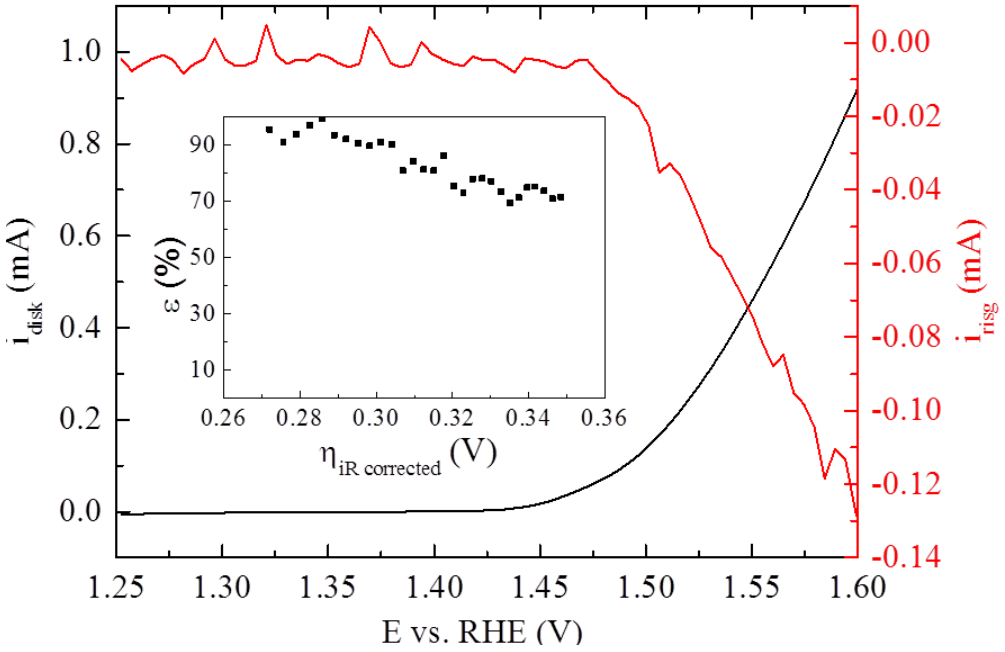

Figure 6. Polarization curve for OER in 0.1 M KOH of nickel-based DH immobilized on Au. Experiments were performed in RRDE configuration (Pt ring at 0.45 V vs. RHE) at 1500 RPM. Scan rate: 0.01 V s^{-1}. Inset: Faradaic efficiency (ε) as function of the potential applied to the disk.

Finally, we have also addressed the important matter of the catalyst stability and durability under working conditions. To do so, we used McCrory *et al.*'s method[12] (further details shown in Appendix C), and conclude that NiFe DHs are more stable than IrO_x nanoparticles, which are typically used as benchmarks.

4.4. Conclusions

We have presented simple guidelines for the rational design of Ni-based double hydroxides with transition metals, to catalyze the electrochemical water oxidation reaction. These rules allowed us to understand the improving effect of Cr, Mn and Fe on the catalytic activity of the Ni-based double hydroxides towards oxygen evolution and the deleterious

effect of Co, Cu and Zn. The active sites are suggested to be of the oxyhydroxide type (that is NiMOOH, where M is a transition-metal dopant), in which the metals form octahedral NiO_6 and MO_6 complexes. We have made one-to-one comparisons between $Ni(OH)_2$ and the double hydroxides, and between the double hydroxides and state-of-the-art IrO_2 nanoparticles. At a reference current density of 0.5 mA cm^{-2} we observed that, on the one hand, Mn, Cr and Fe reduce the potential needed to reach the reference current density by 60 mV, 100 mV and 130 mV with respect to $Ni(OH)_2$. On the other hand, the potential to reach the reference current density is reduced by 160, 190 and 230 mV, compared to IrO_2 nanoparticles, by doping with Mn, Cr and Fe, respectively. These two comparisons show that our simple preparation method renders catalysts that are substantially more active than those in the state of the art. According to the DFT-based analysis presented here, the effects Fe, Mn and Cr doping are different, as Fe and Mn are the active sites in NiFeOOH and NiMnOOH, and Ni is the active site in NiCrOOH.

The NiFe DHs prepared here show significantly higher catalytic activity and stability towards electrochemical water oxidation than IrO_2, with over 90% efficiency for electrochemical O_2 generation. Their activity is comparable to that of NiFe DHs obtained through different procedures, while using a considerably simple preparation method.

These conclusions must be seen in the light of the experimental uncertainty about the exact structure of the surfaces in combination with the accuracy of DFT. Therefore, the significance of this study lies mainly in the guidelines and broader understanding it provides in terms of trends in catalytic activity.

4.5. Acknowledgments

FCV acknowledges funding from the Netherlands Organization for Scientific Research (NWO), Veni project number 722.014.009. This work was also supported by the Netherlands Organization for Scientific Research (NWO) and in part by the BioSolar Cells open innovation consortium, supported by the Dutch Ministry of Economic Affairs, Agriculture and Innovation. The Stichting Nationale Computerfaciliteiten (NCF) is also acknowledged for the use of their supercomputer facilities, with financial support from

NWO. Dr. F. Calle-Vallejo is kindly acknowledged for his computational contributions to the project, and I. Ledezma-Yanez for the assistance with the FTIR characterization of the DHs samples. Prof. Dr. E. Bouwman is acknowledged for the use of the X-Ray Diffraction facility in her group at Leiden University and Dr. W. T. Fu for useful discussions on the XRD results.

REFERENCES

(1) Hoffert, M. I.; Caldeira, K.; Jain, A. K.; Haites, E. F.; Harvey, L. D. D.; Potter, S. D.; Schlesinger, M. E.; Schneider, S. H.; Watts, R. G.; Wigley, T. M. L.; Wuebbles, D. J. *Nature* **1998**, *395*, 881.

(2) Olah, G. A.; Prakash, G. K.; Goeppert, A. *J. Am. Chem. Soc.* **2011**, *133*, 12881.

(3) Crabtree, G. W.; Dresselhaus, M. S.; Buchanan, M. V. *Phys. Today* **2004**, *57*, 39.

(4) McGlade, C.; Ekins, P. *Nature* **2015**, *517*, 187.

(5) Lewis, N. S.; Nocera, D. G. *Proc. Natl. Acad. Sci. U. S. A.* **2006**, *103*, 15729.

(6) Bensaid, S.; Centi, G.; Garrone, E.; Perathoner, S.; Saracco, G. *ChemSusChem* **2012**, *5*, 500.

(7) Hermans, L. J. F. *Energy Survival Guide*; BetaText / Leiden University Press: Amsterdam, 2011.

(8) Koper, M. T. M. *J. Electroanal. Chem.* **2011**, *660*, 254.

(9) Dau, H.; Limberg, C.; Reier, T.; Risch, M.; Roggan, S.; Strasser, P. *ChemCatChem* **2010**, *2*, 724.

(10) Matsumoto, Y.; Sato, E. *Materials Chemistry and Physics* **1986**, *14*, 397.

(11) Lee, Y.; Suntivich, J.; May, K. J.; Perry, E. E.; Shao-Horn, Y. *J. Phys. Chem. Lett.* **2012**, *3*, 399.

(12) McCrory, C. C.; Jung, S.; Peters, J. C.; Jaramillo, T. F. *J. Am. Chem. Soc.* **2013**, *135*, 16977.

(13) Corrigan, D. A. *J. Electrochem. Soc.* **1987**, *134*, 377.

(14) Suntivich, J.; May, K. J.; Gasteiger, H. A.; Goodenough, J. B.; Shao-Horn, Y. *Science* **2011**, *334*, 1383.

(15) Gong, M.; Li, Y.; Wang, H.; Liang, Y.; Wu, J. Z.; Zhou, J.; Wang, J.; Regier, T.; Wei, F.; Dai, H. *J. Am. Chem. Soc.* **2013**, *135*, 8452.

(16) Grimaud, A.; May, K. J.; Carlton, C. E.; Lee, Y. L.; Risch, M.; Hong, W. T.; Zhou, J.; Shao-Horn, Y. *Nat. Commun.* **2013**, *4*.

(17) Song, F.; Hu, X. *Nat. Commun.* **2014**, *5*.

(18) Man, I. C.; Su, H.-Y.; Calle-Vallejo, F.; Hansen, H. A.; Martínez, J. I.; Inoglu, N. G.; Kitchin, J.; Jaramillo, T. F.; Nørskov, J. K.; Rossmeisl, J. *ChemCatChem* **2011**, *3*, 1159.

(19) Oliva, P.; Leonardi, J.; Laurent, J. F.; Delmas, C.; Braconnier, J. J.; Figlarz, M.; Fievet, F.; Guibert, A. d. *J. Power Sources* **1982**, *8*, 229.

(20) Młynarek, G.; Paszkiewicz, M.; Radniecka, A. *J. Appl. Electrochem.* **1984**, *14*, 145.

(21) Corrigan, D. A.; Bendert, R. M. *J. Electrochem. Soc.* **1989**, *136*, 723.

(22) Gong, M.; Dai, H. *Nano Res.* **2014**, 1.

(23) Lu, Z.; Xu, W.; Zhu, W.; Yang, Q.; Lei, X.; Liu, J.; Li, Y.; Sun, X.; Duan, X. *Chem. Commun.* **2014**, *50*, 6479.

(24) Friebel, D.; Louie, M. W.; Bajdich, M.; Sanwald, K. E.; Cai, Y.; Wise, A. M.; Cheng, M.-J.; Sokaras, D.; Weng, T.-C.; Alonso-Mori, R.; Davis, R. C.; Bargar, J. R.; Nørskov, J. K.; Nilsson, A.; Bell, A. T. *J. Am. Chem. Soc.* **2015**, *137*, 1305.

(25) Norskov, J. K.; Bligaard, T.; Rossmeisl, J.; Christensen, C. H. *Nat. Chem.* **2009**, *1*, 37.

(26) Kresse, G.; Furthmüller, J. *Phys. Rev. B* **1996**, *54*, 11169.

(27) Hammer, B.; Hansen, L. B.; Nørskov, J. K. *Phys. Rev. B* **1999**, *59*, 7413.

(28) Vanderbilt, D. *Phys. Rev. B* **1990**, *41*, 7892.

(29) Methfessel, M.; Paxton, A. T. *Phys. Rev. B* **1989**, *40*, 3616.

(30) Calle-Vallejo, F.; Koper, M. T. M. *Electrochim. Acta* **2012**, *84*, 3.

(31) Nørskov, J. K.; Rossmeisl, J.; Logadottir, A.; Lindqvist, L.; Kitchin, J. R.; Bligaard, T.; Jónsson, H. *J. Phys. Chem. B* **2004**, *108*, 17886.

(32) Li, Y.-F.; Selloni, A. *ACS Catal.* **2014**, *4*, 1148.

(33) Cavani, F.; Trifirò, F.; Vaccari, A. *Catal. Today* **1991**, *11*, 173.

(34) Suntivich, J.; Gasteiger, H. A.; Yabuuchi, N.; Shao-Horn, Y. *J. Electrochem. Soc.* **2010**, *157*, B1263.

(35) Grimaud, A.; May, K. J.; Carlton, C. E.; Lee, Y.-L.; Risch, M.; Hong, W. T.; Zhou, J.; Shao-Horn, Y. *Nat Commun* **2013**, *4*.

(36) Suntivich, J.; May, K. J.; Gasteiger, H. A.; Goodenough, J. B.; Shao-Horn, Y. *Science* **2011**, *334*, 1383.

(37) Trasatti, S.; Petrii, O. A. *Journal of Electroanalytical Chemistry* **1992**, *327*, 353.

(38) McFarland, E. W.; Metiu, H. *Chem. Rev.* **2013**, *113*, 4391.

(39) Calle-Vallejo, F.; Díaz-Morales, O. A.; Kolb, M. J.; Koper, M. T. M. *ACS Catal.* **2015**, 869.

(40) Calle-Vallejo, F.; Inoglu, N. G.; Su, H.-Y.; Martinez, J. I.; Man, I. C.; Koper, M. T. M.; Kitchin, J. R.; Rossmeisl, J. *Chem. Sci.* **2013**, *4*, 1245.

(41) Trasatti, S. *Electrochim. Acta* **1984**, *29*, 1503.

(42) Bajdich, M.; García-Mota, M.; Vojvodic, A.; Nørskov, J. K.; Bell, A. T. *J. Am. Chem. Soc.* **2013**, *135*, 13521.

(43) Chen, J.; Selloni, A. *J. Phys. Chem. C* **2013**, *117*, 20002.

(44) Diaz-Morales, O.; Calle-Vallejo, F.; de Munck, C.; Koper, M. T. M. *Chemical Science* **2013**, *4*, 2334.

(45) Kurth, S.; Perdew, J. P.; Blaha, P. *Int. J. Quantum Chem* **1999**, *75*, 889.

(46) Landon, J.; Demeter, E.; İnoğlu, N.; Keturakis, C.; Wachs, I. E.; Vasić, R.; Frenkel, A. I.; Kitchin, J. R. *ACS Catal.* **2012**, *2*, 1793.

(47) Calle-Vallejo, F.; Koper, M. T. M.; Bandarenka, A. S. *Chem. Soc. Rev.* **2013**, *42*, 5210.

(48) Kitchin, J. R.; Nørskov, J. K.; Barteau, M. A.; Chen, J. G. *Phys. Rev. Lett.* **2004**, *93*, 156801.

(49) Gelatt, C. D.; Williams, A. R.; Moruzzi, V. L. *Phys. Rev. B* **1983**, *27*, 2005.

(50) Calle-Vallejo, F.; Martínez, J. I.; García-Lastra, J. M.; Mogensen, M.; Rossmeisl, J. *Angew. Chem. Int. Ed.* **2010**, *49*, 7699.

(51) Grabow, L.; Hvolbæk, B.; Nørskov, J. *Top. Catal.* **2010**, *53*, 298.

Chapter 5

The importance of nickel oxyhydroxide deprotonation on its activity towards electrochemical water oxidation

ABSTRACT

Nickel oxyhydroxide (NiOOH) is extensively used for energy storage and it is a very promising catalyst for the oxygen evolution reaction (OER). However, the processes occurring on the NiOOH surface during charge accumulation and OER are not well understood. This work presents an *in situ* Surface Enhanced Raman Spectroscopy (SERS) study of the pH dependent interfacial changes of the NiOOH catalyst under the working conditions used for OER. We demonstrate the important effect of the electrolyte pH on the degree of surface deprotonation of NiOOH, which crucially affects its OER activity. Our results show that the deprotonation of NiOOH produces negatively charged surface species, which are responsible for the enhanced OER activity of NiOOH in highly alkaline pH. Moreover, we provide spectroscopic evidence obtained in an ^{18}O-labeled electrolyte that allows us to assign this negatively charged species as superoxo-type species (Ni-OO^-). Furthermore, we propose a mechanism for the OER on NiOOH which is consistent with the observed pH-sensitivity, and that also explains why NiOOH is not a suitable catalyst for applications in neutral or moderately alkaline pH (in the range 7 – 11), apart from the lower stability of the catalyst under these conditions.

The content of this chapter is in preparation for publication: Diaz-Morales, O.; Ferrus-Suspedra, D.; Koper, M.T.M.

5.1. Introduction

Nickel-based oxides are extensively used for secondary batteries and super capacitors.[1-3] These materials are also very promising catalysts for the OER,[4-10] which is one of the major bottlenecks for solar energy conversion into storable fuels.[11,12] However, the mechanism of nickel charging and its activation towards OER are still matter of debate. The Bode scheme is one of the accepted mechanisms for the charge/discharge process of the nickel (hydr)oxide, according to which the freshly prepared α-Ni(OH)2 oxidizes to form γ-NiOOH;[13] these phases convert into the more crystalline β-Ni(OH)2 / β-NiOOH phases upon (electro)chemical ageing. It has been proposed that the formal oxidation state of nickel in the γ-NiOOH lies in the range 3.5 – 3.67,[9,14] which suggests that some nickel sites in this compound have NiO_2-like character that may be seen as tetravalent nickel sites; this hypothesis has been supported with X-ray adsorption spectroscopy (XAS), by matching the position of the Ni K-edge of the γ-NiOOH samples with the K-edge of reference compounds in which nickel was thought to be in the Ni^{4+} state ($BaNiO_3$ or $KNiIO_6$).[15-17] However, the values reported for the oxidation state of nickel in those reference compounds did not consider the possibility of oxygen vacancies, which affect the formal valence of nickel in the compounds and make the conclusions derived from the XAS data uncertain.[18,19]

The OER mechanism on a nickel-based catalyst (nickel-borate) was recently studied by Nocera *et al.*,[20] and they proposed that the formation of the catalytically active species for the OER occurs via an oxidative deprotonation of a nickel oxyhydroxide-like structure; the NiOOH proposed by them is dispersed in a polymeric hydrous network similar to the one suggested by Lyons *et al.*[9,21] The charging mechanism of $Ni(OH)_2$ in KOH and its activation towards OER was also studied by Merrill *et al.*[22] by means of Surface Enhanced Raman Spectroscopy (SERS), who reported the appearance of a broad peak in the 900 – 1100 cm^{-1} wavenumber region when α-$Ni(OH)_2$ oxidizes to form γ-NiOOH. This broad feature was attributed to "active oxygen O^0" within the NiOOH structure. The spectroelectrochemical evidence about the active oxygen species within the oxyhydroxide

network raises the question whether this feature may be related to the deprotonated species reported by Nocera *et al.* for the OER active form of nickel-borate catalyst, which heralds the onset of oxygen evolution.

The oxidative deprotonation process to generate the catalytic species for the OER is not particular for nickel. It has been reported that cobalt, iron and manganese-based catalysts also deprotonate prior to oxygen evolution, in processes that are strongly pH-dependent.[23-25] Since the OER activity of NiOOH is also known to be pH-dependent and favored in more alkaline media,[9,21] the appearance of the SERS feature attributed to the "active oxygen" should also correlate with the pH, if this species is related to the formation of OER catalytically active sites in the structure of NiOOH. Following this hypothesis, we present here a systematic *in situ* SERS study of the pH dependence of the catalytic activity of NiOOH towards electrochemical O_2 generation. Our electrodes consist of NiOOH electrodeposited on gold in a rigorously Fe-free electrolyte; the importance of removing such impurities was recently demonstrated by the Boettcher group.[26] The elimination of the Fe impurities from the electrolyte allows us to conclusively rationalize pH-dependent activity changes to observed spectral changes in the γ-NiOOH catalyst. Based on these results, we will suggest a mechanism for OER reaction on first-row transition-metal oxides that we believe will be useful for guiding future first-principles calculations of novel catalysts.

5.2. Experimental Section

All glassware was rigorously cleaned before starting experiments by boiling in concentrated H_2SO_4 to remove metals and organic contaminations, and was subsequently boiled five times in Millipore Milli-Q water (resistivity >18.2 MΩ cm), which was also used to prepare the solutions for the electrochemical experiments.

The chemicals used in this work were of ultra-high purity: $Ni(NO_3)_2 \cdot 6H_2O$ (Aldrich trace metal basis, 99.999%), $HClO_4$ (Aldrich TraceSelect® for trace analysis, 67-72 %) and iron-free NaOH. The purification of commercial NaOH followed the procedure reported by

Boettcher's group,[26] by shaking a 1 M solution of NaOH (30% solution in H_2O, TraceSelect® for trace analysis) with $Ni(OH)_2$ that was precipitated from the 99.999% $Ni(NO_3)_2 \cdot 6H_2O$ salt. The $NaClO_4$ used as supporting electrolyte was prepared by neutralizing the Fe-free NaOH solution with $HClO_4$, to minimize the amount of iron impurities present in the solution. The pH of the solutions used in all the experiments of this work was adjusted with $HClO_4$, and verified with a pH-meter. All experiments were performed at constant ionic strength, which was kept constant at 0.1 M by adding $NaClO_4$ as supporting electrolyte except for the electrolyte at pH 13 and 14, which did not contain $NaClO_4$; they were NaOH 0.1 M and 1 M, respectively.

In situ Surface Enhanced Raman Spectroscopy (SERS) was performed with a confocal Raman microscope (LabRam HR, Horiba Yobin Yvon) with a 50X objective. The excitation source used was a 30 mW He/Ne laser (633 nm). Backscattered light was filtered with an edge filter at 633 nm, subsequently directed to the spectrograph and to the CCD detector; further details of the setup can be found in references [27] and [28]. The experiments were made in a two-compartment and three-electrode cell made of glass, with a quartz window at the bottom. A gold spiral was used as counter electrode, Ag/AgCl (sat. KCl) as reference electrode, and nickel electroplated on a roughened gold disk as working electrode; the reference electrode was separated from the working electrode compartment to avoid chloride contamination. The electrochemical experiments were controlled by a μAutolab type III potentiostat/galvanostat (Metrohm-Autolab). Dissolved oxygen in solutions was removed prior to measurements by purging with argon (purity grade 5.0) for at least 30 min, and the argon was kept flowing above the solution during the experiments.

The working electrode used in this work was a gold disk back-contacted with a gold wire and it was not mounted in any material to allow annealing during the cleaning procedure; the electrochemical measurements were performed with the disk in meniscus configuration. Prior to each measurement, the disk was mechanically polished to mirror finish using aqueous diamond pastes (Buehler Limited) with different grain sizes to 0.25 μm, rinsed with Milli-Q water and ultrasonicated during 5 min to remove all residuals of mechanical polishing; next the gold electrode was annealed with a butane flame and

electrochemically roughened by 25 oxidation-reduction cycles (ORC) in a 0.1 M solution of KCl. The ORC were performed between -0.30 and 1.20 V vs. SCE, during which the potential was held for 30 seconds at the negative limit and for 1.3 seconds at the positive limit; this method is reported to give a brownish surface that is SERS active.[29] The roughened gold electrode was thoroughly rinsed with water to measure a cyclic voltammetry in the potential range 0 – 1.75 V vs. RHE in HClO4 0.1 M at 0.05 V/s. The real surface area of the electrode was measured from the charge of the reduction peak of the gold oxide, assuming 390 $\mu C \cdot cm^{-2}$ for the charge for one monolayer of gold oxide.[30] The surface area obtained from this measurement was used to calculate the current density in the cyclic voltammetry reported in the work. The capacitance-corrected plots of catalytic activity were obtained from the cyclic voltammetry curves by averaging the current of the backward and forward scans.[31,32]

Nickel was plated on the roughened gold electrode by galvanostatic electrodeposition from a $Ni(NO_3)_2 \cdot 6H_2O$ solution $5x10^{-3}$ M, using $NaClO_4$ 0.1 M as supporting electrolyte. The deposition was carried out by applying a cathodic current (10μA) for a given time, in order to get *ca*. five monolayers of coverage; the time for nickel plating was calculated according to the real surface area of the working electrode in order to deposit 5 x 726 $\mu C \cdot cm^{-2}$, the latter value corresponding to the charge needed to deposit one monolayer of closely packed metallic nickel from a Ni^{2+} solution, taking the atomic radius of Ni as 0.124 nm and its density as 8.908 $g \cdot cm^{-3}$.[33]

All potentials in this work are reported versus the reversible hydrogen electrode (RHE) in the working pH, unless otherwise stated. The potentials were converted into the RHE scale according to the equation (1).

$$E_{RHE} = E_{Ag/AgCl\ (sat.\ KCl)} + E^0_{Ag/AgCl\ (sat.\ KCl)} + 0.059 \cdot \Delta pH \quad (1)$$

where E_{RHE} is the potential on the RHE scale, $E_{Ag/AgCl(sat.\ KCl)}$ is the potential applied experimentally and $E^0_{Ag/AgCl\ (sat.\ KCl)}$ is the standard potential of the Ag/AgCl redox couple (in a solution saturated with KCl) on the normal hydrogen electrode scale (0.197 V),[34] ΔpH

accounts for the difference in pH of the working solution respect to the conditions used for the normal hydrogen electrode (pH=0). Equation (1) was verified by measuring the equilibrium potential of platinum in a solution NaOH 0.1 M (pH 13) saturated with H_2.

The Raman experiments in $H_2{}^{18}O$ (98% isotopic purity, GMP standard, purchased from CMR) were performed at pH 13 (NaOH 0.1 M). The electrolyte for these experiments was used without further purification, and the electrochemical cell had a smaller internal volume (*ca.* 1 mL); schematic details of this cell can be found in reference [28].

5.3. Results and Discussion

The cyclic voltammetry (CV) in Figure 1a shows the $Ni(OH)_2$ / NiOOH (Ni^{2+} / Ni^{3+}) redox transition in the potential region 1.3 – 1.5 V vs. RHE. The potential at which the redox transition occurs does not show significant pH dependence (see Figure D1a-b in Appendix D). However, the OER activity (expressed as current density) does depend on the pH of the electrolyte, as confirmed in the capacitance-corrected plot of OER activity as function of the applied potential in Figure D2 in Appendix D. Figure 1a show that the OER activity at pH 11.0 is negligible and increases with the electrolyte pH, with a tendency to saturate at the highest pH values (see Figure D3 in Appendix D).

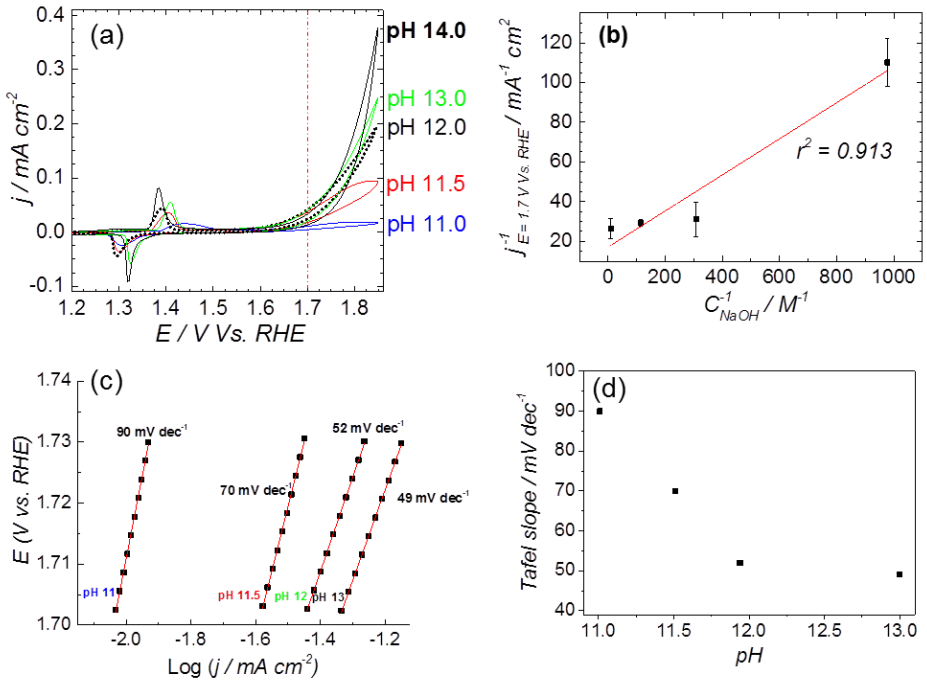

Figure 1. a) CVs of NiOOH deposited on Au, showing the Ni^{2+} / Ni^{3+} redox peaks and the OER activity at E >1.65 V. Measurements at pH 11 – 13 were performed at constant ionic strength, adjusted to 0.1 M with $NaClO_4$ except for pH 13 and pH 14, those solutions solution were NaOH 0.1 M and 1 M, respectively. Scan rate: 0.01 V/s. b) Langmuir-type plot of the OER activity as a function of the concentration of NaOH in the electrolyte (pH 11 – 13), the activity was measured from the CV's as the average of the backwards and forward current density at 1.7 V vs. RHE (red dashed line in a)). c) Tafel plot, obtained from the CV's in a) as the average of the backwards and forward current density in the potential region 1.702-1.73 V vs. RHE. d) Tafel slope as a function of the electrolyte pH.

The potential of the Ni^{2+}/Ni^{3+} transition and the OER current of NiOOH in 1M NaOH (see Figure 1a) compares well with the results reported by Boettcher's group,[26] and confirms that the hydroxide solution was free of iron traces. We can therefore assert that our NiOOH catalyst is not contaminated with Fe during the electrochemical experiments, and the pH effect is not an artifact caused by impurities in the electrolyte. The elimination of Fe impurities in the electrolyte is important because the presence of Fe in the electrolyte

shifts the OER onset potential to lower values due to the formation of NiFe mixed oxyhydroxide ($Ni_{1-x}Fe_xOOH$), which has a higher catalytic activity for oxygen evolution than NiOOH itself;[26] the formation of $Ni_{1-x}Fe_xOOH$ also affects the position of the Ni^{2+} / Ni^{3+} redox transition, and produces an apparent pH dependence of the redox pair (compare Figures D1c-d to Figures D1a-b). Figure D3a-b in Appendix D shows polarization curves of $Ni(OH)_2$ deposited on Au, obtained in purified (Fe-free) and non-purified electrolytes, respectively. The cyclic voltammetry in the Fe-containing electrolytes (Figure D3b in Appendix D) differs from the one obtained in Fe-free electrolyte: the Ni^{2+}/Ni^{3+} redox peaks of NiOOH shift with pH and the OER activity increases *ca.* 20-fold from pH 11 to pH 13 whereas the enhancement is about 10-fold for the purified electrolyte. In general, the activity measured in the Fe-containing electrolyte is *ca.* 10-fold higher than in the Fe-free electrolyte.

The interfacial structural changes during the electrochemical oxidation of $Ni(OH)_2$ and subsequent OER were studied by means of *in situ* SERS at different pH, keeping the ionic strength of the electrolyte constant; Figure 2 shows the results obtained from these experiments.

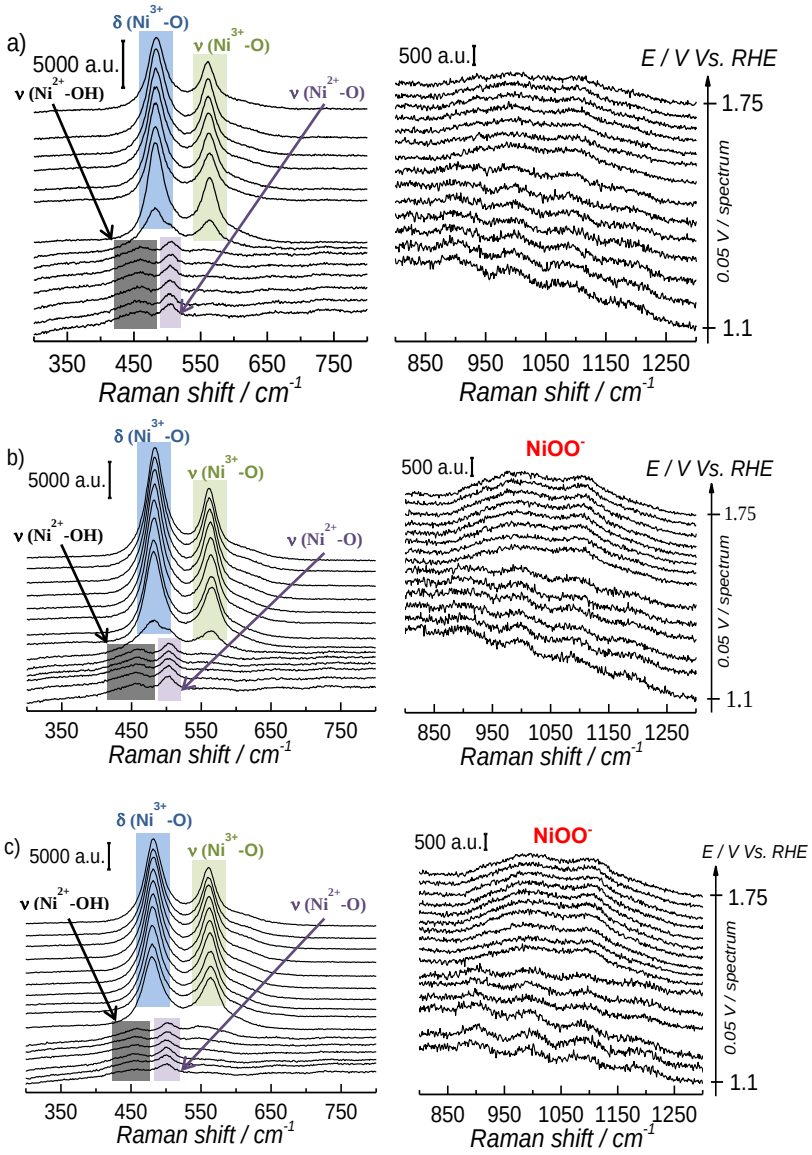

Figure 2. SER spectra obtained at constant potential during the electrochemical oxidation of $Ni(OH)_2$ and the subsequent OER on NiOOH at different pH's. The ionic strength of the solution was fixed to 0.1 M with $NaClO_4$ except for pH 13, that solution is NaOH 0.1 M. The left panel presents the spectra in the wavenumber region 300 – 800 cm^{-1} and the right panel presents the wavenumber region 800 – 1300 cm^{-1}: a) pH 11, b) pH 12.0, c) pH 13.0.

The SERS spectra acquired at potentials below *ca.* 1.4 V vs. RHE show two weak peaks at 457 cm^{-1} and 504 cm^{-1} (see left panel of Figure 2a-c), which can be assigned to the A_{1g} stretching modes of Ni-OH and Ni-O, respectively, in the $Ni(OH)_2$.[35-37] The stretching mode of the dehydrated form of nickel hydroxide (Ni-O peak at *ca.* 504 cm^{-1}) has been attributed to a potential-assisted dehydration process of the nickel hydroxide to NiO-like structures, as expressed in equation (2).[37]

$$Ni(OH)_2 \xrightarrow{E} NiO + H_2O \qquad (2)$$

The $Ni(OH)_2$ / NiOOH redox transition occurs at potentials higher than *ca.* 1.35 V vs. RHE (see Figure 1a), and the SERS spectra in the left panel of Figure 2a-c show the appearance of two well-defined peaks at *ca.* 482 cm^{-1} and 562 cm^{-1} that can be assigned to the e_g bending vibration and the A_{1g} stretching vibration modes, respectively, of Ni-O in NiO(OH).[37] The Raman peaks of $Ni(OH)_2$ are weak in comparison with the intensity observed for the peaks assigned to NiO(OH), as previously reported by Bell's group; this has been attributed to the low Raman scattering cross-section of $Ni(OH)_2$, in contrast to the stronger bands observed for NiO(OH) due to a resonance enhancing effect.[38] At higher potentials, we observe the peak attributed to "active oxygen" in the oxyhydroxide structure; in the 800 – 1150 cm^{-1} wavenumber region. The spectra in the right-hand panel of Figure 2a-c show that the intensity of this peak increases as the pH of the electrolyte becomes more alkaline (spectra taken at pH 11.5 and 14 are shown in Figure D4 in Appendix D).

Our electrochemical results indicate that the oxidation of $Ni(OH)_2$ occurs via a hydroxide-mediated deprotonation process that can be described by the scheme 1.

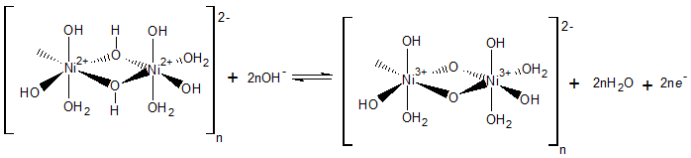

Scheme 1. Electrochemical oxidation of a polymeric hydrous nickel(II) hydroxide.

Scheme 1 shows the Ni^{2+} / Ni^{3+} oxidation process of a polymeric hydrous nickel(II) hydroxide ($[(Ni^{2+})_2(OH)_6(H_2O)_3]_n^{2-}$), which is the actual state of the hydroxide on the electrode surface as reported by Lyons *et al.*[9,21] This redox process is a OH^- / e^- - coupled reaction which should exhibit no pH dependence on the RHE scale.

The $[(Ni^{3+})_2O_2(OH)_4(H_2O)_3]_n^{2-}$ will be further deprotonated if the pH of the electrolyte is higher than pK_a of the proton attached to the NiO(OH) species, leading to formation of a NiO^- species, as shown in scheme 2.

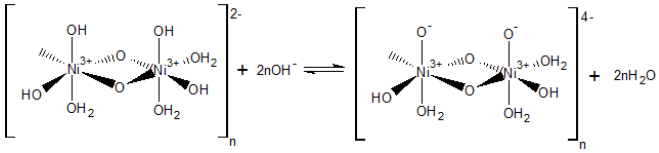

Scheme 2. Hydroxide-mediated deprotonation process of NiO(OH) towards negatively charged oxide.

The reaction presented in scheme 2 is very similar to the activation process towards oxygen evolution proposed by Nocera *et al.*[20] for nickel-borate catalyst, which we have recently shown to be essentially identical to the NiOOH catalyst.[39] Scheme 2 also resembles the mechanism for the photocatalytic water oxidation on Co_3O_4 reported by Frei *et al.*[24] Their spectroscopic and kinetic data show that the deprotonated form of cobalt oxyhydroxide (negatively charged oxide) can produce oxygen through decomposition of the OOH intermediates. However, the reaction rate following this pathway was suggested to be slow and the deprotonated sites in the cobalt-based catalyst were called the "slow sites".

Frei *et al.*[24] also report a vibrational peak at *ca.* 1013 cm^{-1} when the photo-induced OER experiment is performed in $H_2{}^{16}O$. This peak shifts to lower frequencies (*ca.* 18 and 47 cm^{-1}) when the experiment is performed in $H_2{}^{18}O$. Based on the position of the peak in the spectrum and its shift in frequency due to the isotopic labeling, they assigned the

vibrational peak to superoxo intermediates in the cobalt catalyst (CoOO). Moreover, the time-dependence of the peak intensity during the photocatalytic reaction led them to propose that the water oxidation occurs via decomposition of this superoxo species.

Since the frequency of the Raman peak attributed to the "active oxygen" species is very close to the position reported for the infrared peak assigned to the superoxo species on the cobalt-based catalyst,[24] we performed a similar isotopic labeling experiment for the electrocatalytic oxygen evolution on NiOOH to confirm the nature of this species; Figure 3 shows a comparison between the SER spectrum of the "active oxygen" on NiOOH, measured at pH 13 in $H_2{}^{16}O$ and $H_2{}^{18}O$ (at 1.7 V vs. RHE), showing a clear shift of the Raman peak to lower frequencies in the labeled media. The peaks attributed to the "active oxygen" shift *ca*. 15 and 43 cm^{-1} to lower frequencies in $H_2{}^{18}O$ (see table D1 in Appendix D). This corresponds well with the shift observed by Frei *et al*.[24] for the superoxo species in cobalt oxide. The position of the "active oxygen" peak in the spectrum and its shift in $H_2{}^{18}O$ therefore renders further credence to the assertion that the "active oxygen" peak corresponds to a superoxo (O-O) vibration (SERS of NiOOH at pH 13 in $H_2{}^{18}O$ in the potential range of 1.45 – 1.75 V vs. RHE are shown in Figure D5 in the SI).

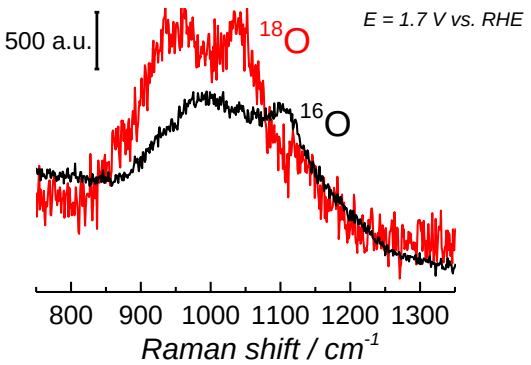

Figure 3. SER spectra of NiOOH in the wavenumber region 800 – 1350 cm^{-1}. The spectra were obtained at 1.7 V vs. RHE in $Na^{16}OH$ 0.1 M. The electrolyte was prepared with $H_2{}^{16}O$ and $H_2{}^{18}O$.

The superoxidic nature of the species in the SER spectra can be further confirmed by comparing the above SERS results to the existing DFT calculations of NiO_2 complexes; the calculations show that NiO_2 has vibrational modes in the wavenumber region 900-1150 cm^{-1},[40] when the O_2 in NiO_2 is of peroxidic or superoxidic character, *i.e.* the 900-1150 cm^{-1} region corresponds to O-O stretching modes.

The dependence of the activity and the corresponding Raman bands on pH suggests that the species is formed upon deprotonation of the γ-NiOOH phase, which has been shown to be the more OER active phase of NiOOH.[26] Moreover, in the light of the abovementioned results reported for the photocatalytic OER on cobalt oxide, [24] the shift of the "active oxygen" Raman peak due to isotopic labeling and its pH-dependence, we conclude that this species is of superoxo nature and acts as precursor for oxygen evolution. As a consequence, we propose that the mechanism for the electrocatalytic OER on NiOOH is similar to the one reported by Nocera *et al.*[20] for the OER on nickel borate, and by Frei *et al.*[24] for the light-assisted water oxidation on Co_3O_4; the reaction occurs via two successive deprotonation steps of the polymeric hydrous nickel oxyhydroxide towards formation of superoxo species ($NiOO^-$), as shown in Figure 4.

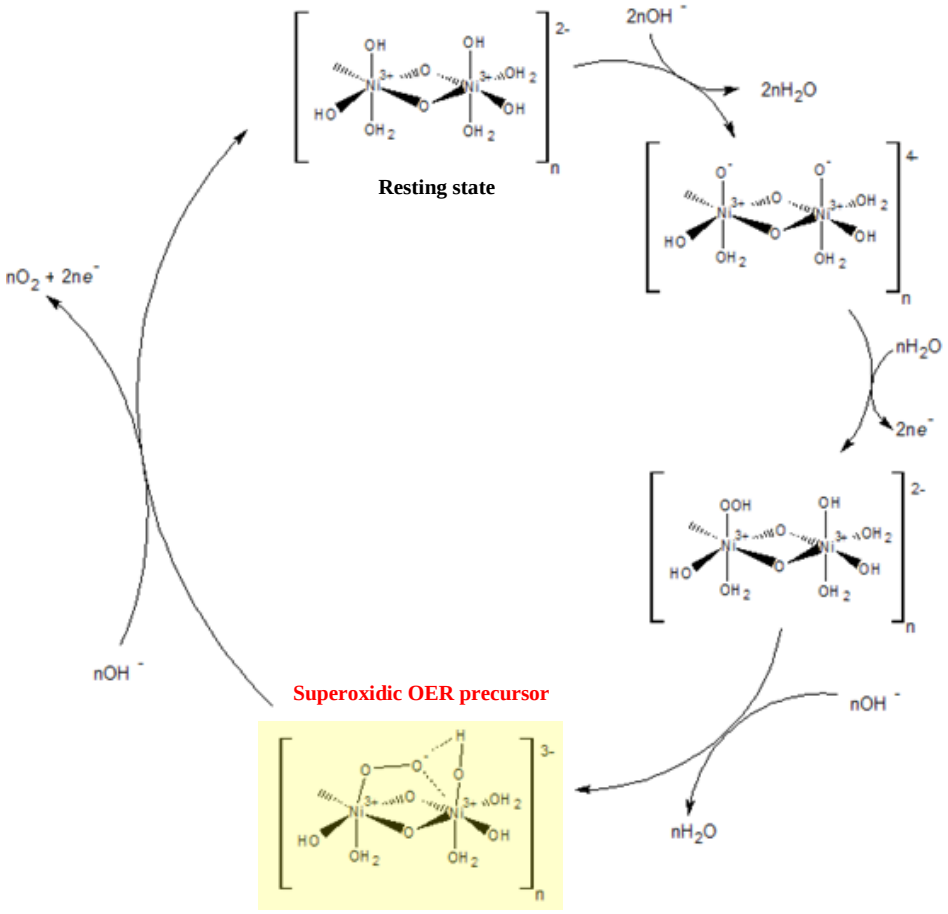

Figure 4. Proposed mechanism for the electrocatalytic oxygen evolution on NiOOH. The resting state corresponds to NiO(OH), which is formed from the hydrous nickel(II) hydroxide in the potential region 1.3 – 1.5 V vs. RHE (corresponding to the Ni^{2+}/Ni^{3+} redox couple observed in the CV of Figure 1a) .

The surface character of the $NiOO^{-}$ species is suggested by the Langmuir-type dependence of the OER activity on the NaOH concentration: a plot of 1/j versus $1/C_{NaOH}$ gives a reasonably straight line (see Figure 1b). The deviation from linearity in the plot of Figure 1b can be attributed to the strong pH dependence of the OER Tafel slope, as can be shown in Figures 1c-d. The Tafel slope for OER on nickel oxyhydroxide varies from *ca.*

90 mV/dec at pH 11 to *ca.* 49 mV/dec at pH 13. Lyons *et al.*[9] reported a similar trend in the values of the Tafel slope in experiments performed at higher concentrations of NaOH (0.1 – 5 M).

In the mechanism suggested in Figure 4, the oxygen evolution reaction may proceed from the negatively charged oxide formed in the first deprotonation step ($[(Ni^{3+})_2O_2(O^-)_2(OH)_2(H_2O)_3]_n^{4-}$) via O_2 formation from the OOH subsequently produced, as suggested for water oxidation on cobalt oxide. However, according to Frei *et al.*,[24] this pathway has a slower reaction rate compared with the mechanism that forms O_2 from the superoxo intermediate, formed in the second deprotonation. The pH-dependence of the NiOOH activity towards OER may in principle be ascribed to both pathways: deprotonation giving rise to the negatively charged oxide and subsequent formation of the O-O bond, or deprotonation giving rise to the negatively charged superoxide. Ultimately, the (surface) pK_a of the corresponding acid-base equilibrium needs to be determined in order to assess which of the two explains the observed pH dependence.

The importance of negatively charged species, either of "O^-" or of "OO^-" character, on the surface of the catalyst during the OER has been suggested for many types of (transition-metal) oxide catalysts,[9,20,21,23,25,41] and their role as O_2 precursors has been proposed for electro- and photocatalytic water oxidation.[20,23,24] However, theoretical descriptions of the OER mechanism employing density functional theory calculations have not yet incorporated this important pH effect in the reaction kinetics.[42] We believe that the data reported here and the associated mechanism suggested in Figure 4 provide another clear experimental example of the importance of negatively charged (surface) intermediates in generating pH dependent electrocatalytic activities, in agreement with a general model reported previously.[43] Further understanding of the role of the oxo (MO^-) and superoxo (MOO^-) intermediates in the OER kinetics would require detailed DFT calculations that consider the pK_a and the relative stabilities of these intermediates. Future computational approaches towards modeling OER should account for this important acid-base surface chemistry.

5.4. Conclusions

In this chapter, we have provided spectro-electrochemical evidence for the active species that is responsible for the pH dependent OER activity of NiOOH in alkaline electrolytes. We identify this species as a deprotonated γ-NiOOH surface phase in which stable (*i.e.* Raman observable) O-O bonds are formed. Based on our observations and other literature data on pH dependent OER kinetics, we propose a mechanism for the OER on NiOOH which is consistent with the observed pH-sensitivity; it involves the formation of a superoxo-type intermediate ($NiOO^-$) that acts as preferential oxygen precursor at pH > 11. The proposed OER mechanism considers a second reaction pathway that forms O_2 from a NiO^- - type intermediate, but with low reaction rate that may explain the lack of OER activity at pH ≤ 11, and allows one to understand the unsuitability of NiOOH as electrocatalyst for applications in neutral or moderately alkaline pH (in the range 7 – 11), apart from the lower stability of the catalyst under these conditions.

5.5. Acknowledgments

This work was also supported by the Netherlands Organization for Scientific Research (NWO) and in part by the BioSolar Cells open innovation consortium, supported by the Dutch Ministry of Economic Affairs, Agriculture and Innovation. D. Ferrus-Suspedra is kindly acknowledged for his assistance with the electrochemical experiments.

REFERENCES

(1) Chen, H.; Cong, T. N.; Yang, W.; Tan, C.; Li, Y.; Ding, Y. *Progress in Natural Science* **2009**, *19*, 291.

(2) Luan, F.; Wang, G.; Ling, Y.; Lu, X.; Wang, H.; Tong, Y.; Liu, X.-X.; Li, Y. *Nanoscale* **2013**, *5*, 7984.

(3) Yang, Q.; Lu, Z.; Liu, J.; Lei, X.; Chang, Z.; Luo, L.; Sun, X. *Progress in Natural Science: Materials International* **2013**, *23*, 351.

(4) Corrigan, D. A.; Bendert, R. M. *J. Electrochem. Soc.* **1989**, *136*, 723.

(5) Doyle, R. L.; Godwin, I. J.; Brandon, M. P.; Lyons, M. E. G. *PCCP* **2013**, *15*, 13737.

(6) Gong, M.; Li, Y.; Wang, H.; Liang, Y.; Wu, J. Z.; Zhou, J.; Wang, J.; Regier, T.; Wei, F.; Dai, H. *J. Am. Chem. Soc.* **2013**, *135*, 8452.

(7) Lu, Z.; Xu, W.; Zhu, W.; Yang, Q.; Lei, X.; Liu, J.; Li, Y.; Sun, X.; Duan, X. *Chem. Commun.* **2014**, *50*, 6479.

(8) Lyons, M. E. G.; Brandon, M. P. *International Journal of Electrochemical Science* **2008**, *3*, 1386.

(9) Lyons, M. E. G.; Cakara, A.; O'Brien, P.; Godwin, I.; Doyle, R. L. *International Journal of Electrochemical Science* **2012**, *7*, 11768.

(10) Matsumoto, Y.; Sato, E. *Materials Chemistry and Physics* **1986**, *14*, 397.

(11) Lewis, N. S.; Nocera, D. G. *Proc. Natl. Acad. Sci. U. S. A.* **2006**, *103*, 15729.

(12) Joya, K. S.; Joya, Y. F.; Ocakoglu, K.; van de Krol, R. *Angew. Chem. Int. Ed.* **2013**, *52*, 10426.

(13) Bode, H.; Dehmelt, K.; Witte, J. *Electrochim. Acta* **1966**, *11*, 1079.

(14) Oliva, P.; Leonardi, J.; Laurent, J. F.; Delmas, C.; Braconnier, J. J.; Figlarz, M.; Fievet, F.; Guibert, A. d. *J. Power Sources* **1982**, *8*, 229.

(15) Hu, Y.; Bae, I. T.; Mo, Y.; Scherson, D. A.; Antonio, M. R. *Can. J. Chem.* **1997**, *75*, 1721.

(16) Mansour, A. N.; Melendres, C. A.; Pankuch, M.; Brizzolara, R. A. *J. Electrochem. Soc.* **1994**, *141*, L69.

(17) O'Grady, W. E.; Pandya, K. I.; Swider, K. E.; Corrigan, D. A. *J. Electrochem. Soc.* **1996**, *143*, 1613.

(18) Gottschall, R.; Schöllhorn, R.; Muhler, M.; Jansen, N.; Walcher, D.; Gütlich, P. *Inorg. Chem.* **1998**, *37*, 1513.

(19) Qian, X.; Sambe, H.; Ramaker, D. E.; Pandya, K. I.; O'Grady, W. E. *J. Phys. Chem. B* **1997**, *101*, 9441.

(20) Bediako, D. K.; Surendranath, Y.; Nocera, D. G. *J. Am. Chem. Soc.* **2013**, *135*, 3662.

(21) Lyons, M. E. G.; Doyle, R. L.; Brandon, M. P. *PCCP* **2011**, *13*, 21530.

(22) Merrill, M.; Worsley, M.; Wittstock, A.; Biener, J.; Stadermann, M. *J. Electroanal. Chem.* **2014**, *717–718*, 177.

(23) Surendranath, Y.; Kanan, M. W.; Nocera, D. G. *J. Am. Chem. Soc.* **2010**, *132*, 16501.

(24) Zhang, M.; de Respinis, M.; Frei, H. *Nat Chem* **2014**, *6*, 362.

(25) Takashima, T.; Hashimoto, K.; Nakamura, R. *J. Am. Chem. Soc.* **2012**, *134*, 1519.

(26) Trotochaud, L.; Young, S. L.; Ranney, J. K.; Boettcher, S. W. *J. Am. Chem. Soc.* **2014**, *136*, 6744.

(27) Lai, S. C. S.; Kleyn, S. E. F.; Rosca, V.; Koper, M. T. M. *Journal of Physical Chemistry C* **2008**, *112*, 19080.

(28) Diaz-Morales, O.; Calle-Vallejo, F.; de Munck, C.; Koper, M. T. M. *Chem. Sci.* **2013**, *4*, 2334.

(29) Gao, P.; Gosztola, D.; Leung, L. W. H.; Weaver, M. J. *J. Electroanal. Chem.* **1987**, *233*, 211.

(30) Trasatti, S.; Petrii, O. A. *Journal of Electroanalytical Chemistry* **1992**, *327*, 353.

(31) Grimaud, A.; May, K. J.; Carlton, C. E.; Lee, Y. L.; Risch, M.; Hong, W. T.; Zhou, J.; Shao-Horn, Y. *Nat. Commun.* **2013**, *4*.

(32) Suntivich, J.; May, K. J.; Gasteiger, H. A.; Goodenough, J. B.; Shao-Horn, Y. *Science* **2011**, *334*, 1383.

(33) House, J. *Inorganic Chemistry*; 2nd ed.; Academic Press: Waltham, 2013.

(34) West, R. *Handbook of Chemistry and Physics*; 53rd ed.; CRC Press Cleveland, 1972.

(35) Hermet, P.; Gourrier, L.; Bantignies, J. L.; Ravot, D.; Michel, T.; Deabate, S.; Boulet, P.; Henn, F. *Phys. Rev. B* **2011**, *84*, 235211.

(36) Li, H. B.; Yu, M. H.; Wang, F. X.; Liu, P.; Liang, Y.; Xiao, J.; Wang, C. X.; Tong, Y. X.; Yang, G. W. *Nat Commun* **2013**, *4*, 1894.

(37) Lo, Y. L.; Hwang, B. J. *Langmuir* **1998**, *14*, 944.

(38) Yeo, B. S.; Bell, A. T. *J. Phys. Chem. C* **2012**, *116*, 8394.

(39) Trzesniewski, B. J.; Diaz-Morales, O.; Vermaas, D.; Longo, A.; Bras, W.; Koper, M. T. M.; Smith, W. A. **submitted, 2015**.

(40) Uzunova, E. L.; Mikosch, H.; Nikolov, G. S. *The Journal of chemical physics* **2008**, *128*, 094307.

(41) Nguyen, A. I.; Ziegler, M. S.; Oña-Burgos, P.; Sturzbecher-Hohne, M.; Kim, W.; Bellone, D. E.; Tilley, T. D. *J. Am. Chem. Soc.* **2015**.

(42) Rossmeisl, J.; Qu, Z. W.; Zhu, H.; Kroes, G. J.; Norskov, J. K. *J. Electroanal. Chem.* **2007**, *607*, 83.

(43) Koper, M. T. M. *Chem. Sci.* **2013**, *4*, 2710.

Chapter 6

Iridium-based double perovskites for efficient water oxidation in acid media

ABSTRACT

The development of active, cost-effective and stable anodes for the oxygen evolution reaction (OER) is one of the major challenges for the solar-to-fuel conversion towards sustainable energy generation. IrO2 is the most active catalyst for OER in acid media, and the only one having long-term stability, but it is prohibitively expensive for large-scale applications. The design of new catalysts with lower amounts of the scarce but active and stable iridium is an attractive alternative to overcome this economical constraint. In this work, we report a new type of OER anodes based on iridium double perovskites which contain three times less iridium and exhibit a more than 3-fold higher activity per cm2 of real surface area for OER in acid media compared to IrO2, with more than 90% Faradaic efficiency. We show that these compounds are the most active catalysts for OER in acid media reported to date, according to recently suggested benchmarking criteria.

The content of this chapter is the basis of a patent application, and a manuscript has been submitted for publication: Diaz-Morales O.; Raaijman, S.; Kortlever, R.; Kooyman, P. J.; Wezendonk, T.; Gascon, J.; Fu, W.T. and Koper, M.T.M.

6.1. Introduction

Energy generation by burning fossil fuels has huge environmental effects. The steady increase of the global population, with the concomitant increase in energy needs, requires the development of clean and renewable sources of energy for a sustainable society in the future.[1-3] Solar energy is by far the largest exploitable resource, but its availability is neither temporal nor geographically constant so that its large-scale storage will be a crucial step toward the use of this form of energy as a viable alternative.[2-4] Photo-electrochemical generation of fuels (hydrogen or hydrocarbons) is a promising way to store solar energy. However, the slow kinetics of the anode reaction (water oxidation, or oxygen evolution reaction OER) and the lack of a stable, abundant, and cost-effective OER catalyst limit its large-scale application.[5]

Anodes for OER also find widespread utilization in acid electrolyzers and in technical electrochemistry applications requiring a stable and energy-efficient anode (such as electroplating and electrowinning).[6,7] The current anode material of choice for acid-based industrial operation is TiO_2-stabilized iridium oxide or ruthenium oxide, also known as the Dimensionally Stable Anode (DSA).[6,8-11] Iridium oxide is the most efficient material for the OER in acid media among all transition metal oxides, and the only one having long-term stability.[6,12,13]

In alkaline media, oxides based on earth abundant 3d transition metals such as Ni, Co, Mn and Fe show good stability and activity,[14-18] sometimes even higher than the expensive and scarce IrO_2 and RuO_2, and are typically used as anode materials in alkaline electrolyzers.[19,20] However, the kinetics for hydrogen generation is slower in alkaline media than in acid[21,22]. Furthermore, the electrolytes typically used in alkaline electrolyzers have low conductivities; this causes high Ohmic losses in the device and limits the maximum achievable current to about 0.3 A cm^{-2}, much lower than the values achievable by proton exchange membrane electrolyzers (PEM), which are higher than 1.6 A cm^{-2}.[19,20] Such high current densities are required for large-scale and cost-efficient applications of water electrolysis. Moreover, the diaphragms used to separate the anode and cathode chamber in

the alkaline electrolyzers do not completely prevent the product gases from cross-diffusing, which also compromises the efficiency and safety of these devices[23]. PEM electrolyzers overcome this problem by using proton exchange membranes (*eg.* perfluorinated Nafion® membranes) that are efficient gas separators, but this type of membranes is unsuitable in alkaline media.[24]

Iridium is one of the rarest metals on earth, and its high price makes it unsuitable for large scale application. Therefore, development of active and stable OER catalysts with a lower amount of the expensive but highly active iridium[25,26], in combination with iridium recycling, is an alternative avenue (and may presently well be the most realistic avenue) for the extensive application of hydrogen/hydrocarbon generation in solar energy storage, as well as for the development of cheaper and more efficient anodes for the electrochemical industry.

This work reports on a new class of OER catalysts based on iridium double perovskites which contain three times less iridium and yet exhibit a more than 3-fold higher activity per cm2 of real surface area (see Experimental Section for details) for OER in acid media compared to IrO_2, with a similar stability. We will show that these compounds are the most active catalysts for OER in acid media reported till now, according to recently suggested benchmarking criteria.[18]

Double perovskites are compounds with the generic formula $A_2BB'O_6$, with *A* being a large cation and *B* and *B´* being smaller cations. The crystal structure of the ideal double perovskite is depicted schematically in Figure 1(a), showing the three-dimensional network of corner-shared octahedra BO_6 / $B'O_6$ with the *A* cations located in the cavity composed of 8 BO_6 / $B'O_6$ octahedra.[27-29] A wide range of compounds can be prepared by different combinations of *A*, *B* and *B´* cations, which allows fine tuning of the double perovskites components. This feature is used in our work to obtain insight in the parameters affecting the catalytic activity of the A_2BIrO_6 double perovskites, with *A* = Ba, Sr and *B* = La, Ce, Pr, Nd, Tb, Y.

6.2. Experimental Section

6.2.1. Chemicals

The water used to prepare solutions and clean glassware was deionized and ultrafiltrated with a Millipore Milli-Q system (resistivity = 18.2 MΩ·cm and TOC< 5 ppb). All chemicals used in this work were of high purity (pro analysis grade or superior) and they were used without any further purification. The perchloric acid used for the electrolyte was from Merck (70-72%, EMSURE®).

6.2.2. Synthesis and characterization of the iridium-based catalysts

Ba_2MIrO_6 (M= La, Ce, Pr, Nd, Tb and Y), Sr_2YIrO_6, Sr_2IrO_4 and Pr_3IrO_7 were prepared, respectively, from $BaCO_3$, $SrCO_3$, La_2O_3, CeO_2, Pr_6O_{11}, Nd_2O_3, Tb_4O_7, Y_2O_3 and metallic iridium powder, respectively, in alumina crucibles, using the standard solid-state reactions described in references.[30-33] All reactions were carried out in air and the products were furnace-cooled to room temperature. The powders were intermittently reground during the synthesis.

The suspension of iridium oxide nanoparticles was prepared by hydrolysis of Na_2IrCl_6 in alkaline media at 90 °C, to form $[Ir(OH)_6]^{2-}$ intermediate; the particles were generated by an acid-catalyzed condensation of this intermediate.[34]

X-ray powder diffraction patterns were collected on a Philips X'Pert diffractometer, equipped with the X'Celerator, using Cu-Kα radiation in steps of 0.020º (2θ) with 10 s counting time in the range $10º < 2\theta < 100º$.

6.2.3. Electrochemical experiments

Glassware was cleaned by boiling in a 3:1 mixture of concentrated sulfuric acid and nitric acid to remove organic contaminations, after which it was boiled five times in water. When not in use, the glassware was stored in a solution 0.5 M H_2SO_4 and 1 g/L $KMnO_4$. To clean the glassware from permanganate solution, it was rinsed thoroughly with water and

then immersed in a solution 1:1 of concentrated H_2SO_4 and 30% H_2O_2 to remove the MnO_2 particles, after which it was rinsed with water again and boiled five times in ultrapure water.

The electrochemical measurements were carried out at room temperature in a two compartment electrochemical cell with the reference electrode separated by a Luggin capillary. Measurements were performed using a homemade rotating Pt ring – Au disk electrode (ϕ_{disk} = 4.6 mm) as working electrode, a gold spiral as counter electrode and a reversible hydrogen electrode (RHE) as reference electrode; a platinum wire was connected to the reference electrode through a capacitor of 10 μF, acting as a low-pass filter to reduce the noise in the low current measurements. The electrochemical measurements were controlled with a potentiostat/galvanostat (PGSTAT12, Metrohm-Autolab) and they were performed either with cyclic voltammetry at 0.01 V/s or with potentiostatic steps of 0.02 V every 30 seconds. The latter procedure is referred to as steady-state measurements. Before and between measurements the working electrode was polished with 0.3 μm and 0.05 μm alumina paste (Buehler Limited), subsequently it was ultrasonicated in water for 5 minutes to remove polishing particles. The electrolyte was saturated with air prior to the experiments by bubbling for 20 min with compressed air, with the air first passed through a 6 M KOH washing solution. The rotating ring-disk (RRDE) experiments to measure the faradaic efficiency were carried out with the electrolyte saturated with argon, which was purged through for at least 30 min prior to the experiment and kept passing above the solution during the measurement. For RRDE measurements, the Pt ring was kept at 0.45 V vs. RHE while the disk with the catalyst loaded was scanned at 0.01 V/s in the potential range 1.25 – 1.75 V vs. RHE.

The catalysts were immobilized on the Au disk by drop-casting an ethanol-based ink of the oxides, using Na-exchanged neutral Nafion as binder.[35] The inks were prepared to yield the following final concentrations: 1 mg_{oxide}/mL_{ink} and 0.7 mg_{Nafion}/mL_{ink}.[36] Prior to the preparation, the powders were ground in a mortar to eliminate big clusters. The appropriate amount of ink was drop-casted on the electrode to obtain 15 $\mu g_{oxide}/cm_{disk}^2$ of

loading and this electrode was dried in vacuum; cm_{disk}^2 refers to the geometrical surface area of the Au disk.

The current densities reported in this work were calculated with the electrochemical surface area, obtained from pseudo-capacitance measurements, assuming 60 $\mu F \cdot cm^{-2}$ for the specific capacitance of the double layer.[18,37] The Tafel plots were corrected for the Ohmic resistance of the electrolyte, the resistance was measured by Electrochemical Impedance Spectroscopy and by conductimetry[18] and the value obtained was $24 \pm 1\ \Omega$.

6.3. Results and Discussion

The catalytic activity (measured as the current density) towards OER in 0.1 M $HClO_4$ (pH=1) was studied for iridium-based double perovskites with the same *A*-cation (Ba), but changing the *B* cations (La, Ce, Pr, Nd, Tb and Y). The electrodes were prepared by drop-casting an ethanol-based ink of the double perovskites on a rotating ring-disk electrode and the electrochemical experiments were carried out under rotating conditions (see Experimental section for further details). The structure of the double perovskites was verified by powder XRD and the patterns obtained agree with those reported in the literature,[30,31,38] as shown in Figures E1-E7 in Appendix E. Figure 1b summarizes the measured catalytic activities in the form of Tafel plots and compares it with IrO_2 nanoparticles that have been reported as the activity benchmark for OER in acid media.[18] The observed activity of the IrO_2 nanoparticles compares well with the activity reported previously for similar IrO_2 nanoparticles.[18,39] The current density was obtained by normalizing the measured current with respect to the real oxide surface area, as obtained by pseudo-capacitance measurements, following the procedure suggested by Trasatti and Petrii[37] and further developed by McCrory *et al.*[18] (see Experimental section for further details). This procedure of surface area determination is preferred over the Brunaur-Emmet-Teller (BET) method, based on the physical absorption of a gas on the oxide powder, because it allows us to estimate the active electrochemical surface area that can be very different from the real surface area estimated by the BET physical adsorption method.[37]

All Ir-based double perovskites show a more than 3-fold higher catalytic activity per cm^2 of real surface area towards oxygen evolution compared with the benchmarking IrO_2 nanoparticles. Their activity depends on the lanthanide in the B-site, in the order Ce ≈ Tb < La ≈ Pr < Nd. Substitution of the A-site cation can also affects the catalytic activity as is illustrated in Figure 1c which shows that catalytic activity of Sr_2YIrO_6 is higher compared with its barium equivalent. The iridium double perovskites with strontium and lanthanides were also prepared but we did not manage to prepare pure phases of these compounds. Only Sr_2YIrO_6 formed a single phase, hence it was the only iridium double perovskite with strontium used for the electrochemical characterization of the OER activity.

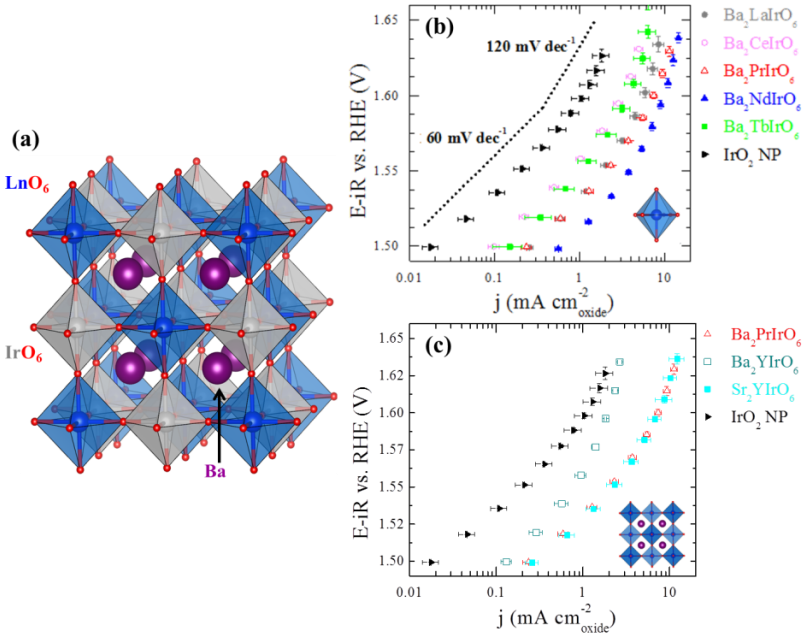

Figure 1. a) Schematic representation of the crystal structure of a generic Ba_2LnIrO_6 double perovskite. b) Catalytic activity to OER in 0.1 M $HClO_4$ of Ir-based double perovskites with A = Ba and with different lanthanides, compared to the benchmark activity IrO_2 nanoparticles; the dashed line shows Tafel slopes of 60 and 120 mV/dec, to guide the eye. c) Effect of the lanthanides and barium substitution on the catalytic activity for water oxidation in 0.1 M $HClO_4$ M of the Ir-based double perovskite. Measurements were performed in hydrodynamic conditions at 1500 RPM.

Both the IrO_2 nanoparticles and the iridium-based double perovskites show two values for the Tafel slope, *ca.* 60 mV/dec between 1.5 and 1.6 V vs. RHE and 120 mV/dec at potentials higher than 1.6 V (numerical values are given in table E1 in Appendix E). This feature has been reported previously for IrO_2 and was explained by a change in the mechanism for OH adsorption, which is thought to be the rate determining step for oxygen evolution on iridium oxide.[40,41] We note, however, that the Tafel slope measured at high electrode potentials for Ba_2YIrO_6 (196 $\pm$ 23 mV/dec) markedly deviates from the values for the iridium-based double perovskites (*ca.* 120 mV/dec).

The catalytic activity towards OER sensitively depends on the crystal structure of the iridium-based catalyst. Figure 2a-b compares the activity of the Ba_2PrIrO_6 and Sr_2YIrO_6 double perovskites with Sr_2IrO_4 and Pr_3IrO_7 (XRD for these compounds are shown in Figure E8-E9 in Appendix E). The catalytic activity of Sr_2IrO_4 is quite similar to that of Sr_2YIrO_6 (see Figure 2a); whereas that of Pr_3IrO_7 is 10-fold lower than the Ba_2PrIrO_6, though comparable to the activity of the IrO2 nanoparticles. The structure of Sr_2IrO_4 and Pr_3IrO_7 also contain the corner-shared IrO_6 octahedra, but differ from that of the double perovskite in the network arrangement. The Sr_2IrO_4 forms two-dimensional (2D) perovskite-like layers,[32,42] separated by a rock salt layer of SrO (see Figure 2c), whereas in the Pr_3IrO_7, the IrO_6 octahedra are linked by sharing the corner oxygen and form one-dimensional (1D) chains[33] (see Figure 2d).

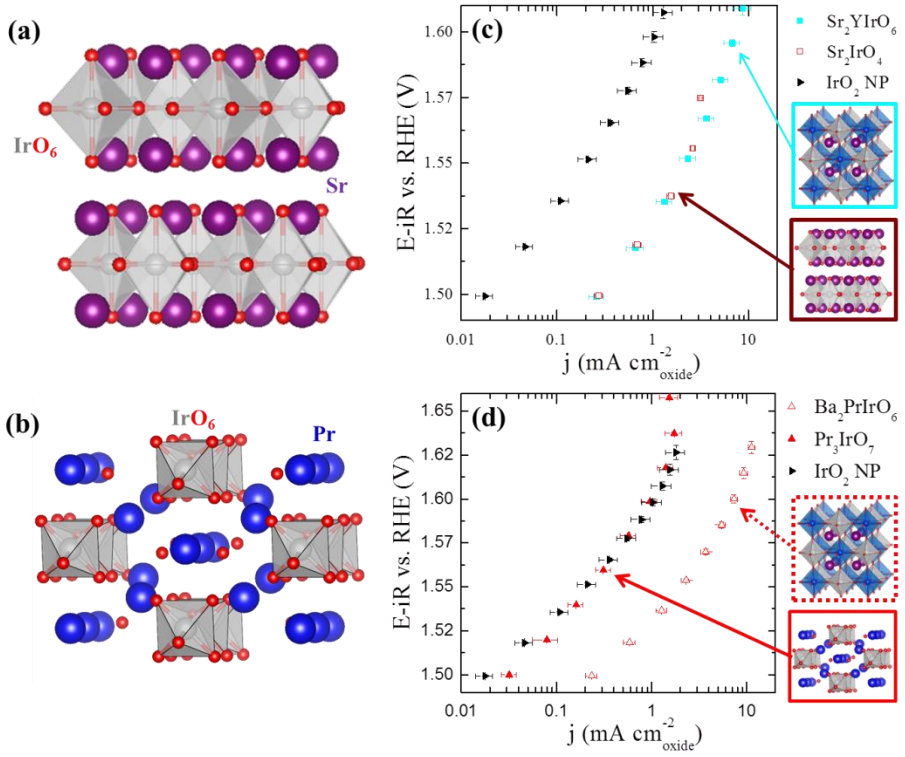

Figure 2. a) Crystal structure of Sr_2IrO_4, showing the 2D network of corner-shared octahedra. b) Crystal structure of Pr_3IrO_7, showing the 1D network of corner-shared octahedra. c) Catalytic activity for OER in 0.1 M $HClO_4$ M of Sr_2YIrO_6 double perovskites in comparison with Sr_2IrO_4 perovskite-like structure. d) Catalytic activity for water oxidation in 0.1 M $HClO_4$ of Ba_2PrIrO_6 double perovskites in comparison with Pr_3IrO_7 fluorite-like structure. Measurements were performed at steady-state conditions at 1500 RPM. The benchmark activity of IrO_2 nanoparticles is shown as benchmark.

The results shown in Figure 2c-d suggest that the 2D arrangement of corner-shared octahedra is the minimal condition to obtain the enhanced catalytic activity of the iridium-based perovskite-like compounds with respect to conventional IrO_2. However, stability under the anodic working conditions is observed only with the extended 3D arrangement of corner-share octahedral of the double perovskites, as illustrated in the voltammetry data shown in Figure E10 in Appendix E. The Sr_2IrO_4 is certainly catalytically active towards

OER in the first cycle(s), but it tends to deactivate after a number of oxygen evolution cycles in the acid environment.

The electrochemical stability of the Ir-based double perovskites was assessed by galvanostatic electrolysis, in a manner similar to the approach reported by the JCAP group.[18] The experiment was performed by applying 10 mA cm_{disk}^{-2} for 1 h (cm_{disk}^{-2} refers to the geometrical surface area of the electrode), and the Ohmic drop-corrected overpotential for OER after 1 h of electrolysis is plotted versus the overpotential measured at the beginning of the experiment (t = 0 s). Figure 3 summarizes the results obtained from these experiments. The stability of IrO_2 nanoparticles is presented for comparison. The diagonal dashed line represents the expected response of a stable catalyst.

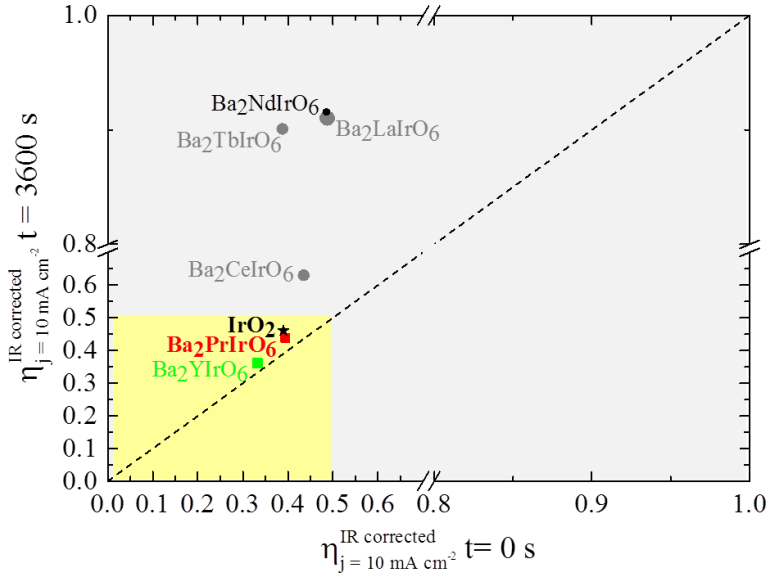

Figure 3. Illustration of the stability of the Ir-based double perovskites and IrO_2 nanoparticle under anodic condition for electrochemical water oxidation in 0.1 M $HClO_4$. The Ohmic drop-corrected overpotential measured after 1 h of galvanostatic electrolysis at 10 mA cm_{disk}^{-2} in hydrodynamic conditions (ω = 1500 RPM) is plotted as a function of the initial overpotential.

The results in Figure 3 show that Ba_2PrIrO_6 and Ba_2YIrO_6 are electrochemically stable, and show similar stability as the IrO_2, which is the state-of-the-art catalyst for OER in acid. The electrochemical stability of these compounds can be illustrated by a plot of Ohmic drop-corrected overpotential as a function of time obtained from the galvanostatic electrolysis (see Figure E10 in Appendix E). During such a time-dependent electrolysis, the Ba_2PrIrO_6 and Ba_2YIrO_6 compounds show even better stability in terms of overpotential than the IrO_2 catalyst. The lanthanum, neodymium and terbium- containing double perovskites are also very active towards OER in acid media according to the JCAP benchmarking, with an overpotential for 10 mA cm^{-2} in the range 0.4 – 0.5 V (see Figure 3). However, they lose their activity after 1 h of galvanostatic electrolysis as expressed by their higher OER overpotentials after 1 h of electrolysis.

In order to assess the structural stability of the Ir-based double perovskites, Ba_2PrIrO_6 was characterized by TEM and XRD after 48 h of leaching treatment in harsh media, namely 0.1 M $HClO_4$ and in 0.1 M $HClO_4$ + 4 M H_2O_2. The Ba_2PrIrO_6 compound was selected for these experiments because it was one of the compounds that showed to be electrochemically stable (see Figure 3), hence we wanted to assess whether it is also structurally stable. The open-circuit potentials of the Ba_2PrIrO_6 double perovskite in 0.1 M $HClO_4$ solution and in 0.1 M $HClO_4$ + 4 M H_2O_2 solution were measured to be 1.3 and 1.1 V vs. RHE, respectively. Therefore the characterization of the powder leached in these two solutions should give a hint about the stability of the double perovskite in acid at the onset of the OER. The TEM images in Figures E11 – E16 in Appendix E show that all the pristine iridium-based double perovskites consist of rather large particles (*ca.* 0.5 – 2 μm), consistent with the sharp lines in XRD pattern (see Figure E1-E7 in Appendix E). The particle size of the Ba_2PrIrO_6 powders leached in 0.1 M $HClO_4$ and 0.1 M $HClO_4$ + 4 M H_2O_2 (Figures E17 – E18 in Appendix E) and the XRD pattern (Figure E19 in Appendix E) remains virtually the same. This shows that the crystal structure of the double perovskite is preserved during the leaching treatment. However, there are a higher number of smaller particles (particle size below 200 nm) in the samples that were leached than in the pristine compound (see Figure E13 in comparison with Figures E17 – E18 in Appendix E). This

suggest that Ba_2PrIrO_6 either cleaves or partially dissolves during the leaching treatment but this process seems to be slow, therefore the average particle size is still large so that no significant broadening is observed in the XRD pattern (see Figure E19 in Appendix E).

We also characterized the surface composition of the pristine and leached samples of the Ba_2PrIrO_6 double perovskite by means of X-ray photoelectron spectroscopy (XPS). The results of this analysis are summarized in Figure E20 and table E2 in Appendix E. The main conclusion derived from this study is that the surface of the double perovskite is not stable upon the acid and the oxidative treatment. XPS results indicate that surface enrichment in iridium occurs upon both leaching treatments of Ba_2PrIrO_6, whereas the barium surface contribution reduces *ca.* 3-fold after leaching in 0.1 M $HClO_4$ and 4-fold after treatment with 0.1 M $HClO_4$ + 4 M H_2O_2, with respect to the pristine compound. Regarding the oxidation state of iridium in the pristine and treated samples, our results show that the surface iridium sites contain a mixture of Ir(IV) and Ir(V), and become enriched in Ir(V) upon the leaching treatments (see Figure E21 in Appendix E).

The leaching of the components of the Ba_2PrIrO_6 double perovskite during electrochemical experiments for oxygen evolution was also assessed by elemental analysis of the electrolyte after electrolysis experiments of one hour at constant electrode potential (see table E3 in Appendix E). The analysis indicates that approximately 10% of Ba and Pr are leached out of the double perovskites in the potential region 1.45 – 1.55 V vs. RHE; however, a negligible amount of iridium dissolves (less than 1%). These results are consistent with the evidence from XPS, indicating that barium and praseodymium are superficially removed at oxidative potentials but that these surface changes do not affect the bulk of the double perovskite, and therefore do not change the XRD pattern, and do not impact on the electrochemical stability of the perovskite as evaluated by the JCAP protocol.

Summarizing, the galvanostatic electrolysis results and the characterization by TEM and XRD show that the bulk of the Ba_2PrIrO_6 double perovskite is electrochemically and structurally stable in acid environment under oxidative conditions. However, the XPS and elemental electrolyte analyses indicate that the surface of the compound changes under

oxidative conditions, becoming enriched in iridium (which tends to be converted to the Ir(V) state) with approximately 10% of Ba and Pr dissolved from the double perovskite.

Finally, we measured the Faradaic efficiency of Ba_2PrIrO_6 towards OER in 0.1 M $HClO_4$ in a rotating ring-disk electrode (RRDE) configuration. The result of this measurement is shown in Figure E22 in the Appendix E and shows that Ba_2PrIrO_6 has high efficiency towards water oxidation, higher than 90% at 1.50 V vs. RHE (0.27 V of overpotential). The Faradaic efficiency appears to decrease with the more anodic electrode potential, which can be explained by the large current for oxygen evolution at $E \geq 1.6$ V vs. RHE, leading to the formation of oxygen bubbles which reduces the detection efficiency on the ring. The double perovskites have very high tendency to bubble formation (due to their high activity) even at low OER overpotentials, which reduces the amount of dissolved O_2 detected at the ring and therefore the reported Faradaic efficiency. This can explain the apparent 10% efficiency loss at 0.27 V of overpotential.

Regarding the high activity measured for the Ir-based double perovskites, Calle-Vallejo *et al.*[43] showed that the oxygen adsorption energy on ABO_3 simple perovskites (with B = Sc, Ti, V, Cr, Mn, Fe, Co, Ni, Cu and A = La, Y) is slightly lower for the yttrium based perovskites and they suggest this might be due to strains in the crystal lattice caused by the smaller Y, in comparison with La. This was also observed for the 3d transition metal perovskites with A = Ba, Sr, strontium-based perovskites showing slightly weaker binding energy than the barium equivalent. Since the IrO_2 has been reported to bind oxygen too strongly to be a truly optimal catalyst,[44,45] the lattice strain caused by substitution of smaller lanthanides or yttrium could weaken the oxygen adsorption energy and therefore improve the catalytic activity of the iridium-based double perovskites in comparison with iridium oxide. The catalytic activity of Ba_2CeIrO_6 shows an additional effect related with the tetravalent oxidation state of the iridium centers;[31,38] this increases the binding energy of adsorbates[43] and may explain why the cerium compound is the least active in the series. In addition, the observed surface leaching may also contribute to the enhancement of the OER catalytic activity of the perovskite surface by leaving behind highly active iridium centers.

6.4. Conclusions

We have reported a new family of iridium-based double-perovskite electrocatalysts with superior activity for water oxidation in acid media. Compared to IrO_2, the state-of-the art benchmarking catalyst, these compounds contains three times less iridium, and exhibit a more than 3-fold higher catalytic activity per cm^2 of real surface area for the oxygen evolution reaction. Our results show that a 3D network of corner-shared octahedra is a necessary prerequisite for the catalytic activity enhancement of the iridium-based double perovskites and for their chemical stability under anodic working conditions. Our findings regarding the effect of the A and B-site cations on the catalysis towards water splitting of the iridium based double perovskite suggest that the activity of these compounds might be further improved by carefully selecting the cations at those sites. Our strategy could also be extended to enhance the catalytic activity and chemical stability of ruthenium-containing compounds, with lower content of ruthenium compared with RuO_2.

6.5. Acknowledgments

This work was also supported by the Netherlands Organization for Scientific Research (NWO) and in part by the BioSolar Cells open innovation consortium, supported by the Dutch Ministry of Economic Affairs, Agriculture and Innovation. Dr. W.T. Fu is kindly acknowledged for his assistance with the synthesis of the double perovskites and their XRD characterization. Dr. P. Kooyman and R. Kortlever are acknowledged for the TEM characterization. Thanks to Prof. J. Gascon and T. Wezendonk for the XPS analysis. Special thanks to S. Raaijman for his assistance with the synthesis, XRD and electrochemical characterization of double perovskites.

REFERENCES

(1) Olah, G. A.; Prakash, G. K.; Goeppert, A. *J. Am. Chem. Soc.* **2011**, *133*, 12881.

(2) Bensaid, S.; Centi, G.; Garrone, E.; Perathoner, S.; Saracco, G. *ChemSusChem* **2012**, *5*, 500.

(3) Crabtree, G. W.; Dresselhaus, M. S.; Buchanan, M. V. *Physics Today* **2004**, *57*, 39.

(4) Lewis, N. S.; Nocera, D. G. *Proceedings of the National Academy of Sciences of the United States of America* **2006**, *103*, 15729.

(5) Koper, M. T. M. *Journal of Electroanalytical Chemistry* **2011**, *660*, 254.

(6) Hayfield, P. C. S. *Platinum Metals Rev.* **1998**, *42*, 116.

(7) Schmachtel, S.; Toiminen, M.; Kontturi, K.; Forsen, O.; Barker, M. H. *J. Appl. Electrochem.* **2009**, *39*, 1835.

(8) da Silva, L. A.; Alves, V. A.; da Silva, M. A. P.; Trasatti, S.; Boodts, J. F. C. *Canadian Journal of Chemistry-Revue Canadienne De Chimie* **1997**, *75*, 1483.

(9) Depauli, C. P.; Trasatti, S. *J. Electroanal. Chem.* **1995**, *396*, 161.

(10) Trasatti, S. *Electrochim. Acta* **2000**, *45*, 2377.

(11) Hu, J. M.; Zhang, J. Q.; Cao, C. N. *Int. J. Hydrogen Energy* **2004**, *29*, 791.

(12) Matsumoto, Y.; Sato, E. *Mater. Chem. Phys.* **1986**, *14*, 397.

(13) Antolini, E. *ACS Catal.* **2014**, *4*, 1426.

(14) Oliva, P.; Leonardi, J.; Laurent, J. F.; Delmas, C.; Braconnier, J. J.; Figlarz, M.; Fievet, F.; Guibert, A. d. *J. Power Sources* **1982**, *8*, 229.

(15) Corrigan, D. A.; Bendert, R. M. *Journal of The Electrochemical Society* **1989**, *136*, 723.

(16) Suntivich, J.; May, K. J.; Gasteiger, H. A.; Goodenough, J. B.; Shao-Horn, Y. *Science* **2011**, *334*, 1383.

(17) Grimaud, A.; May, K. J.; Carlton, C. E.; Lee, Y. L.; Risch, M.; Hong, W. T.; Zhou, J.; Shao-Horn, Y. *Nat Commun* **2013**, *4*, 2439.

(18) McCrory, C. C.; Jung, S.; Peters, J. C.; Jaramillo, T. F. *Journal of the American Chemical Society* **2013**, *135*, 16977.

(19) Carmo, M.; Fritz, D. L.; Mergel, J.; Stolten, D. *International Journal of Hydrogen Energy* **2013**, *38*, 4901.

(20) Holladay, J. D.; Hu, J.; King, D. L.; Wang, Y. *Catalysis Today* **2009**, *139*, 244.

(21) Markovic, N. M.; Sarraf, S. T.; Gasteiger, H. A.; Ross, P. N. *J. Chem. Soc., Faraday Trans.* **1996**, *92*, 3719.

(22) Sheng, W.; Gasteiger, H. A.; Shao-Horn, Y. *J. Electrochem. Soc.* **2010**, *157*, B1529.

(23) Schröder, V.; Emonts, B.; Janßen, H.; Schulze, H. P. *Chemical Engineering & Technology* **2004**, *27*, 847.

(24) Zeng, K.; Zhang, D. *Prog. Energy Combust. Sci.* **2010**, *36*, 307.

(25) Hu, W.; Zhong, H.; Liang, W.; Chen, S. *ACS Applied Materials & Interfaces* **2014**, *6*, 12729.

(26) Nong, H. N.; Gan, L.; Willinger, E.; Teschner, D.; Strasser, P. *Chem. Sci.* **2014**, *5*, 2955.

(27) Howard, C. J.; Stokes, H. T. *Acta Crystallographica Section A* **2005**, *61*, 93.

(28) Howard, C. J.; Kennedy, B. J.; Woodward, P. M. *Acta Crystallographica Section B* **2003**, *59*, 463.

(29) Howard, C. J.; Stokes, H. T. *Acta Crystallographica Section B* **2004**, *60*, 674.

(30) Fu, W. T.; Ijdo, D. J. W. *J. Alloys Compd.* **2005**, *394*, L5.

(31) Fu, W. T.; Ijdo, D. J. W. *J. Solid State Chem.* **2005**, *178*, 1312.

(32) Huang, Q.; Soubeyroux, J. L.; Chmaissem, O.; Sora, I. N.; Santoro, A.; Cava, R. J.; Krajewski, J. J.; Peck Jr, W. F. *J. Solid State Chem.* **1994**, *112*, 355.

(33) Vente, J. F.; Ijdo, D. J. W. *Mater. Res. Bull.* **1991**, *26*, 1255.

(34) Zhao, Y.; Hernandez-Pagan, E. A.; Vargas-Barbosa, N. M.; Dysart, J. L.; Mallouk, T. E. *The Journal of Physical Chemistry Letters* **2011**, *2*, 402.

(35) Diaz-Morales, O.; Hersbach, T. J. P.; Hetterscheid, D. G. H.; Reek, J. N. H.; Koper, M. T. M. *J. Am. Chem. Soc.* **2014**, *136*, 10432.

(36) Suntivich, J.; Gasteiger, H. A.; Yabuuchi, N.; Shao-Horn, Y. *J. Electrochem. Soc.* **2010**, *157*, B1263.

(37) Trasatti, S.; Petrii, O. A. *Journal of Electroanalytical Chemistry* **1992**, *327*, 353.

(38) Wakeshima, M.; Harada, D.; Hinatsu, Y. *J. Mater. Chem.* **2000**, *10*, 419.

(39) Lee, Y.; Suntivich, J.; May, K. J.; Perry, E. E.; Shao-Horn, Y. *The Journal of Physical Chemistry Letters* **2012**, *3*, 399.

(40) Hu, J.-M.; Zhang, J.-Q.; Cao, C.-N. *International Journal of Hydrogen Energy* **2004**, *29*, 791.

(41) Dau, H.; Limberg, C.; Reier, T.; Risch, M.; Roggan, S.; Strasser, P. *ChemCatChem* **2010**, *2*, 724.

(42) Beznosikov, B. V.; Aleksandrov, K. S. *Crystallography Reports* **2000**, *45*, 792.

(43) Calle-Vallejo, F.; Inoglu, N. G.; Su, H.-Y.; Martinez, J. I.; Man, I. C.; Koper, M. T. M.; Kitchin, J. R.; Rossmeisl, J. *Chemical Science* **2013**, *4*, 1245.

(44) Rossmeisl, J.; Qu, Z. W.; Zhu, H.; Kroes, G. J.; Nørskov, J. K. *J. Electroanal. Chem.* **2007**, *607*, 83.

(45) Man, I. C.; Su, H.-Y.; Calle-Vallejo, F.; Hansen, H. A.; Martínez, J. I.; Inoglu, N. G.; Kitchin, J.; Jaramillo, T. F.; Nørskov, J. K.; Rossmeisl, J. *ChemCatChem* **2011**, *3*, 1159.

Summary

This thesis discusses the parameters affecting the catalysis for the electrochemical conversion of water into oxygen. The slow kinetics for the oxygen evolution reaction (OER) is one of the major bottlenecks in the solar energy-to-fuels conversion process, which reduces the efficiency for the photo-electrochemical fuels generation (artificial photosynthesis).

Most of the theoretical and experimental attempts to understand the factors affecting the kinetics for the electrochemical water oxidation to oxygen focus in the properties of the catalysts. Those research efforts concentrate on developing catalysts able to reduce the intrinsic overpotential inherent to the oxygen evolution reaction. Only few research efforts have been devoted to understand the role of the electrolyte in the water oxidation electrocatalysis, which can however strongly affect the OER activity beyond catalyst optimization. This thesis presents a (spectro)-electrochemical study of the factors affecting the kinetics of the water oxidation reaction, not only by looking at the catalysts but also by addressing the role of the electrolyte in the catalytic process. Our experimental approach combines evidence obtained by means of a wide variety of electrochemical techniques such as cyclic and linear sweep voltammetry, potentiostatic and galvanostatic experiments, all under stationary or hydrodynamic conditions. We have also combined these techniques with spectroscopic/spectrometric techniques, particularly surface enhanced Raman spectroscopy (SERS) and online electrochemical mass spectrometry (OLEMS), to respectively monitor the formation of adsorbed intermediates and volatile reaction products. Some of the experimental evidences obtained have been analyzed in the light of results obtained by density functional theory (DFT) calculations, to propose models that allow us to rationalize the reactions occurring on the electrochemical interface, and how they affect the water oxidation kinetics.

The thesis starts in chapter 2 with a joint spectroelectrochemical and computational study of the water oxidation reaction on gold electrodes in acid media. We

study the reactions taking place on the electrode surface prior to the actual oxygen evolution, to understand the role of the 3D structure of the metal oxide in the OER. The experimental and computational results allow us to propose a model for the oxygen evolution reaction on gold electrodes where the surface metal oxide is not innocent but decomposes to produce oxygen during the overall reaction. Gold is nevertheless a very poor catalyst for the oxygen evolution reaction, and therefore it is used as support for other OER catalysts studied in this thesis.

We study the effect of the electrolyte anions and pH on the OER activity of a molecular catalyst in chapter 3. To do this, we performed systematic spectroelectrochemical experiments on an iridium-N-dimethylimidazolin-2-ylidene complex adsorbed on gold electrodes. This chapter compares the water oxidation activity obtained by having the molecular catalyst in solution (by using an auxiliary oxidant), with the electrochemical activity measured on the adsorbed catalyst. This work provides benchmarking criteria that allow one to compare the OER activity on the iridium-based molecular catalyst with heterogeneous catalysts (*i.e*. metal oxides). Moreover, we present conclusive evidences that the electrolyte anions and the pH play a crucial role in the water oxidation catalyzed by the iridium complex, such that the catalytic activity of the iridium-N-dimethylimidazolin-2-ylidene complex can be enhanced 20-fold by carefully selecting the electrolyte anion and the working pH. Furthermore, the work presents *in situ* evidence that the molecular complex does not decompose to iridium oxide during the water oxidation reaction, but rather that it becomes activated by a reversible dimerization process.

The electrochemical water oxidation in alkaline media on oxide catalysts based on earth-abundant materials is revisited in chapters 4 and 5. First, in chapter 4, we provide a joint theoretical-experimental study of the electrocatalysis of the OER on nickel double hydroxides with 3d-transition metal dopants. This study demonstrates that the nature of the active site in the double hydroxides is strongly dependent on the dopant incorporated in the compound. Moreover, this work proposes guidelines that can be employed for the rational design of nickel-based water oxidation catalysts in alkaline media. We continue in chapter 5 with a spectroelectrochemical study of the role of pH on the catalytic activity of nickel

oxyhydroxide (NiOOH) towards water oxidation. This study presents evidence of a deprotonation process of the NiOOH towards a negatively charged intermediate (oxo and/or superoxo species) that strongly affects its catalytic activity towards OER. Chapter 5 shows once more that the development of good OER anodes should take into consideration the synergy of the OER catalyst with the electrolyte.

The discussion returns to the acid-based water oxidation electrocatalysis in chapter 6. We present here a new type of oxygen evolution catalyst based on iridium double perovskites. These compounds contain three times less iridium than the IrO_2 benchmarking catalyst but exhibit a more than 3-fold higher catalytic activity, which makes them the most active catalysts for OER in acid media reported to date. The study shows that the 3D arrangement of corner-shared octahedra is a necessary prerequisite for the catalytic activity enhancement of the iridium-based double perovskites and for their chemical stability under anodic working conditions. Our findings regarding the effect of the *A* and *B*-site cations on the catalysis towards water splitting of the iridium based double perovskite suggest that the activity of these compounds might be further improved by carefully selecting the cations at those sites. Our strategy may also be extended to enhance the catalytic activity and chemical stability of ruthenium-containing compounds, with lower content of ruthenium compared with RuO_2.

In summary, this thesis shows that to enhance the kinetics for the oxygen evolution reaction, one should not only look at the catalysts but also consider the synergy between catalyst and electrolyte. A more general approach that considers the electrochemical interface as a whole (electrode + electrolyte) is therefore the most promising route towards optimal activity.

Samenvatting

Dit proefschrift beschrijft de katalytische eigenschappen die van invloed zijn op de elektrochemische conversie van water tot zuurstof. Eén van de grootste problemen met de omzetting van zonne-energie tot brandstof is de langzame kinetiek van de zuurstof evolutie reactie (OER). Dit zorgt voor een lager rendement tijdens de foto-elektrochemische productie van brandstoffen en maakt daarmee dit proces minder aantrekkelijk voor grootschalige energieopslag.

Voor het merendeel van zowel het theoretisch als experimenteel onderzoek naar de factoren van invloed op de kinetiek van elektrochemische oxidatie van water tot zuurstof ligt de focus op de eigenschappen van de katalysator. Zij concentreren zich vooral op het maken van katalysatoren die de benodigde overpotentiaal voor de OER kunnen verlagen. Weinig onderzoekers richten zich op het begrijpen van de rol die het elektrolyt speelt tijdens de katalytische oxidatie van water, terwijl dit een prominent effect kan hebben op de activiteit voor de zuurstof evolutie reactie en net een stap verder gaat dan katalysator optimalisatie. Met deze reden presenteert dit proefschrift een (spectroscopisch-) elektrochemisch onderzoek naar de factoren van invloed op de kinetiek van de wateroxidatiereactie, waarbij we niet alleen de katalysator maar ook de rol van het elektrolyt in het katalytisch proces bekijken. Onze experimentele aanpak combineert bewijs dat is verkregen met uiteenlopende elektrochemische technieken als lineaire sweep en cyclische voltammetrie, potentiostatische en galvanostatische experimenten, waarbij altijd stationaire of hydrodynamische omstandigheden van toepassing waren. Ook hebben we deze technieken gecombineerd met spectroscopische en spectrometrische technieken, voornamelijk oppervlak-versterkte Raman spectroscopie (SERS) en online elektrochemische massaspectrometrie (OLEMS), om respectievelijk de vorming van intermediairen en vluchtige reactieproducten te volgen. We hebben experimentele resultaten gecombineerd met theoretische resultaten verkregen met density functional theory (DFT) berekeningen, om te kunnen modelleren welke reacties er aan het oppervlak plaatsvinden, en hoe deze van invloed zijn op de kinetiek van wateroxidatie.

Het proefscrift begint in hoofdstuk 2, waar we wateroxidatie aan een goud oppervlak onder zure omstandigheden onderzoeken middels spectroscopisch-elektrochemische technieken en theoretische berekeningen. We bekijken welke reacties er plaatsvinden aan het elektrodeoppervlak voordat wateroxidatie begint, om te begrijpen welke rol de 3D structuur van het metaaloxide speelt tijdens OER. De experimentele en theoretische resultaten stellen ons in staat een model op te stellen voor de zuurstof evolutie reactie aan goud elektrodes, waarbij de metaaloxides aan het oppervlak ontbinden en zuurstof vrijgeven tijdens de reactie. Desalniettemin is goud een slechte katalysator voor de zuurstof evolutie reactie, en daarom is het gebruikt als drager voor de andere katalysatoren die zijn onderzocht in dit proefschrift.

Wat voor effect de anionen in, en de zuurgraad van, het elektrolyt hebben op de activiteit van een moleculaire katalysator voor wateroxidatie komt aan bod in hoofdstuk 3. Om dit te onderzoeken hebben we spectroscopisch-electrochemische experimenten gedaan tijdens zuurstofevolutie aan een iridium-N-dimethylimidazool-2-ylideen complex, dat geadsorbeerd is op een goud elektrode. Dit hoofdstuk vergelijkt de activiteit voor water oxidatie van het moleculaire complex in oplossing (met behulp van een additionele oxidant) met de activiteit van het complex als het geadsorbeerd is aan een goudoppervlak. We beschrijven criteria die gebruikt kunnen worden om de activiteit voor zuurstof evolutie van het iridium-gebaseerde moleculaire katalysator te vergelijken met heterogene katalysatoren (metaaloxides). Verder tonen we aan dat de zuurgraad van, en de anionen in, het elektrolyt een cruciale rol spelen tijdens de zuurstof evolutie reactie aan iridium-N-dimethylimidazool-2-ylideen complexen, en dat een optimalisatie van deze parameters de activiteit met een factor twintig kan verhogen. Ook wordt er *in-situ* bewijs geleverd dat het complex niet ontbindt tot iridium oxide tijdens wateroxidatie, maar dat het geactiveerd wordt door een reversibel dimerisatieproces.

De elektrochemische oxidatie van water aan oxidische katalysatoren gebaseerd op veelvoorkomende materialen komt aan bod in hoofdstukken 4 en 5. In hoofdstuk 4 beschrijven we onderzoek dat zowel experimenteel als theoretisch van aard is, waarbij er gekeken is naar de elektrokatalyse voor de zuurstof evolutie reactie aan nikkel dubbel

hydroxides van 3d overgangsmetalen. Hier laten we zien dat het doteren van het nickel oxyhydroxide een groot effect heeft op de aard van de katalytisch actieve sites. Verder stellen we een aantal richtlijnen voor die gebruikt kunnen worden om rationeel katalysatoren te ontwerpen gebaseerd op nikkel voor gebruik in basische omstandigheden. In hoofdstuk 5 gaan we verder met een spectroscopisch-electrochemisch onderzoek naar de rol van de zuurgraad op de katalytische activiteit van nikkel oxyhydroxide (NiOOH) voor de oxidatie van water. Hierin geven we bewijs dat een negatief geladen oxidisch intermediair aan het oppervlak wordt gevormd door deprotonering, een proces dat een grote invloed heeft op de katalytische activiteit voor OER. Ook hoofdstuk 5 laat zien dat je tijdens het ontwerpen van een goede anode voor de zuurstof evolutie reactie niet alleen moet kijken naar de katalysator maar ook naar het elektrolyt, en de onderlinge interactie tussen de twee.

In hoofdstuk 6 keren we terug naar de elektrokatalyse van de zuurstof evolutie reactie onder zure omstandigheden. Hier beschrijven we een nieuw type katalysator, gebaseerd op iridium in een dubbel perovskiet, voor de zuurstof evolutie reactie. Deze katalysatoren bevatten drie maal zo weinig iridium als IrO_2, welke tevens de benchmark is voor zuurstofevolutie. Het feit dat deze nieuwe katalysatoren verder een minimaal factor 3 hogere activiteit vertonen voor OER dan iridium oxide, maakt ze de meest actieve verbinding ooit gerapporteerd in zuur milieu. We laten zien dat een 3D arrangement van hoek-gedeelde octaëders nodig is voor de verhoogde katalytische activiteit voor water oxidatie door deze iridium gebaseerde dubbel perovskieten, en ook voor hun chemische stabiliteit onder typische anodische omstandigheden. Onze bevindingen aangaande het effect van de kationen op de A en B plek op de activiteit voor watersplitsing suggereren dat de activiteit van deze iridium dubbel perovskieten verder zou kunnen worden verbeterd door deze kationen zorgvuldig te selecteren. Onze strategie zou ook kunnen worden gebruikt voor ruthenium gebaseerde stoffen, om de katalytische activiteit en chemische stabiliteit te verhogen, en tegelijk de hoeveelheid ruthenium ten opzichte van RuO_2 te verminderen.

Uit dit proefschrift blijkt dat, om de kinetiek van de zuurstof evolutie reactie te verbeteren, niet alleen naar de katalysator gekeken moet worden maar ook de synergie tussen katalysator en elektrolyt in acht genomen moet worden. Een meer generieke aanpak, waarbij het elektrochemische grensvlak als één geheel (elektrode + elektrolyt) beschouwt wordt lijkt daarmee een veelbelovende route voor het ontwerpen van een optimale katalysator.

List of publications

- O. Diaz-Morales, I. Ledezma-Yanez, M.T.M. Koper and F. Calle-Vallejo, "Guidelines for the rational design of Ni-based double hydroxide electrocatalysts for the oxygen evolution reaction", *ACS Catal.* 2015, 5, 5380-5387

- I. Ledezma-Yanez, O. Diaz-Morales, M. Figueiredo, M.T.M. Koper, "Hydrogen Oxidation and Hydrogen Evolution on a Platinum Electrode in Acetonitrile", *ChemElectroChem* 2015, DOI: 10.1002/celc.201500341.

- J. Shen, R. Kortlever, R. Kas, Y. Birdja, O. Diaz-Morales, Y. Kwon, I. Ledezma-Yanez, K. J. P. Schouten, G. Mul and M.T.M. Koper, "Electrocatalytic reduction of carbon dioxide to carbon monoxide and methane at an immobilized cobalt protoporphyrin in aqueous solution", *Nat. Comm.* 2015, 6, 8177.

- F. Calle-Vallejo, O. Diaz-Morales, M. Kolb and M.T.M. Koper, "Why Is Bulk Thermochemistry a Good Descriptor for the Electrocatalytic Activity of Transition Metal Oxides?", *ACS Catal.* 2015, 5, 869-873.

- O. Diaz-Morales, T.J.P. Hersbach, D.G.H. Hetterscheid, J.N.H. Reek and M.T.M. Koper, "Electrochemical and Spectroelectrochemical Characterization of an Iridium-Based Molecular Catalyst for Water Splitting: Turnover Frequencies, Stability, and Electrolyte Effects", *J. Am. Chem. Soc.* 2014, 136, 10432-10439.

- O. Diaz-Morales, F. Calle-Vallejo, C. de Munck and M.T.M. Koper, "Electrochemical water splitting by gold: evidence for an oxide decomposition mechanism", *Chem. Sci.*, 2013, 4, 2334-2343. (**Front cover of Issue)**

- O. Diaz-Morales, J. Mostany, C. Borrás, B.R. Scharifker, “Current transient study of the kinetics of nucleation and diffusion-controlled growth of bimetallic phases”, *J. Solid State Electrochem.* 2013, 17, 345-351.

Curriculum Vitae

Oscar was born in Caracas, Venezuela on the 26th of September 1984. After high school, he studied Chemistry at Simón Bolívar University (USB), and finished his bachelor in 2008 with a research thesis on "Heavy metal detection by anodic stripping voltammetry in closed loop flow systems". He continued at USB for his master's degree in Chemistry under the supervision of Prof. Dr. Benjamin Scharifker, studying the electrodeposition of bimetallic alloys; the topic of his master research was "Electrochemical bimetallic phase formation". In 2009, he did an internship at the Institute of Physical Chemistry "Rocasolano" under the supervision of Dr. Angel Cuesta, studying the alloy formation process during the underpotential metal deposition by means of potential-modulated ultraviolet spectroscopy; the internship was funded by a fellowship awarded by the Venezuelan Research Council. He obtained his master's degree (with honors) in 2011.

In June 2011, Oscar started his PhD work in Leiden University (the Netherlands) under the supervision of Prof. Dr. Marc T. M. Koper with the project title of "Catalysis of the electrochemical water oxidation to oxygen" sponsored by the BioSolar Cell open innovation consortium, to understand the parameters affecting the electrochemical oxygen evolution reaction. The results of this work are presented in this thesis; parts of his work have been presented at several international conferences.

Appendix A: Supplementary Material for Chapter 2

Evidences for Gold Oxide Decomposition Mechanism during the Electrochemical Water Oxidation

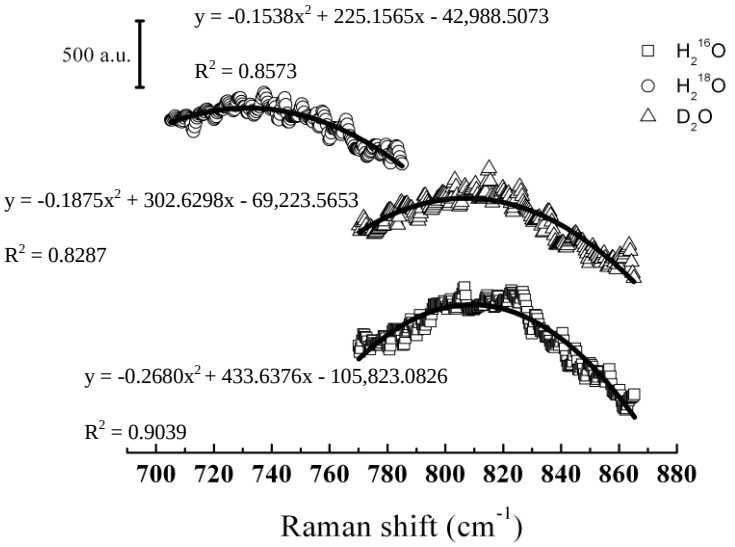

Figure A1. Raman spectrum acquired at 1.7 V vs. RHE in a pH=0 solution prepared with $H_2{}^{16}O$, $H_2{}^{18}O$ and D_2O, showing the polynomial fittings (second grade polynomial) used to determine the peak position.

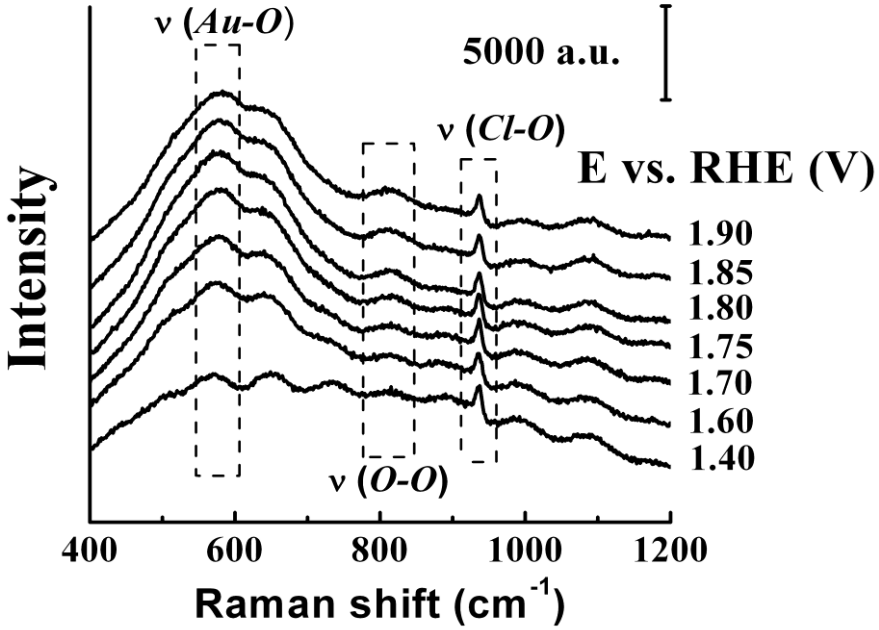

Figure A2. SERS spectra for oxygen evolution acquired at constant potential in pH=0 solution prepared in D_2O.

Appendix B: Supplementary Material for Chapter 3

Electrochemical and Spectroelectrochemical Characterization of an Iridium-based Molecular Catalyst for Oxygen evolution: Turnover Frequencies, Stability and Electrolyte Effects

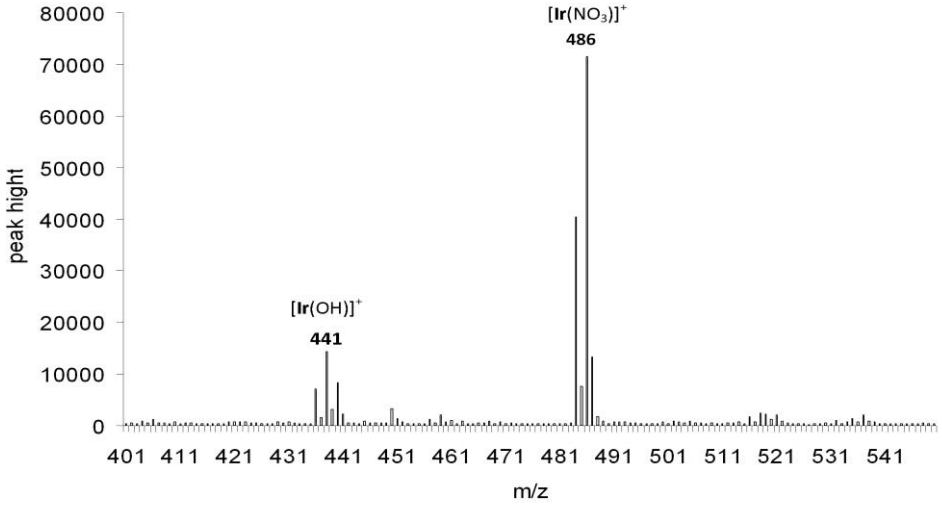

Figure B1. ESI-MS spectrum of $Ir(OH)_2$ at pH 1 when acidified with HNO_3. An identical ESI-MS spectrum is obtained upon dissolving $[Ir(NO_3)_2]$ in water.

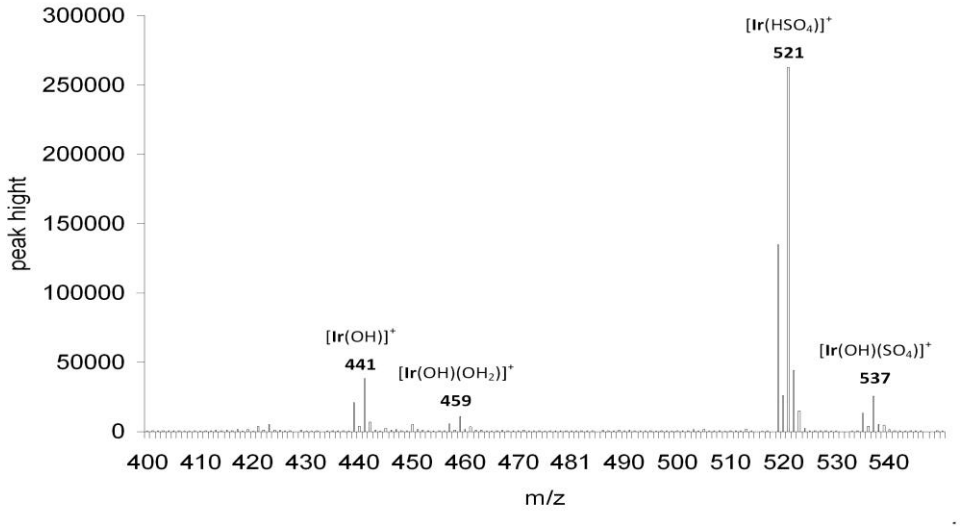

Figure B2. ESI-MS spectrum of $Ir(OH)_2$ at pH 1 when acidified with H_2SO_4.

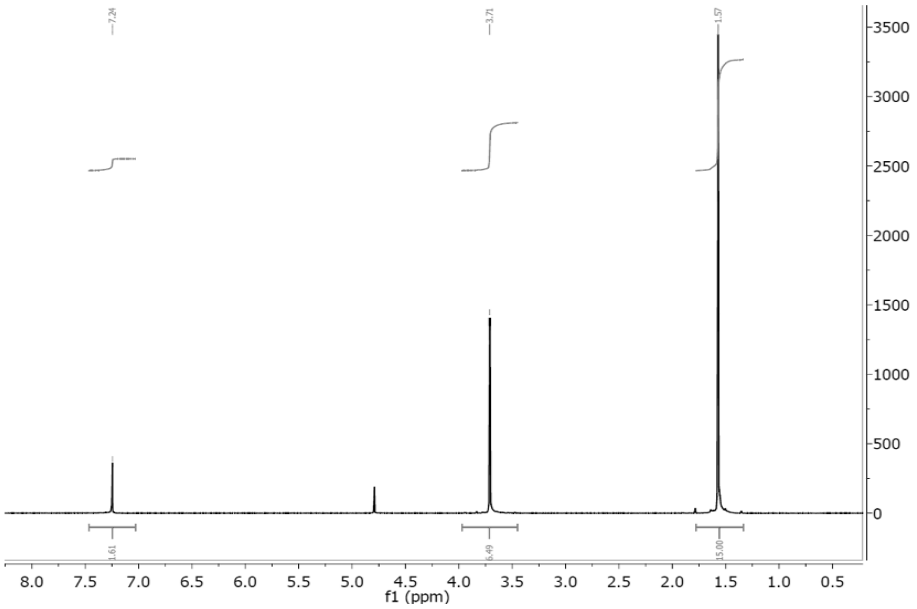

Figure B3. ^{1}H NRM spectrum of iridium-N-dimethylimidazolin-2-ylidene in D_2O at pH 1.

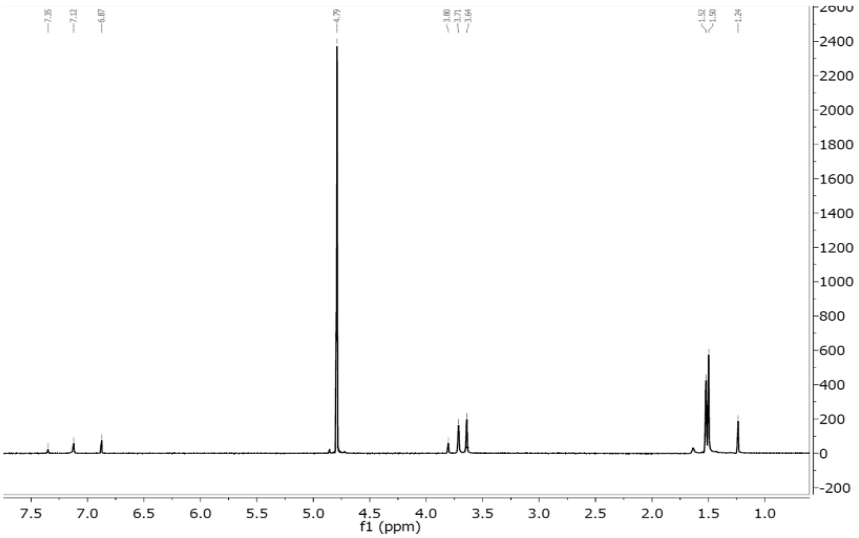

Figure B4. ^{1}H NRM spectrum of iridium-N-dimethylimidazolin-2-ylidene in D_2O at pH 7.

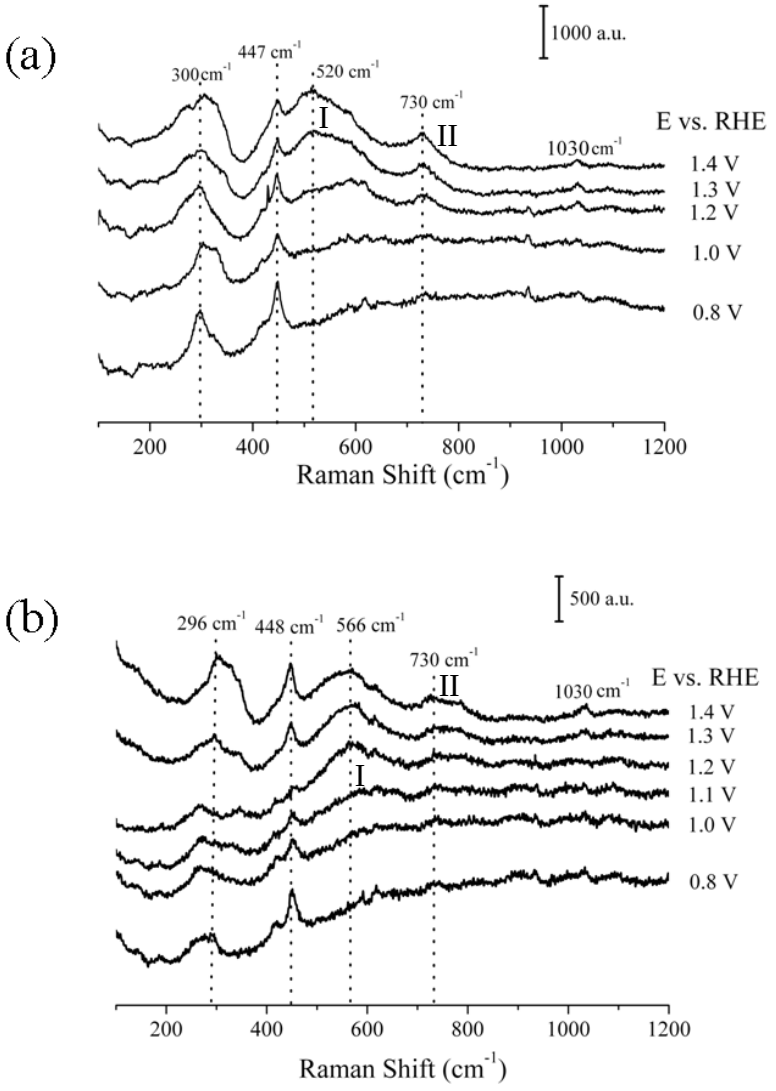

Figure B5. SERS spectra of the Ir-based molecular catalyst drop casted on gold, acquired in potentiostatic conditions in 0.1 M $HClO_4$: (a measured in ^{18}O water, (b measured in D_2O.

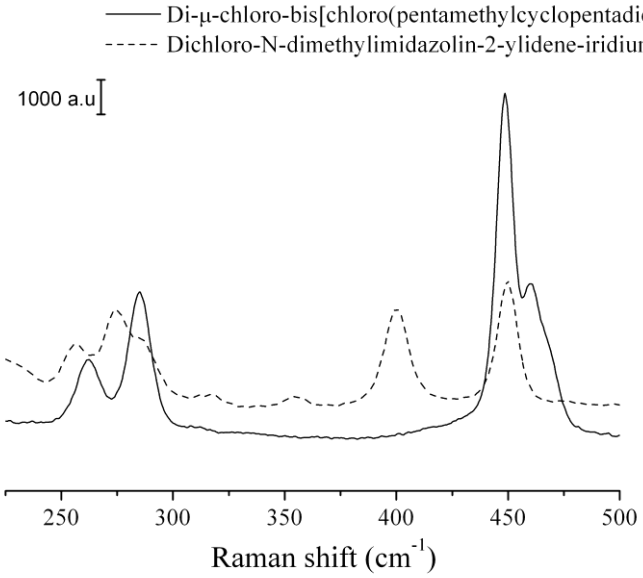

Figure B6. Spectra for Di-μ-chloro-bis[chloro(pentamethylcyclopentadienyl)iridium(III)], and Di-chloro-N-dimethylimidazolin-2-ylidene-penthamethylcyclopentanienyl)iridium(III) acquired in normal Raman mode

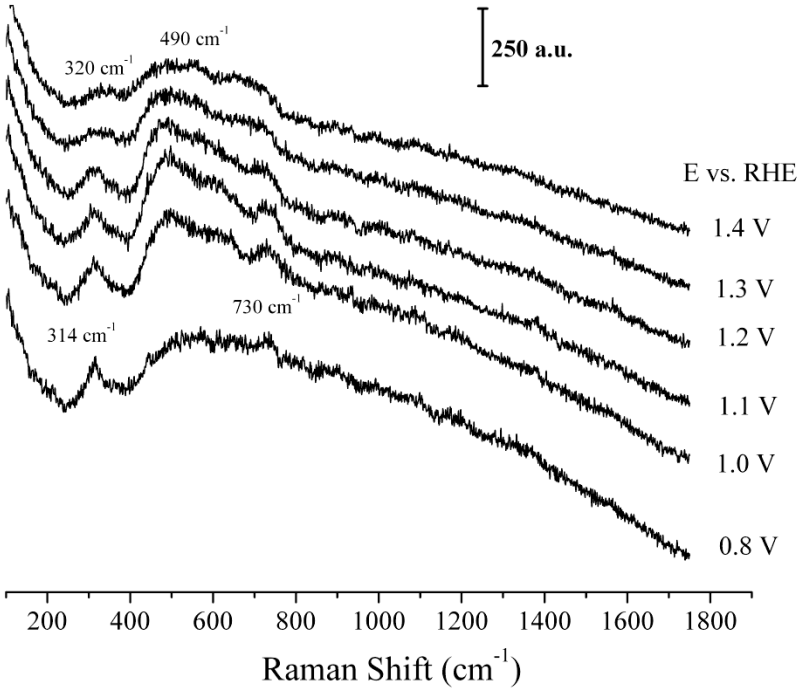

Figure B7. SERS spectra of iridium oxide nanoparticles drop-casted on gold, acquired under potentiostatic conditions in 0.1 M $HClO_4$

Table B1. Position and error of the Raman the peak I and II (see Figure 5 in discussion) in the three media studied and ratio between the position of the peaks in $^{18}OH_2$ and D_2O *versus* $^{16}OH_2$. Average obtained out of three different measurements.

	Peak I position (cm^{-1})	**Peak II position (cm^{-1})**	**Ratio $^{18}O/^{16}O$ and D/H**
$^{16}OH_2$	564 $\pm$ 8	733 $\pm$ 7	----------
$^{18}OH_2$	537 $\pm$ 5	725 $\pm$ 5	0.95
$^{16}OD_2$	565 $\pm$ 4	732 $\pm$ 6	1.00

Appendix C: Supplementary Material for Chapter 4

Guidelines for the Rational Design of Nickel-based Double Hydroxide Electrocatalysts for the Oxygen Evolution Reaction

X-Ray Diffraction data

The XRDs were analyzed with X'Pert HighScore 2.0.1. The pattern for the product of thermal decomposition of NiFe DH fits well with the pattern number 00-044-1485 corresponding to $NiFe_2O_4$, see Figure C1. The XRD of pristine NiFe DH shows a compound of low crystallinity and the phase analysis was not possible. However, the segregation of $Ni(OH)_2$ was discarded upon comparison with the XRD of the double hydroxide with the pattern of $Ni(OH)_2$, as shown in Figure C2. Thus, there are no significant evidences of pure $Ni(OH)_2$ formation.

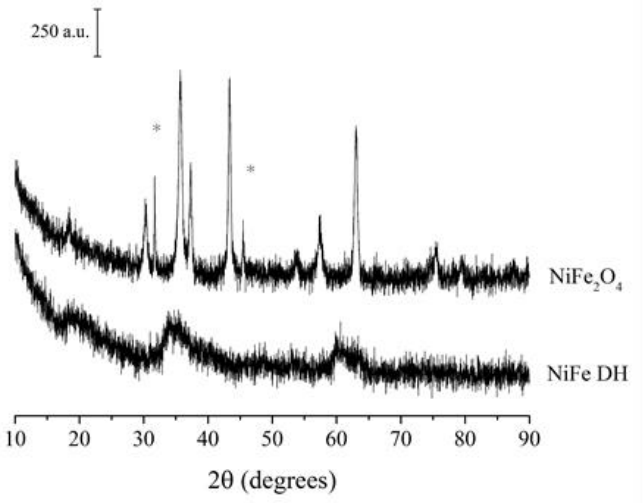

Figure C1. Powder XRD of the (as prepared) NiFe DH and $NiFe_2O_4$ (product of thermal decomposition of the DH at 600 °C). The stars mark the peaks belonging to a second, unknown phase formed in small amounts during the thermal decomposition of NiFe DH.

The analysis of the XRD of NiMn DH with X'Pert HighScore 2.0.1 confirmed that manganese precipitated as manganese carbonate. The XRD of the double hydroxide fits well with the pattern number 00-007-0268 of $MnCO_3$ (the peaks corresponding to this phase are marked with orange stars in Figure C3).

The XRD of the NiCo DH indicates the formation of a separate phase of pure $Ni(OH)_2$ (the peaks corresponding to this phase are marked with black stars in Figure C2).

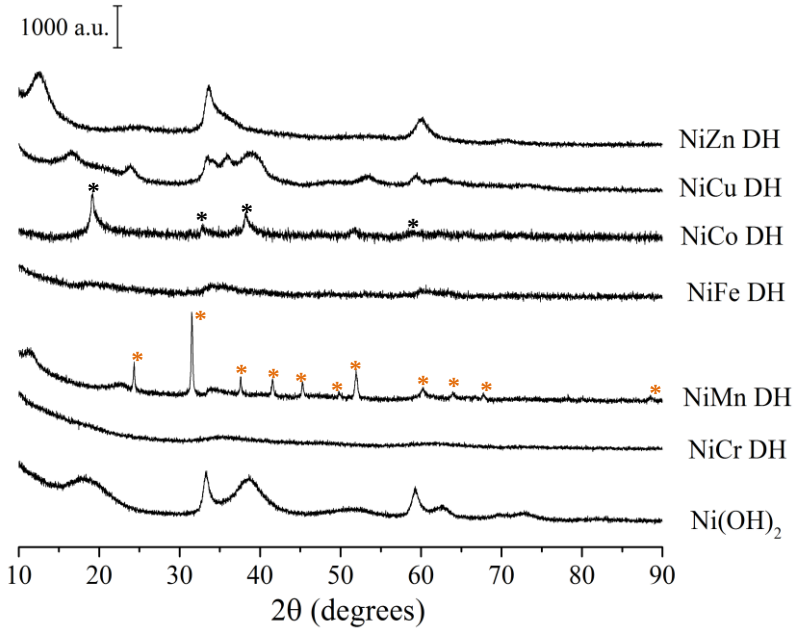

Figure C2. Powder XRDs of the Ni-based DHs with various transition metals. The XRD pattern of $Ni(OH)_2$ is also presented for comparison. The black stars indicate the peaks corresponding to pure $Ni(OH)_2$ in NiCo DH, while the orange stars indicate the peaks corresponding to $MnCO_3$ in NiMn DH.

Effect of Fe doping on the catalytic activity of NiFe DH

NiFe DH with Fe content in the range 25-75% was synthesized to assess doping effects in the catalytic activity. Figure C3 summarizes the results obtained for this experiment, in which it is clear that the highest catalytic activity is reached for 50 % Fe doping.

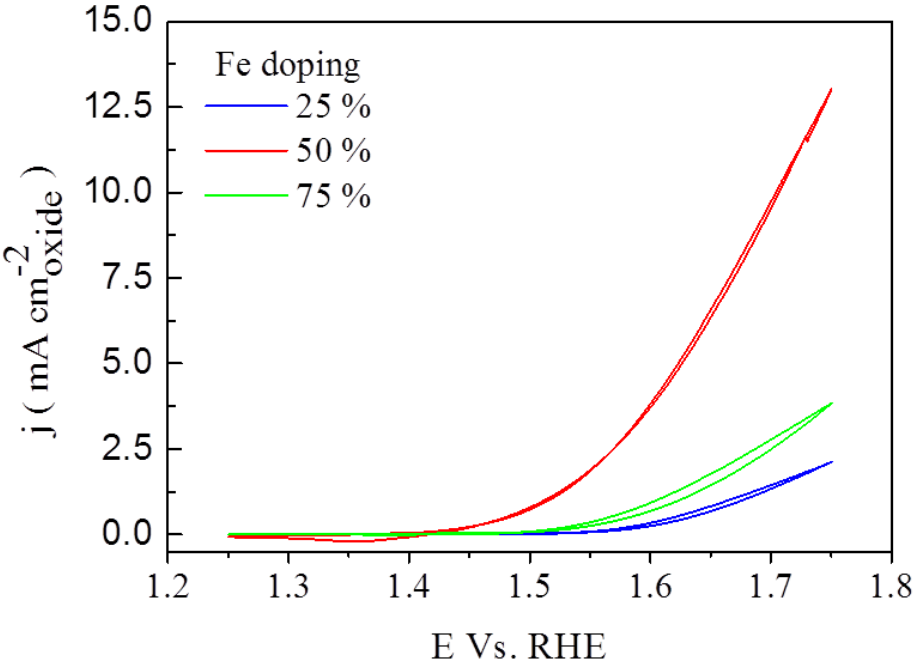

Figure C3. Cyclic voltammetry for oxygen evolution in 0.1 M KOH for NiFe DH with different percentages of Fe doping. The NiFe DH was immobilized on Au. The experiments were performed under hydrodynamic conditions (rotation rate: 1500 RPM, scan rate: 0.01 V s^{-1}).

Infrared data

Figure C4 shows the infrared spectra for the different DHs. The first band (depicted in red) corresponds to the ν_2-CO_3^{2-} symmetric vibration,[1-3] and appears to be larger for the NiMn

DH. The next band at *ca.* 1080 cm^{-1} (in blue), shows the ν_1 symmetric vibration from carbonate ion, which suggests a degeneration in the symmetry of the carbonate ion from D_{3h} a C_{2v}.[1,2,4] The green band around 1390 cm^{-1} corresponds to the ν_1-CO_3^{2-} anti-symmetric vibration,[5] present in all samples, but appears broaden for the NiMn DH, confirming the presence of superficial and interstitial $MnCO_3$. We also observe the ν_3-CO_3^{2-} symmetric band at *ca.* 1530 cm^{-1} (purple line) as well as the δ-HOH around 1664 cm^{-1} (brown line).[1-4,6] The former band indicates the presence of water in the first coordination sphere of the DHs. Meanwhile, NiMn and NiCo show a band around 3380 cm^{-1} (in orange), corresponding to "free" water,[5] and it is an indicative for the presence of $Mn(H_2O)_x$ and $Co(H_2O)_x$ complexes and simple out-of-coordination-sphere hydration. The hydration water coordinated to the Ni is depicted in olive,[3,6] and appears at 3625 cm^{-1}.

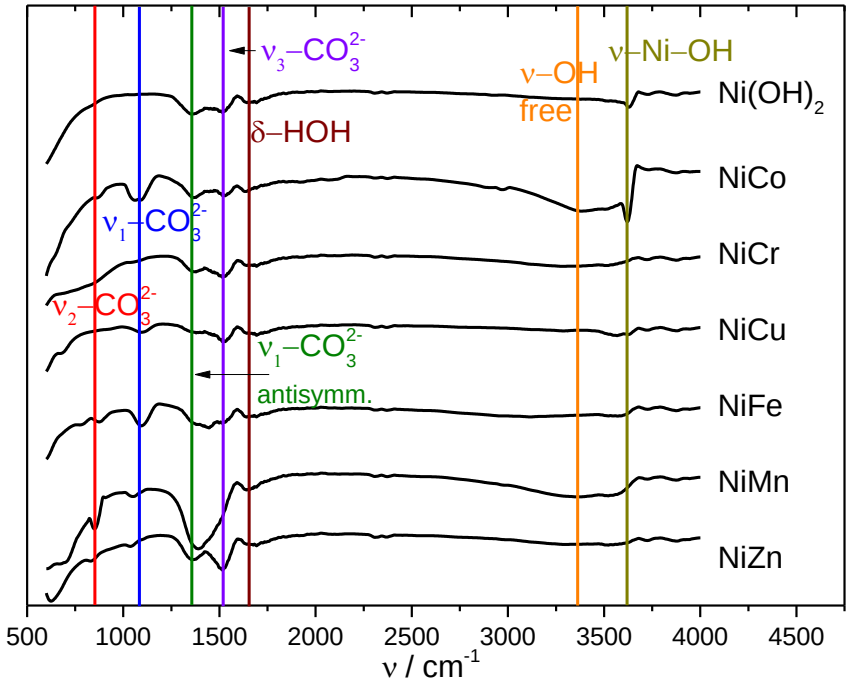

Figure C4. Infrared spectra for the Ni-based DHs with transition metals. The spectra are presented with the respective frequency assignment of the characteristic bands.

(1) Frost, R. L.; Ding, Z.; Martens, W. N.; Johnson, T. E.; Kloprogge, J. T. *Spectrochimica Acta Part A: Molecular and Biomolecular Spectroscopy* **2003**, *59*, 321.

(2) Frost, R. L.; Martens, W.; Ding, Z.; Kloprogge, J. T.; Johnson, T. E. *Spectrochimica Acta Part A: Molecular and Biomolecular Spectroscopy* **2003**, *59*, 291.

(3) Kloprogge, J. T.; Frost, R. L. *J. Solid State Chem.* **1999**, *146*, 506.

(4) Cocheci, L.; Barvinschi, P.; Pode, R.; Popovici, E.; Seftel, E. M. *Chem. Bull. "POLITEHNICA" Univ. (Timisoara)* **2010**, *55*, 40.

(5) Lambert, J. B. *Introduction to organic spectroscopy*; Macmillan: New York, 1987.

(6) Frost, R. L.; Weier, M. L.; Clissold, M. E.; Williams, P. A. *Spectrochimica Acta Part A: Molecular and Biomolecular Spectroscopy* **2003**, *59*, 3313.

Effect of the precipitating agent of NiCr, NiMn and NiFe DHs on their catalytic activity towards OER

The effect of the precipitating agent used in the synthesis of NiCr, NiMn and NiFe DHs on their OER activity was assessed by replacing the sodium carbonate used in the synthesis for a solution 2 M NaOH, following the co-precipitation procedure described in section 4.2.4 of this work. Figure C5 compares the OER activity of the three nickel-based double hydroxide. It is clear from the plot that the precipitation with sodium carbonate (at constant pH) generates catalysts with higher OER activity than the procedure performed with sodium hydroxide.

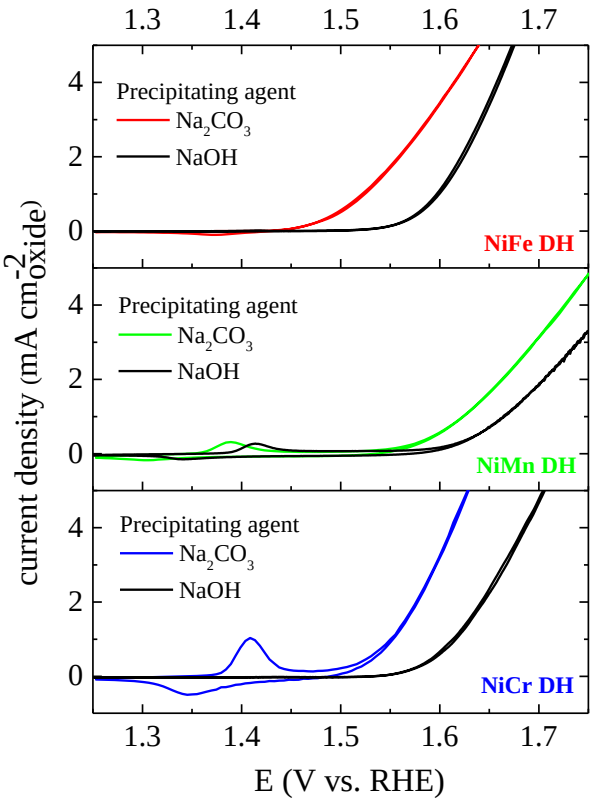

Figure C5. Effect of the precipitating agent during the synthesis of NiCr, NiMn and NiFe DHs on their catalytic activity towards the oxygen evolution reaction in 0.1 M KOH. The experiments were performed under hydrodynamic conditions (rotation rate: 1500 RPM, scan rate: 0.01 V s^{-1}).

Catalytic activity towards OER of NiFe DH in comparison with the IrO_2

The catalytic activity of the NiFe DH towards electrochemical water oxidation in alkaline media was compared with the activity measured on IrO_2, reported as benchmark for the oxygen evolution reaction.[1,2] IrO_2 deposition was performed as reported in literature.[3] Figure C6 summarizes the results of these measurements, it is clear that NiFe DH reported in this work shows higher intrinsic catalytic activity (expressed as current density) towards oxygen evolution when it is compared with the benchmark IrO_2 catalyst.

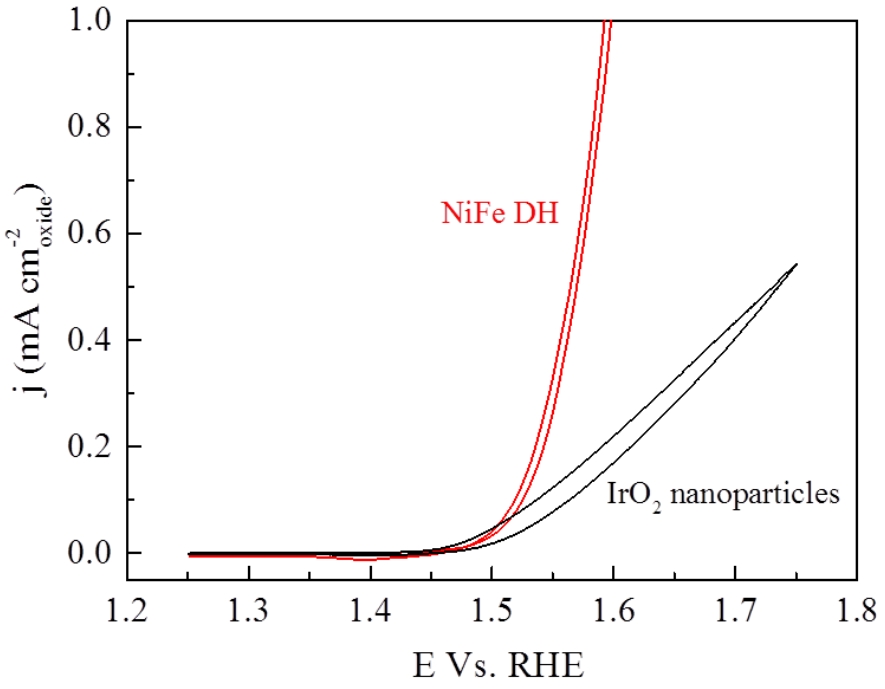

Figure C6. Polarization curve for the oxygen evolution reaction in 0.1 M KOH for NiFe DH and IrO_2 nanoparticles immobilized on Au. The experiments were performed under hydrodynamic conditions (rotation rate: 1500 RPM, scan rate: 0.01 V s^{-1}).

Stability of NiFe DHs under anodic conditions

The stability of the NiFe DH electrocatalyst was assessed by galvanostatic electrolysis, using the approach reported by McCrory *et al.*[2] Figure C7a shows the evolution of the overpotential during an electrolysis carried out by applying a current density of 10 mA cm_{disk}^{-2} for 2 h. The overpotential at the beginning of the electrolysis is plotted versus the value measured after 2 h, and the results are shown in Figure C7b. The results reported by McCrory *et al.*[2] for the electrochemical water oxidation in NaOH 1 M on IrO_x, $NiFeO_x$ and NiO are presented for comparison. Note that the diagonal dashed line in Figure C7b represents the expected response of a stable catalyst. The results in Figure C7.a clearly show that NiFe DH is stable under anodic conditions, has activities comparable to those of $NiFeO_x$ catalysts and is more stable than IrO_x.

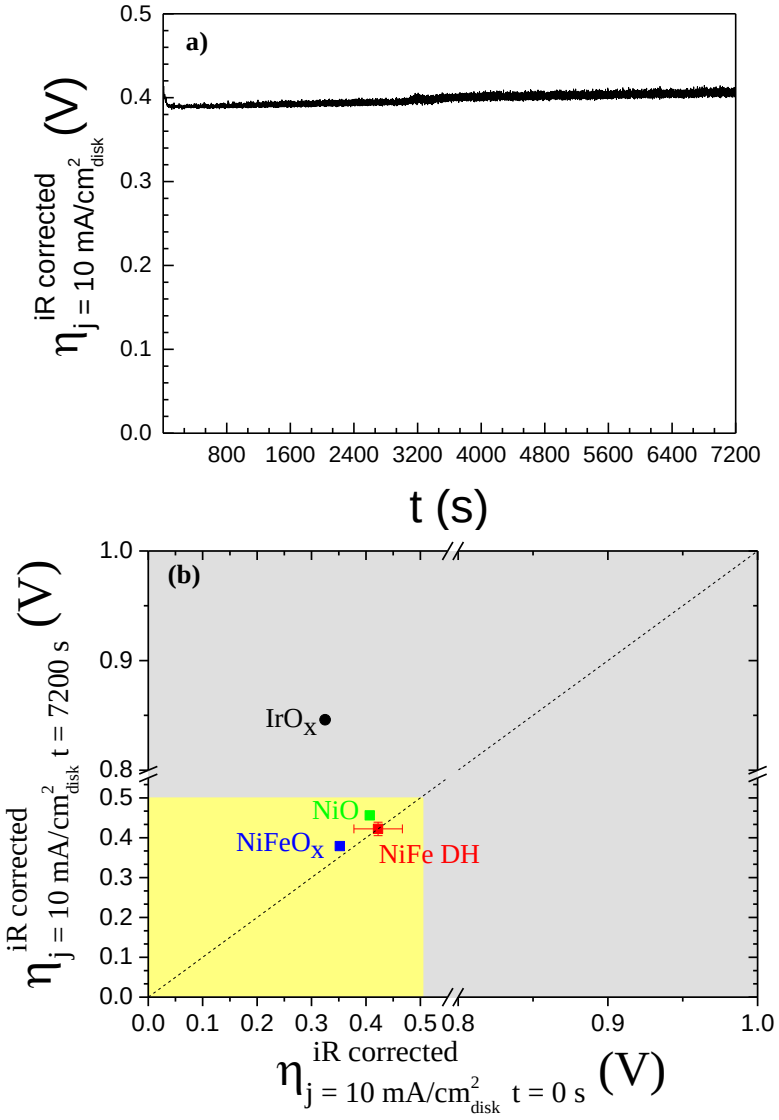

Figure C7. Stability of NiFe DH assessed by galvanostatic electrolysis. a) Evolution of the overpotential towards electrochemical water oxidation in KOH 0.1 M on NiFe DH, measured by applying a constant current density of 10 mA cm_{disk}^{-2} during 2 h in hydrodynamic conditions (rotation rate: 1500 RPM). b) Overpotential at the end of the galvanostatic electrolysis towards electrochemical water oxidation on NiFe DH obtained from Figure C7a as a function of the initial overpotential. Additional points for IrO_x, NiO and $NiFeO_x$ are provided for comparison, and correspond to a galvanostatic experiment performed in NaOH 1M, taken from McCrory *et al.*[2]

Estimation of the Faradaic efficiency

The experiments were performed in rotating ring-disk electrode (RRDE) configuration. The Pt-ring electrode was set at 0.45 V vs. RHE so that the O_2 produced in the disk during the anodic scans was reduced, via 4 electrons to OH^-, according the equation C1[4]:

$$O_2 + 2H_2O + 4e^- \rightarrow 4OH^- \quad \text{(C1)}$$

The faradaic efficiency (ε%) was calculated using the expression for the collection efficiency of the RRDE[5] given in Equation C2:

$$\varepsilon(\%) = \frac{i_{ring}}{N \cdot i_{disk}} \times 100 \quad \text{(C2)}$$

The collection efficiency (N) for the RRDE setup was calculated for the water oxidation reaction, using IrO_2 deposited on the Au-disk as electrocatalyst[2] and the number obtained was 0.20 ± 0.01, which is in close agreement with the collection factor obtained from the experiments with $Fe(CN)_6^{3-}$/ $Fe(CN)_6^{4-}$ (N=0.23). The small difference between N calculated from water oxidation/oxygen reduction and the $Fe(CN)_6^{3-}$/ $Fe(CN)_6^{4-}$ is attributed to the non-ideal outward flow of O_2.[1]

Estimation of the adsorption energies

The adsorption energies of *O, *OH and *OOH, namely ΔG_O, ΔG_{OH} and ΔG_{OOH}, correspond to the reaction energies of the following reactions:

$$* + H_2O \rightarrow {}^*O + 2(H^+ + e^-)$$
$$* + H_2O \rightarrow {}^*OH + 2(H^+ + e^-)$$
$$* + 2H_2O \rightarrow {}^*OOH + 2(H^+ + e^-)$$

Where * is a free adsorption site at the surface. The left leg of the volcanoes in Figures 2 and 3 are calculated as: $\Delta G_{LEFT} = \Delta G_{OOH} - \Delta G_{O}$. The right leg of the volcanoes in Figures 2 and 3 are calculated as: $\Delta G_{RIGHT} = \Delta G_{O} - \Delta G_{OH}$.

We note that in the case of the oxygen reduction reaction (ORR), namely the reaction opposite to the OER, solvation is essential to estimate accurate adsorption energies and the corrections for *OH and *OOH are on the order of ~0.5 eV[6]. However, Norskov and coworkers have shown that solvation decreases as the electrode potential raises[7]. Among the reasons for the loss of solvation, we remark the formation of surface oxides, which disturb the formation of the long-ranged ice-like water layers over the surface within which adsorbates such as *OH and *OOH are fully solvated. This is why the modelling of the OER does not normally incorporate solvation corrections (see Man et al.[8]). Furthermore, earlier this year, Siahrostami and Vojvodic inspected the effects of solvation on the predicted OER overpotentials of various rutile oxides[9]. Note that they used exactly the same kind of volcano plots and exchange-correlation functional (RPBE) as in our study and concluded that "the OER activity trend is preserved in the presence of a water network". They also find that oxides near the top of the volcano possess solvation energies the addition of which modifies the OER overpotentials by ~0.05 V only. We conclude that solvation is typically not included in the OER modelling and that its addition does not alter the overall conclusions of Sabatier-type activity plots. Additionally, we would like to mention that we have considered a full coverage of adsorbed intermediates for the double hydroxides in this study (see Figure 1 in the main text and Figure C7 below). Thus, there exist hydrogen bonds between co-adsorbed oxygenates (*OH with other vicinal *OH and *OOH species) which are accounted for in the adsorption energy trends without any need for external corrections.

The volcano plots in Figures 3a and b in the main text correspond to a full-coverage regime in which different species populate the active sites as follows:

i) In Figure 3a, that is when the activity of Ni sites is evaluated, the M site was covered with *O for M = Cr, Mn, Fe, Co, and the M site was covered with *OH for M = Ni, Cu, Zn.

ii) In Figure 3b, that is when the activity of M sites is assessed, Ni sites are covered with *OH.

These different configurations are provided in Figure C7.

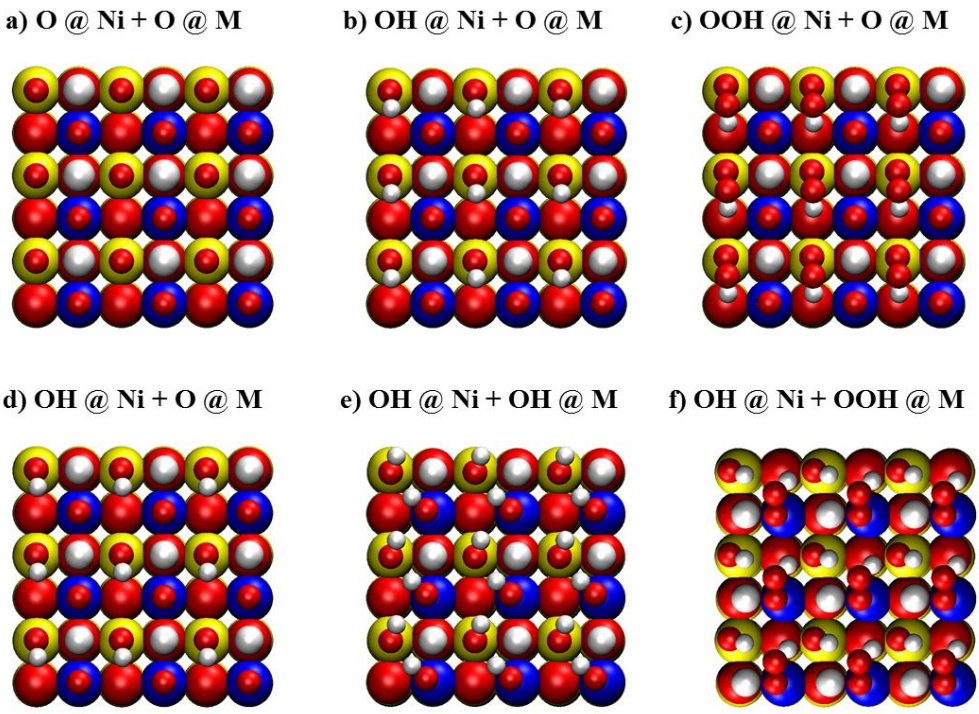

Figure C7. High coverage of OER adsorbates on model NiMOOH catalysts. When the activity of Ni sites is evaluated (Figure 3a), the adsorption energies of a) *O, b) *OH and c) *OOH are calculated while the M site is covered with *O for M = Cr, Mn, Fe, Co. When M = Ni, Cu, Zn, the M site is covered with *OH, analogous to d)-f). When the activity of M sites is assessed (Figure 3b), the adsorption energies of c) *O, d) *OH, and e) *OOH are calculated while Ni sites are covered with *OH.

REFERENCES

(1) Lee, Y.; Suntivich, J.; May, K. J.; Perry, E. E.; Shao-Horn, Y. *J. Phys. Chem. Lett.* **2012**, *3*, 399.

(2) McCrory, C. C.; Jung, S.; Peters, J. C.; Jaramillo, T. F. *J. Am. Chem. Soc.* **2013**, *135*, 16977.

(3) Zhao, Y.; Hernandez-Pagan, E. A.; Vargas-Barbosa, N. M.; Dysart, J. L.; Mallouk, T. E. *J. Phys. Chem. Lett.* **2011**, *2*, 402.

(4) Marković, N. M.; Schmidt, T. J.; Stamenković, V.; Ross, P. N. *Fuel Cells* **2001**, *1*, 105.

(5) Bard Allen J., F. L. R. *Electrochemical Methods: Fundamentals and Applications*; 2nd ed., 2001.

(6) Nørskov, J. K.; Rossmeisl, J.; Logadottir, A.; Lindqvist, L.; Kitchin, J. R.; Bligaard, T.; Jónsson, H. *J. Phys. Chem. B* **2004**, *108*, 17886.

(7) Casalongue, H. S.; Kaya, S.; Viswanathan, V.; Miller, D. J.; Friebel, D.; Hansen, H. A.; Nørskov, J. K.; Nilsson, A.; Ogasawara, H. *Nat Commun* **2013**, *4*.

(8) Man, I. C.; Su, H.-Y.; Calle-Vallejo, F.; Hansen, H. A.; Martínez, J. I.; Inoglu, N. G.; Kitchin, J.; Jaramillo, T. F.; Nørskov, J. K.; Rossmeisl, J. *ChemCatChem* **2011**, *3*, 1159.

(9) Siahrostami, S.; Vojvodic, A. *J. Phys. Chem. C* **2015**, *119*, 1032.

Appendix D: Supplementary Material for Chapter 5

The Importance of Nickel Oxyhydroxide Deprotonation on its Activity towards Electrochemical Water Oxidation

pH dependence of the potential for the Ni^{2+}/Ni^{3+} redox transition: comparison between Fe-free and Fe-containing electrolytes

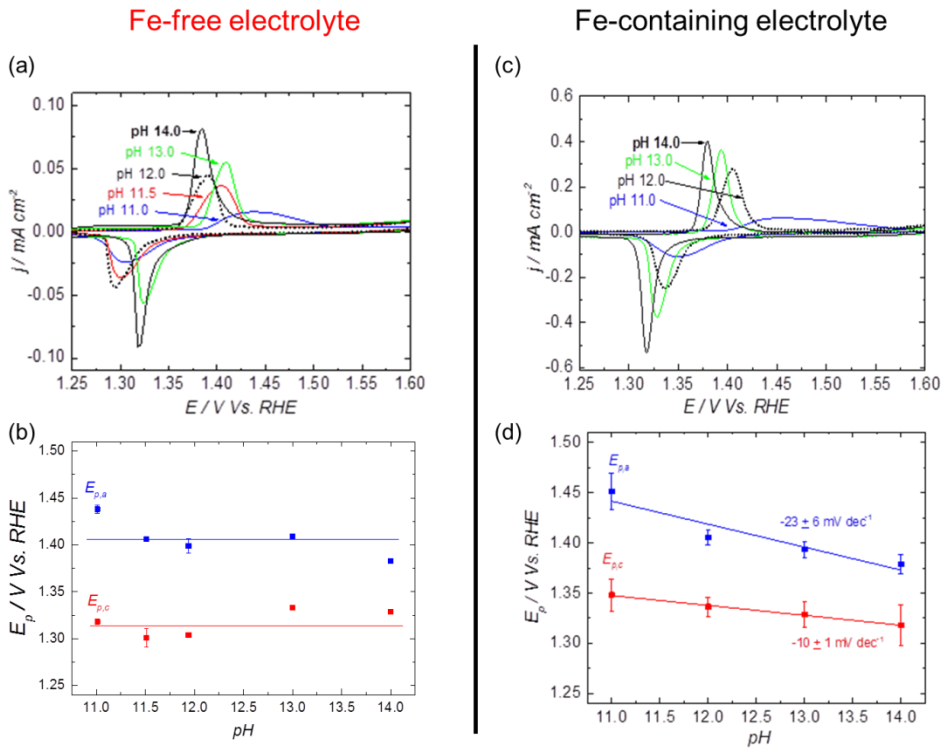

Figure D1. a) CVs of NiOOH acquired in purified (Fe-free) electrolyte, showing the changes in the Ni^{2+}/ Ni^{3+} redox transition with the pH. Scan rate: 0.01 V/s**.** b) Position of the oxidation and reduction peaks for the Ni^{2+} / Ni^{3+} redox transition ($E_{p,a}$ / $E_{p,c}$) in a) as a function of pH. c) CVs acquired in unpurified Fe-containing electrolyte, showing the changes in the Ni^{2+}/ Ni^{3+} redox transition with the pH. Scan rate: 0.01 V/s. d) Position of the oxidation and reduction peaks for the Ni^{2+} / Ni^{3+} redox transition ($E_{p,a}$ / $E_{p,c}$) in c) as a function of pH.

Capacitance-corrected OER activity of NiOOH as a function of pH

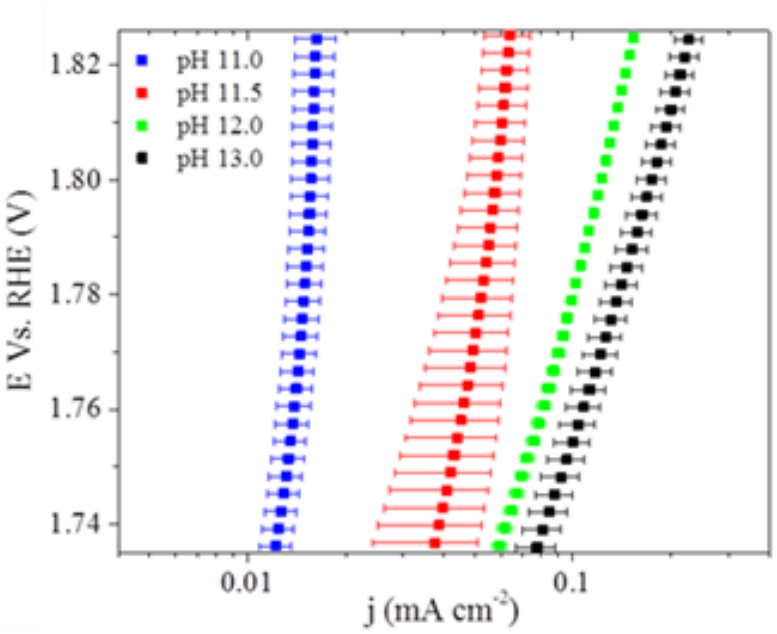

Figure D2. OER activity obtained from the average of the current measured in the forward and backward scan in the polarization curves of NiOOH deposited on Au (capacitance-corrected). Measurements at pH's 11 – 13 were performed at constant ionic strength, adjusted to 0.1 M with $NaClO_4$ except for pH 13, that solution was NaOH 0.1 M.

The catalytic activity of NiOOH towards OER: the effect of iron impurities in the electrolyte

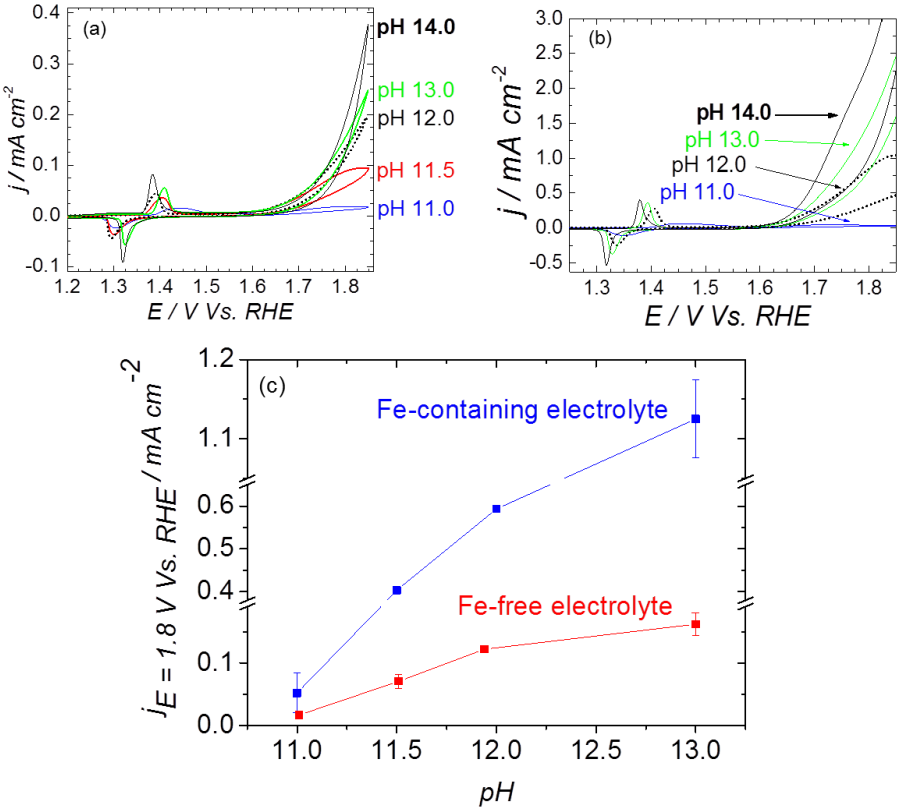

Figure D3. Effect of iron impurities on the activity of NiOOH towards OER. Measurements at pH's 11 – 13 were performed at constant ionic strength, adjusted to 0.1 M with $NaClO_4$. Solutions at pH 13 and pH 14 were NaOH 0.1 M and 1 M respectively. Scan rate: 0.01 V/s. a) CVs measured in Fe-free electrolyte. b) CVs measured in Fe-containing electrolyte. c) Capacitance-corrected activity of NiOOH towards OER as a function of pH, the activity was measured from the CVs a) and b) as the average of the backwards and forward current density at 1.8 V vs. RHE.

Additional SERS spectra of NiOOH in the Fe-free electrolyte

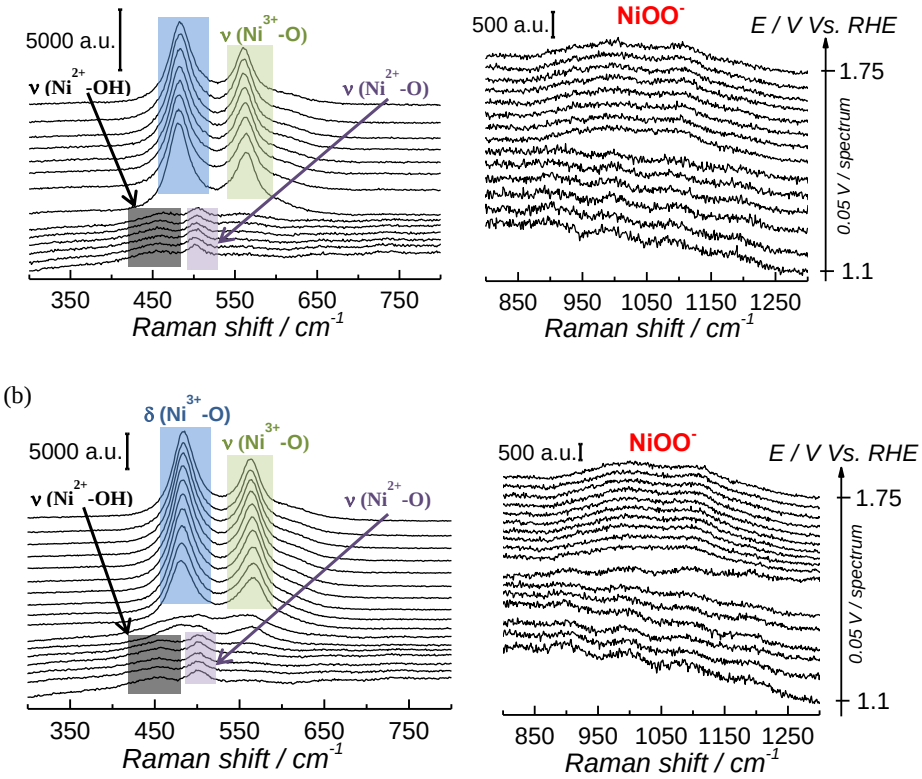

Figure D4. SER spectra obtained at constant potential during the electrochemical oxidation of $Ni(OH)_2$ and the subsequent OER on NiOOH at different pH's. The ionic strength of the solution was fixed to 0.1 M with $NaClO_4$. The left panel presents the spectra in the wavenumber region 300 – 800 cm^{-1} and the right panel presents the wavenumber region 800 – 1300 cm^{-1}: a) pH 11.5, b) pH 14.0.

SERS experiments in solutions prepared with $H_2{}^{18}O$

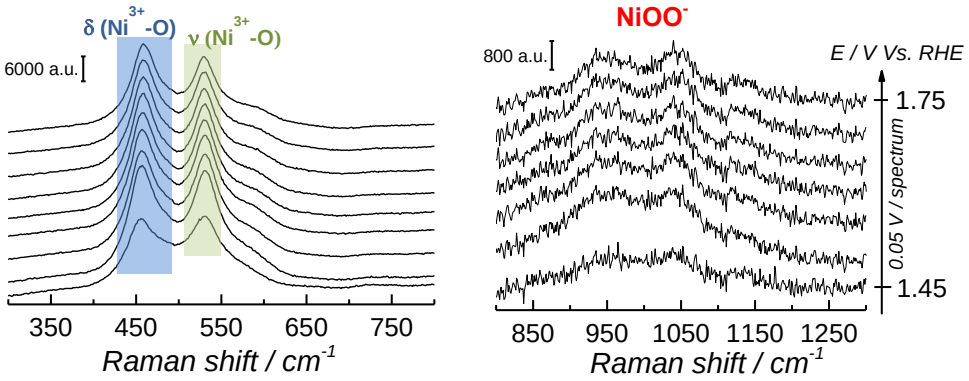

Figure D5. SER spectra obtained at constant potential during the electrochemical oxidation of $Ni(OH)_2$ and the subsequent OER on NiOOH at pH 13. The electrolyte was prepared in $H_2{}^{18}O$. The left panel presents the spectra in the wavenumber region 300 – 800 cm^{-1} and the right panel presents the wavenumber region 800 – 1300 cm^{-1}.

Position of the Raman peaks of NiOOH in electrolytes prepared with $H_2{}^{16}O$ and $H_2{}^{18}O$

Table D1. Position of the Raman peaks associated with the vibrations $\delta(Ni^{3+}\text{-}O)$, $\nu(Ni^{3+}\text{-}O)$ and $NiOO^-$ as a function of the oxygen isotope in the electrolyte. The spectra were obtained in NaOH 0.1 M in potentiostatic conditions.

E (V vs. RHE)	$\delta(Ni^{3+}\text{-}O)$		$\nu(Ni^{3+}\text{-}O)$		$NiOO^-$			
	^{16}O	^{18}O	^{16}O	^{18}O	^{16}O	^{18}O	^{16}O	^{18}O
1.65	481 ± 1	459 ± 3	561 ± 1	530 ± 5	986 ± 9	908 ± 9	1093 ± 2	1054 ± 5
1.7	482 ± 1	460 ± 1	561 ± 1	531 ± 3	991 ± 8	891 ± 12	1097 ± 8	1054 ± 8
1.75	481 ± 1	458 ± 3	560 ± 1	529 ± 5	991 ± 13	896 ± 8	1096 ± 7	1068 ± 6

Appendix E: Supplementary Material for Chapter 6

Iridium-based Double Perovskites for Efficient and Cost Effective Water Oxidation in Acid Media

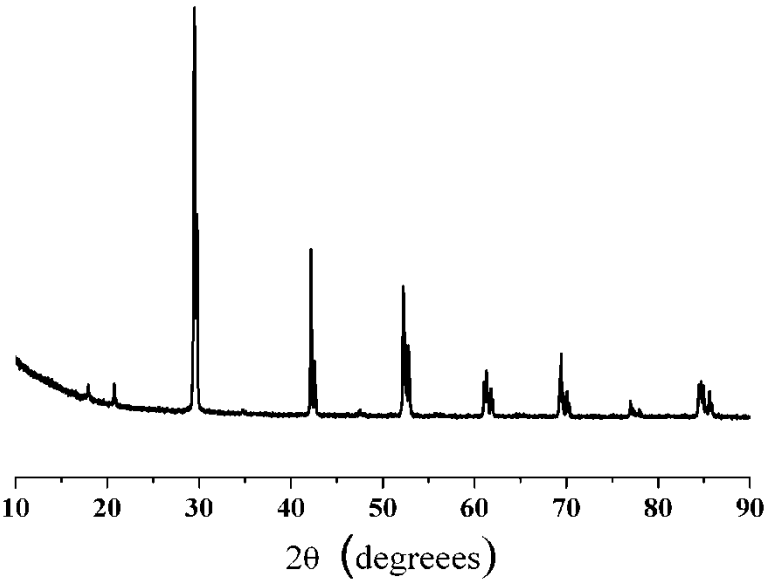

Figure E1. Powder XRD for the Ba_2LaIrO_6 double perovskite

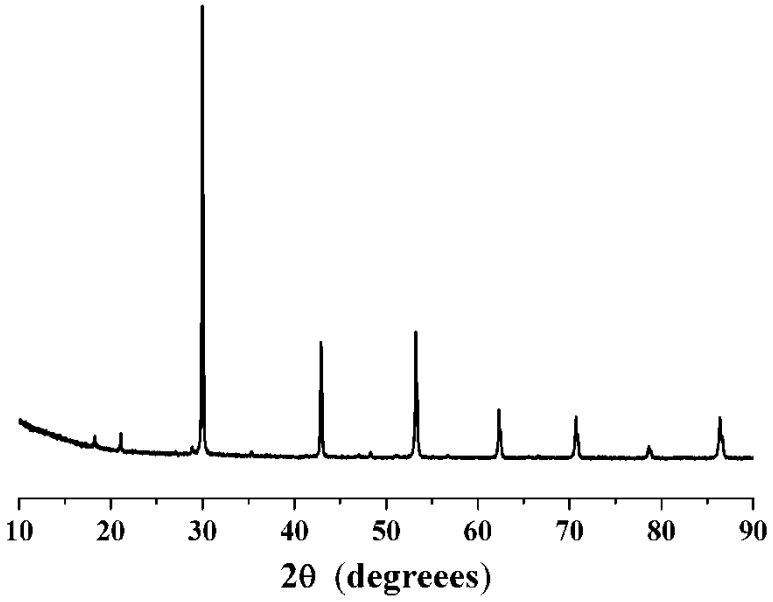

Figure E2. Powder XRD for the Ba_2CeIrO_6 double perovskite

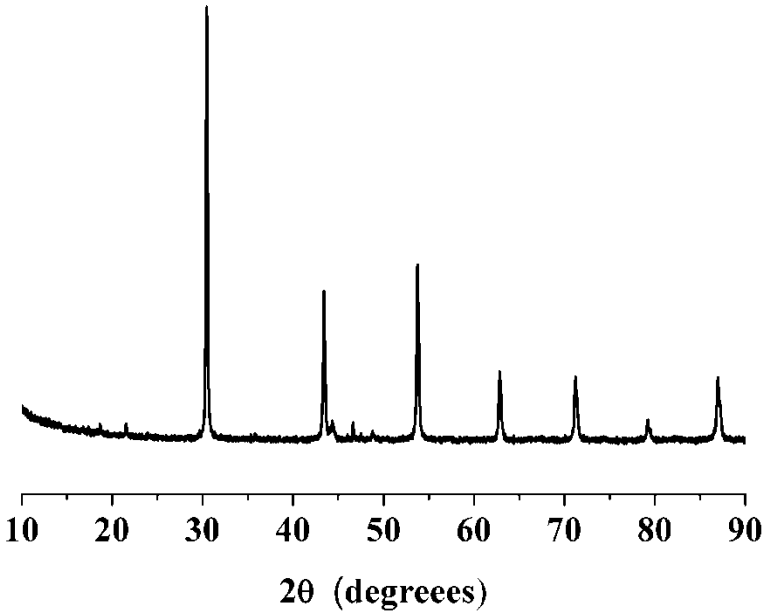

Figure E3. Powder XRD for the Ba_2PrIrO_6 double perovskite

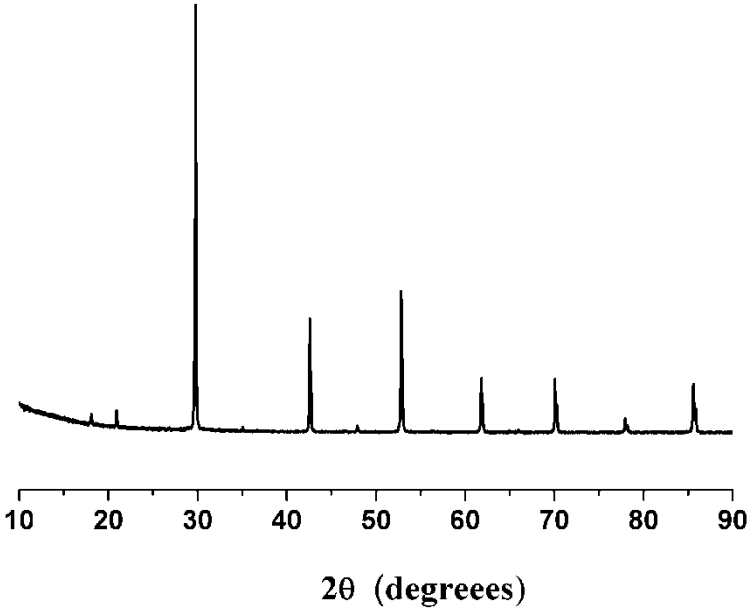

Figure E4. Powder XRD for the Ba_2NdIrO_6 double perovskite

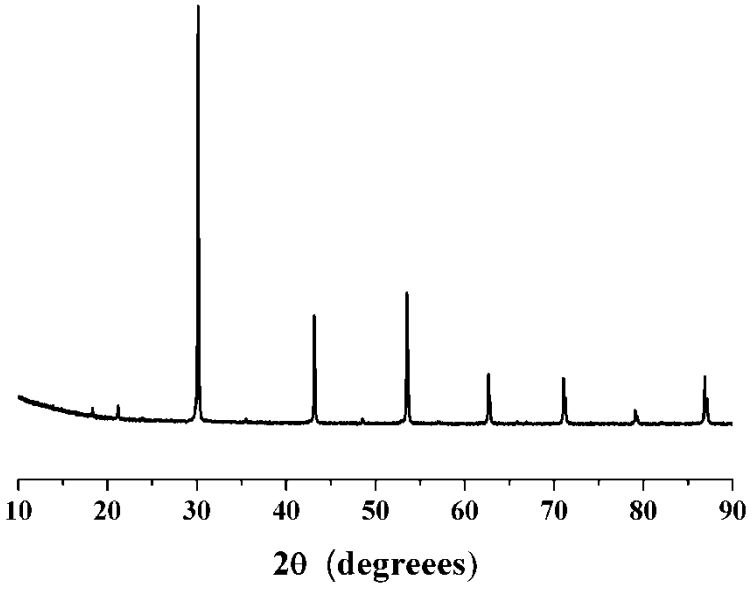

Figure E5. Powder XRD for the Ba_2TbIrO_6 double perovskite

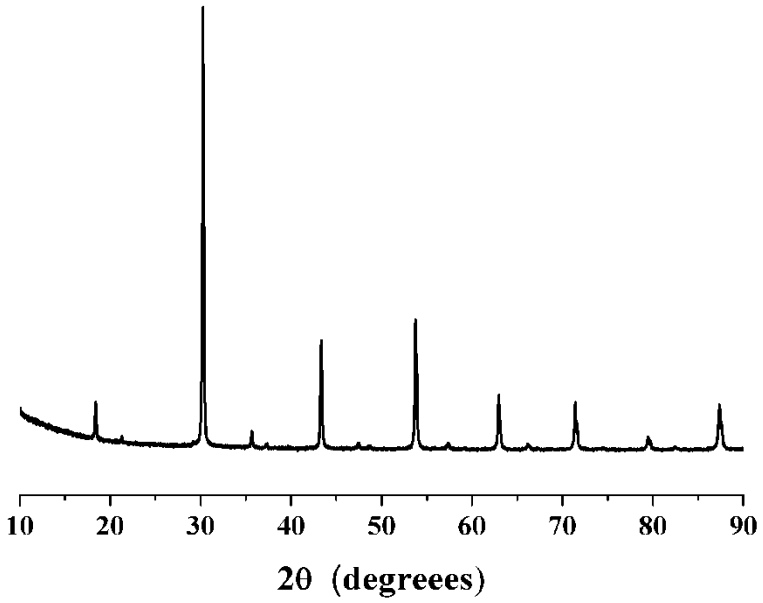

Figure E6. Powder XRD for the Ba_2YIrO_6 double perovskite

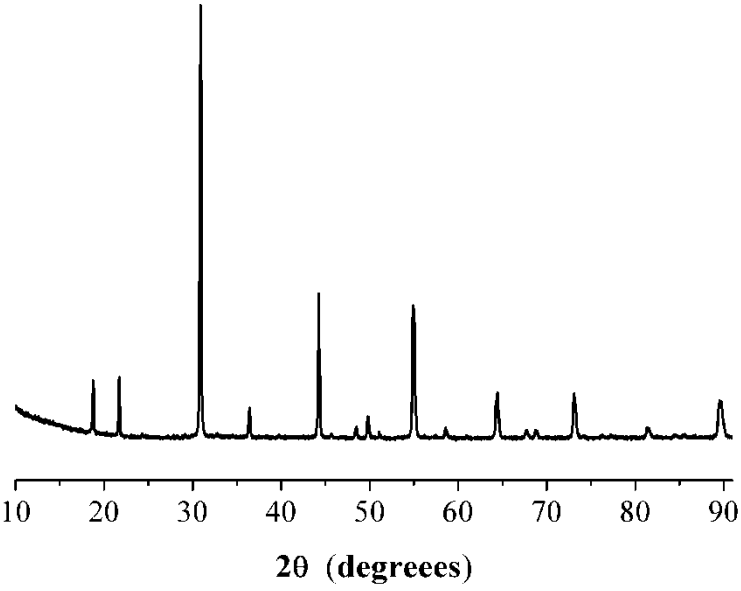

Figure E7. Powder XRD for the Sr_2YIrO_6 double perovskite

Table E1. Tafel slope for the water splitting reaction in 0.1 M $HClO_4$ for IrO_2 and the iridium-based double perovskites. Currents were measured in steady-state conditions. Rotation rate: 1500 RPM.

	Tafel slope (mV/dec) (E = 1.5-1.6 V vs. RHE)	**Tafel slope (mV/dec) (E> 1.6 V vs. RHE)**
IrO_2	57 ± 1	115 ± 13
Ba_2LaIrO_6	59 ± 3	127 ± 10
Ba_2CeIrO_6	57 ± 7	121 ± 12
Ba_2PrIrO_6	54 ± 3	106 ± 17
Ba_2NdIrO_6	59 ± 4	136 ± 1
Ba_2TbIrO_6	61 ± 3	118 ± 9
Ba_2YIrO_6	67 ± 4	196 ± 23

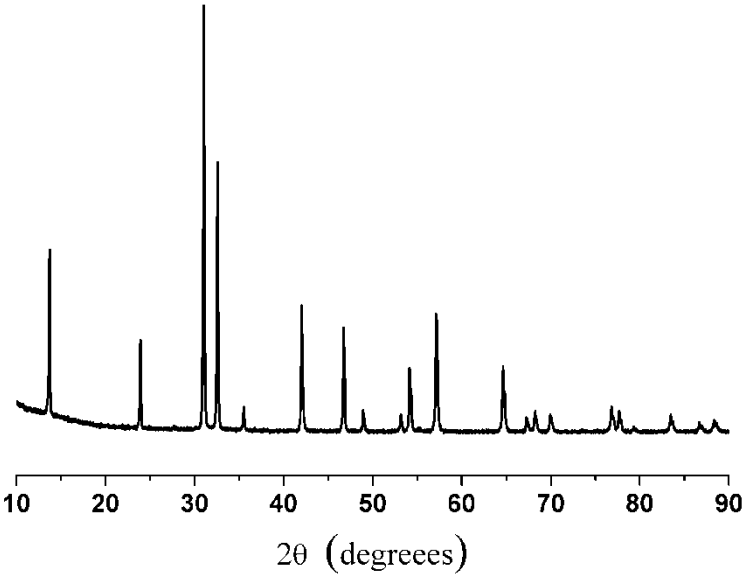

Figure E8. Powder XRD for Sr_2IrO_4 layered perovskite Ruddlesden-Popper phase

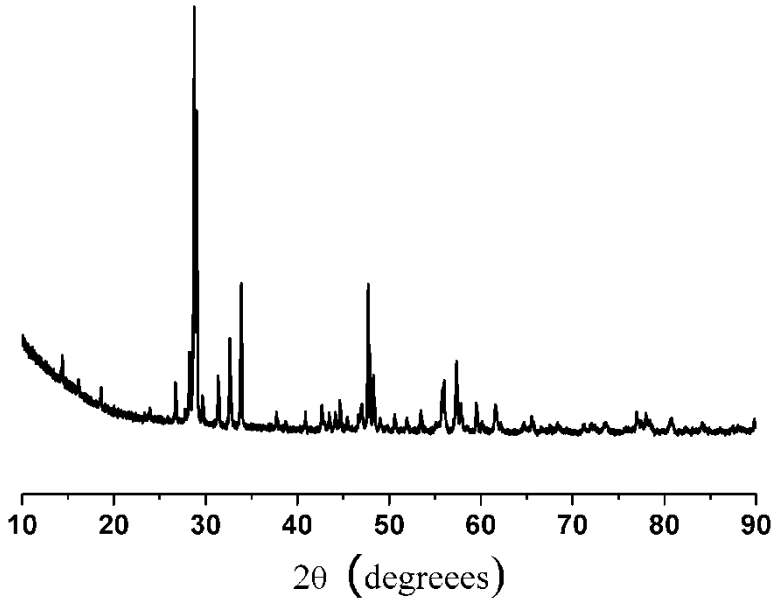

Figure E9. Powder XRD for Pr_3IrO_7 fluorite-like phase

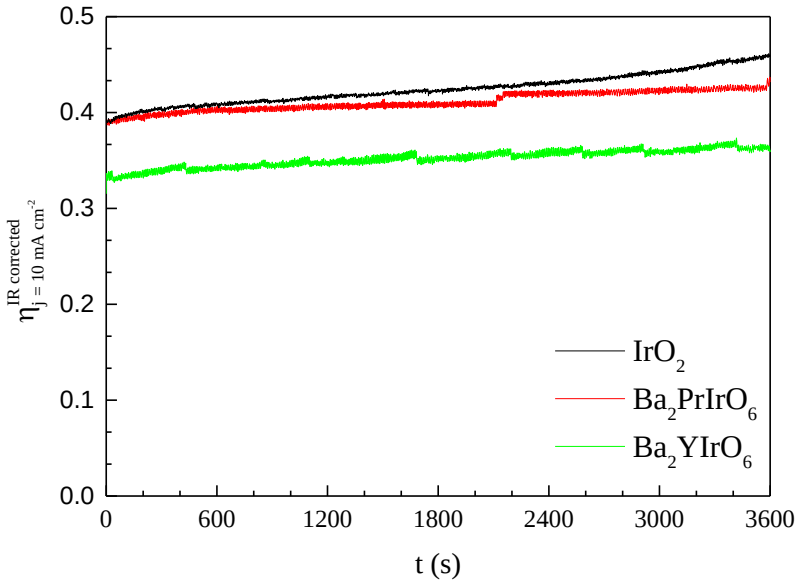

Figure E10. Evolution of the overpotential towards electrochemical water oxidation in 0.1 M $HClO_4$ Ba_2PrIrO_6 / Ba_2YIrO_6 double perovskites, measured by applying a constant current density of 10 mA cm_{disk}^{-2} during 1 h in hydrodynamic conditions (rotation rate: 1500 RPM). The stability of IrO_2 nanoparticles is presented for comparison.

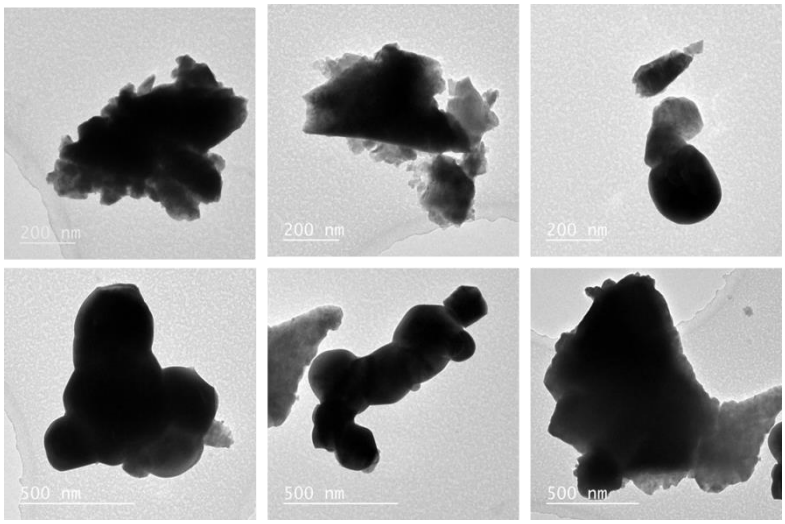

Figure E11. TEM images of the pristine sample of Ba_2LaIrO_6 double perovskite.

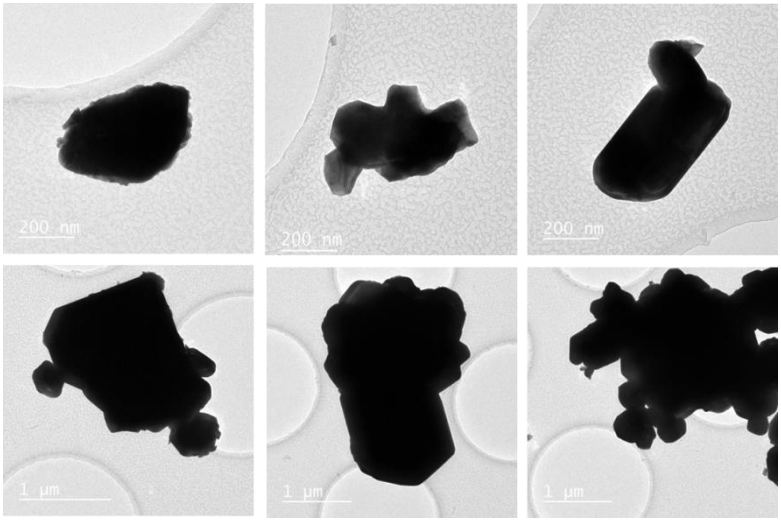

Figure E12. TEM images of the pristine sample of Ba_2CeIrO_6 double perovskite.

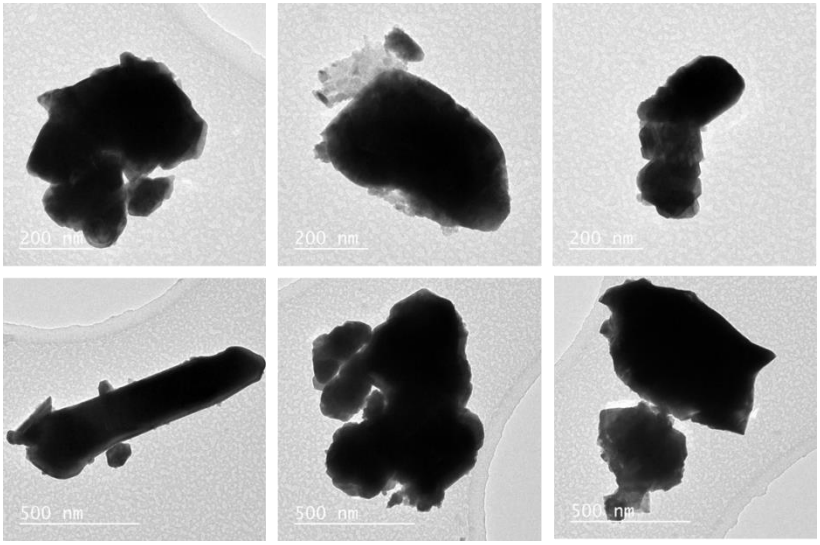

Figure E13. TEM images of the pristine sample of Ba_2PrIrO_6 double perovskite.

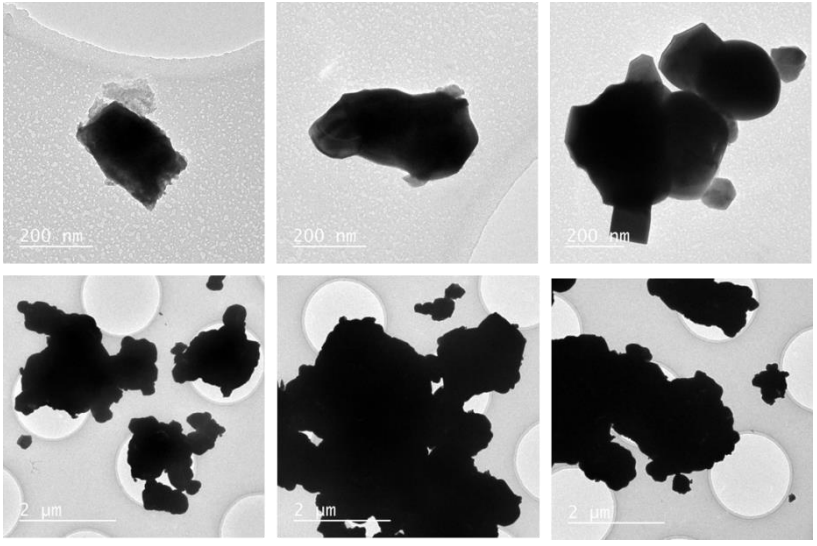

Figure E14. TEM images of the pristine sample of Ba_2NdIrO_6 double perovskite.

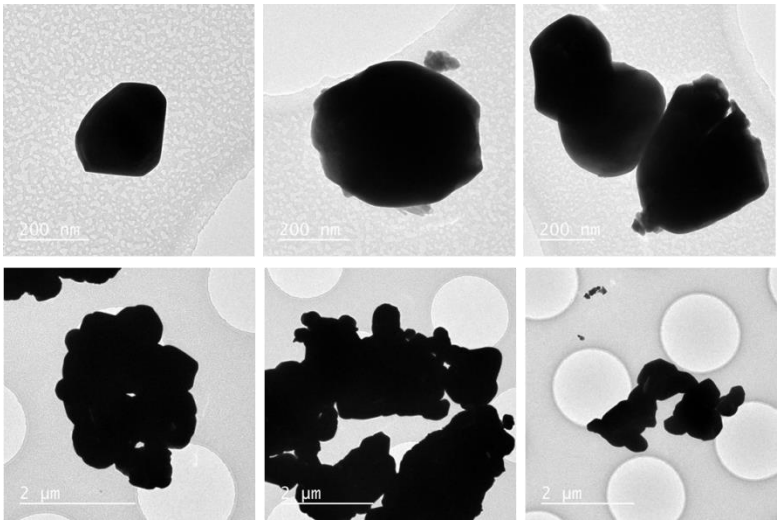

Figure E15. TEM images of the pristine sample of Ba_2TbIrO_6 double perovskite.

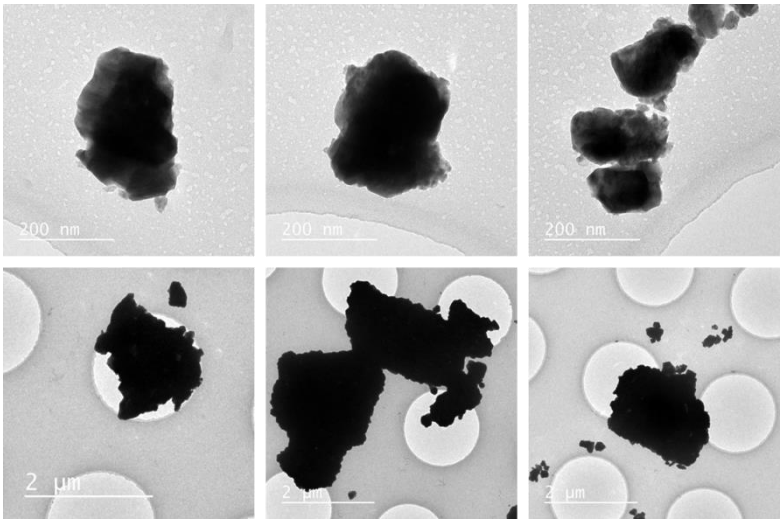

Figure E16. TEM images of the pristine sample of Ba_2TbIrO_6 double perovskite.

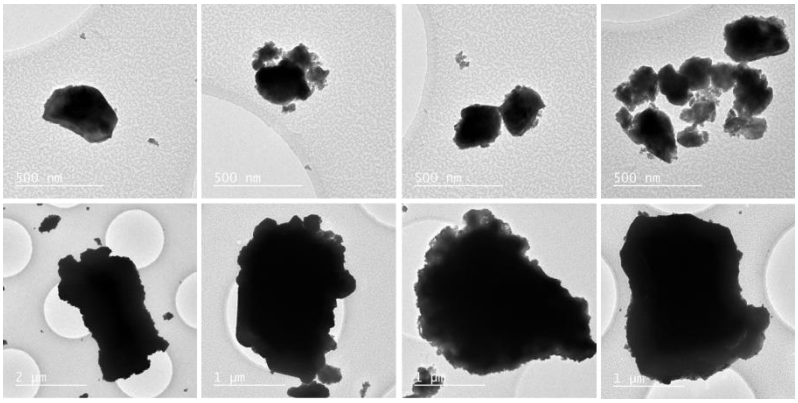

Figure E17. TEM images of Ba_2PrIrO_6 double perovskite after leaching in $HClO_4$ 0.1 M for 48 h.

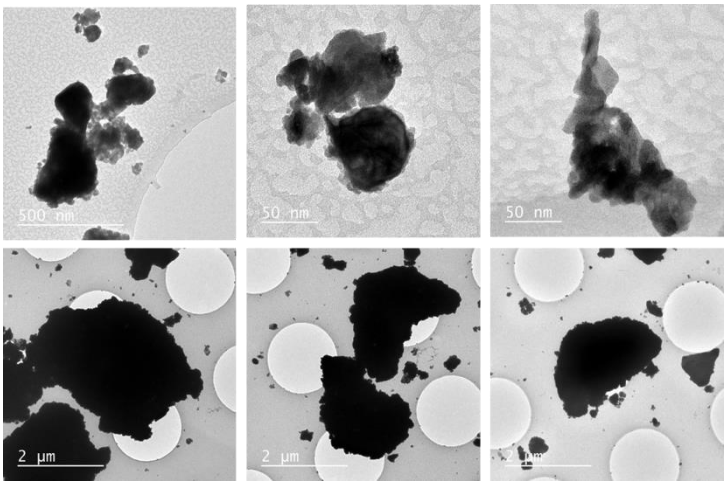

Figure E18. TEM images of Ba_2PrIrO_6 double perovskite after leaching in 0.1 M $HClO_4$ + 4 M H_2O_2 for 48 h.

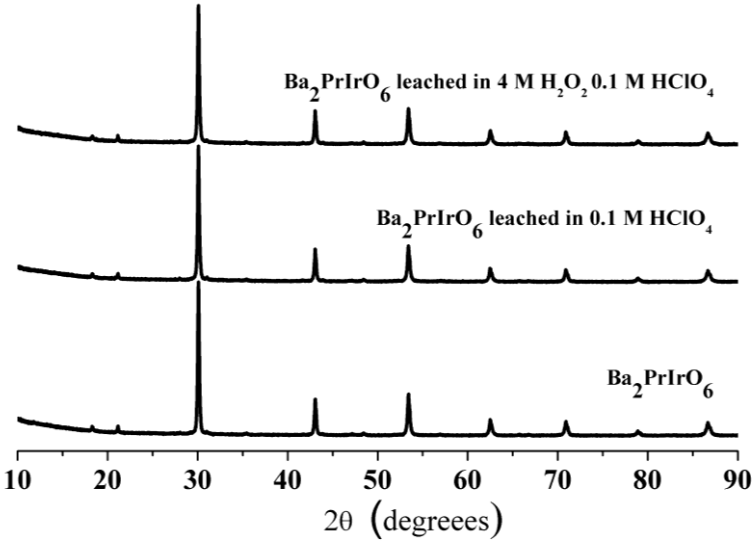

Figure E19. Powder XRD of the Ba_2PrIrO_6 before and after the leaching treatments. XRD pattern of the Ba_2PrIrO_6 pristine sample is presented for comparison.

XPS analysis of the pristine and leached Ba2PrIrO6 double perovskite

The results of the XPS analysis of the Ba_2PrIrO_6 double perovskite before and after exposure to the oxidizing environment are presented in Figure E20.

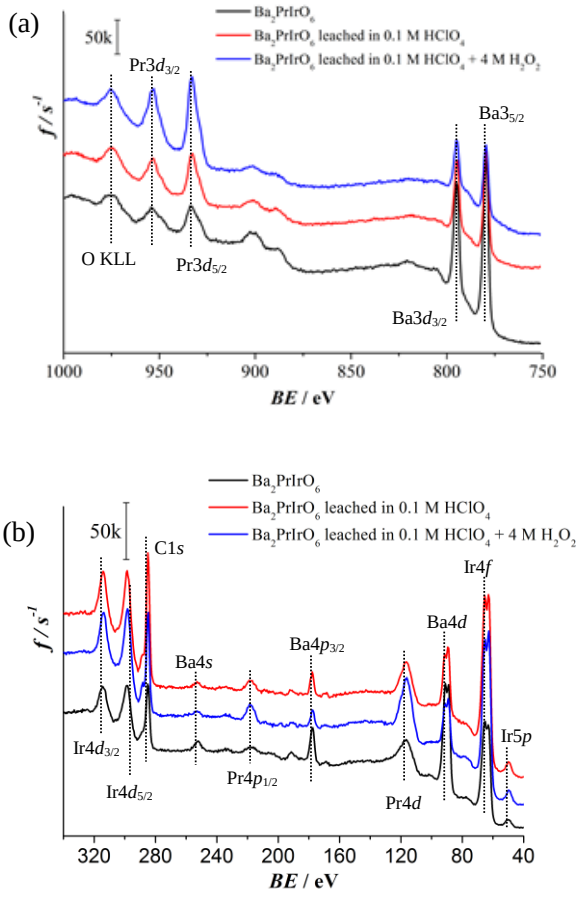

Figure E20. XPS spectra of pristine Ba_2PrIrO_6 before and after the leaching treatments. a) Binding energy region 750 – 1000 eV. b) Binding energy region 40 – 340 eV.

It is clearly shown in Figure E20 that the pristine double perovskite contains a much larger contribution of Ba ($3d_{3/2}$, 794.9 eV; $3d_{5/2}$, 779.6 eV) relative to Pr ($3d_{3/2}$, 953.4 eV; $3d_{5/2}$, 933.0 eV) compared to the leached samples. The surface of the double perovskite enriches with praseodymium upon leaching with hydrogen peroxide and perchloric acid, which is indicated by the relative intensities in Figure E20. The intensity of the peaks attributed to iridium (Ir4$d_{3/2}$, 313.9; Ir4$d_{5/2}$, 298.1 eV and Ir4*f*, 63.8 eV) increases for the sample leached in 0.1 M $HClO_4$, however, the oxidative treatment in 0.1 M $HClO_4$ + 4 M H_2O_2 slightly reduces the intensity of the iridium peaks, indicating that the noble metal started to leach.

The surface composition of the pristine and leached Ba_2PrIrO_6 samples is summarized in table E2. The XPS results show that the relative atomic composition in the pristine double perovskite is very close to the expected values, indicating that the surface exhibits the same composition as the bulk of the double perovskite. Again, the results show the surface composition of the Ba_2PrIrO_6 enriches in iridium and praseodymium upon the leaching treatments, whereas the barium is depleted from the surface.

Table E2: Surface composition of Ba, Pr and Ir in the pristine Ba_2PrIO_6 and after the leaching treatments with 0.1 M $HClO_4$ and 0.1 M $HClO_4$ + 4 M H_2O_2, obtained from XPS analysis. The expected values were obtained from the chemical formula of the compound reported by Fu and Ijdo[1].

	Ba	**Pr**	**Ir**
Expected values	2.00	1.00	1.00
Pristine Ba_2PrIrO_6	2.46	0.97	1.00
Ba_2PrIrO_6 leached in 0.1 M $HClO_4$	0.85	0.77	1.00
Ba_2PrIrO_6 leached in 0.1 M $HClO_4$ + 4 M H_2O_2	0.60	1.39	1.00

The change in the oxidation state of barium, praseodymium and iridium in the samples was analyzed using the high-resolution scans of the core-level in the XPS spectra. The oxidizing treatment did not eliminate or change the adventitious carbon signal, allowing the use of the

C1s signal as energy calibration at 284.8 eV (see Figure E20b). The deconvolution analysis of the XPS spectra shows that the surface of the double perovskite contains additional oxidation states different from the bulk composition (see Figure E21).

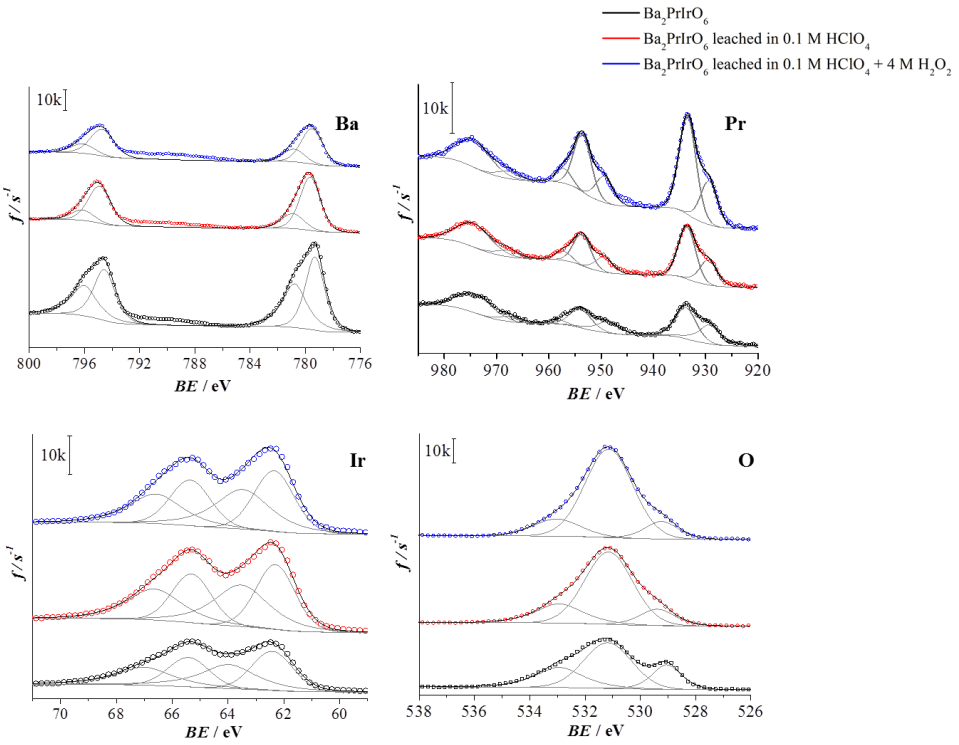

Figure E21: Core-level XPS spectra (Ba3*d*, Pr3*d*, Ir4*f* and O1*s*) of Ba_2PrIrO_6 before and after the leaching treatments.

The Ba3*d* core-level spectra in Figure E21 show the $3d_{3/2}$ and $3d_{5/2}$ contributions with spin-orbit coupling of 15.3 eV. The deconvolution was carried out with fixed 3:2 intensity ratios to exclude possible Pr MNN overlap at 797 eV and Ba shake-off features on the lower binding energies side of the Ba3$d_{3/2}$ signal. The deconvoluted spectra of the Ba3$d_{3/2}$ peak show two Ba^{2+} phases, one that can be related to the bulk perovskite (*ca.* 779.5 eV) and a different surface phase at *ca.* 780.8 eV)[2-4] . The spectra of pristine Ba_2PrIrO_6 look similar to

other Ba-containing perovskites (*e.g.* $BaTiO_3$) with a typical high-energy shoulder at *ca.* 1.3 eV above the main peak with an intensity ratio of around 0.6[4,5]. The leaching of barium from the Ba_2PrIrO_6 double perovskite surface is accompanied with a relative decrease in the high-energy component, indicating removal of the surface phase and exposure of the barium-bulk phase. Furthermore, the typical Ba perovskite binding energy shifts approximately 0.3 eV to higher binding energies, indicating the change in environment to a more oxidized character[6]. The oxidizing treatment has a detrimental effect on the Ba content, heavily perturbing both the Ba surface and bulk phase. The ionic character of Ba in addition to its location in the cavity of the PrO_6/IrO_6 octahedra may be the cause of its easier exclusion from the structure.

The Pr3*d* core-level spectra (see Figure E21) consist of two main signals from the ground state 4*f* configuration with spin-orbit coupling of 20.1 eV and accompanying shoulders and shake-off features resulting from a mixture of final state configurations[7,8]. The signals were recorded including the O1s Auger line to properly assess the distinct features that indicate a mixture of tri- and tetravalent species. The Pr3$d_{5/2}$ and Pr3$d_{3/2}$ signals of the pristine double perovskite are broad, with a FWHM of 4.7 eV, but the main peaks can be unambiguously fitted with the statistical 3:2 intensity ratio and 20.1 eV spin-orbit coupling, indicating that mainly Pr^{3+} is present[9]. The 3$d_{5/2}$ binding energy of 933.8 eV agrees well with the binding energy of praseodymium in a $PrAlO_3$ perovskite lattice[10], approximately 1.0 eV above the value reported for Pr_2O_3[7,11]. The satellite energy separation of both signals is large, in the range of the reported values for trivalent Pr in highly electronegative ligand orientation[12]. Satellite spin-orbit coupling of 19.4 eV is lower than the expected (*ca.* 20.5 eV), and shake-off in the 3$d_{3/2}$ region is visible around 958 eV indicating Pr^{4+} contributions, with PrO_2 nature[11,13]. The main and satellite relative intensity ratios of 0.6 are in the upper limit of trivalent species, and in addition to the abovementioned features, this indicates mixed-valence praseodymium species present in the perovskite structure. The acid treatment induced subtle changes in the spectra of praseodymium, suggesting minor but notable changes in the perovskite surface environment. The binding energy of the main peak shifted 0.3 eV to lower energy, and the width narrowed to FWHM values of 3.9 eV. Moreover, the satellite energy separation decreased and coincides with values for Pr_2O_3. Similarly, the

satellite intensity ratio of the $3d_{5/2}$ signal is reduced to values very close to the value in Pr_2O_3 [12]. The leaching treatment induces the removal of praseodymium from the perovskite through surface oxidation to form other phases with Pr^{3+}. The Ba:Pr ratio is approximately 1:2, which might indicate the formation of a Pr_2BaO_4 spinel surface phase[13].

The Ir4*f* core-level spectra show two broad signals separated by an extraordinary high saddle between $4f_{5/2}$ and $4f_{7/2}$, indicating two superimposed spectra (see Figure E21)[14]. The deconvolution yields two contributions with spin-orbit coupling of 3.0 eV and different FWHM. The high binding energy peak is probably broader as a result of conduction band interaction during the photoemission process[15,16]. The binding energy values for the $4f_{7/2}$ peak of 62.4 and 64.0 eV are about 0.3 eV higher than reported for iridium compounds with Ir^{4+}, the difference may be attributed to electronic charge transfer with praseodymium in the perovskite[17,18]. It is striking that the high binding energy peak shifts 0.5 eV towards lower binding energies after the oxidizing treatments, while the low binding energy peak value of 62.4 eV is unchanged. Moreover, the 1:1 relative ratio of the two contributions is maintained after the oxidizing treatment. Taking into account the formal Ir^{4+} valence of the bulk perovskite, the prominent saddle and increasing suspicion of Pr^{3+} contributions, the system is likely bivalent with Ir^{4+} and Ir^{5+} present in roughly equivalent ratio[1].

The O1*s* core-level spectra have been resolved with three peaks to distinguish between the contributions of the metal oxides and the surface-adsorbed species (see Figure E21). The main peak of the pristine double perovskite is located around 531 eV and is accompanied by a high binding energy shoulder and a low binding energy peak at 529 eV. The main peak is either ascribed directly to the constitutional metal oxide, or more indirectly to oxyhydroxide or metal carbonate signals originating from interactions with the metal oxide surface[4,11,15,17-20]. The value of 531.1 eV agrees as well with ionic Ba-O-V bonds of non-bridging oxygen in barium vanadophosphate glasses, corresponding to a Ba-O coordination resembling the one in perovskite[21]. The low binding energy peak is ascribed to the O1*s* signal of a lattice oxygen, more specific from the lattice oxygen bound to Pr^{3+} or Pr^{4+} [11,18,19]. The O1*s* metal oxide contribution of perovskite-type $BaTiO_3$ has a similar value of 529.0 eV, which is identical to other Pr-based perovskites such as $PrCoO_3$, and mixed $PrCaMnO_3$,

once more indicating overlap of different metal-oxide signals[4]. This lattice oxygen binding energy is somewhat on the low side for Ir^{4+} compounds, however, these values are not reported for perovskite phases[17]. In all abovementioned analyses, the 533 eV peak is assigned to surface contamination from adsorbed water or related hydroxide species. The effect of the oxidizing treatment on the O1*s* spectra is clear; the main peak further exceeds the high binding energy shoulder and lower binding energy peak. The lattice oxygen contribution is decreased to a minor shoulder, and its binding energy shifts to higher values. Thus, the oxyhydroxide and metal carbonate contribution has increased with respect to the surface contaminants and lattice oxygen, indicating that the surface coverage of the perovskite metal-oxide phase increases. The shift in binding energy is observed as well for $BaTiO_3$ perovskites, where the lattice oxygen signal at 529.0 eV shifted to 529.3 eV after prolonged oxidation times, displaying the electronic interaction of the bulk with the oxidized surface[4]. A shift in binding energy of the lattice oxygen in the case of Pr would imply a reduction from Pr^{4+} to Pr^{3+}, which could indicate a surface reorganization with other metals into different mixed-valence phases[13].

Summarizing, the deconvolution analysis of the XPS Ba, Pr, Ir and O core-levels indicate that next to the tetravalent Pr^{4+}/Ir^{4+} valence pair, a surface phase exists containing Pr^{3+} and Ir^{5+} (see Figure E21), however, the chemical nature of these species cannot be confirmed. The oxidizing treatment greatly perturbs the surface of the perovskite, majorly reducing the Ba content to values below that of Pr and Ir. The leaching further enhances the differences in the oxidation state, increasing the Ir^{5+} contribution.

Faradaic efficiency of Ba_2PrIrO_6 towards OER in 0.1 M $HClO_4$

The faradaic efficiency towards water splitting in acid media was measured in RRDE configuration; the results are summarized in Figure E20. The efficiency (ε) was calculated with equation (D1), assuming that the oxygen reduction proceeds via four electron transfer, to produce water[22].

$$\varepsilon = \frac{i_{ring}}{i_{disk} \cdot N} \times 100 \qquad \text{(E1)}$$

The collection factor (N) for oxygen was measured by using IrO_2 as reference catalyst (see Figure E21 for further details), and the value obtained was 0.199 ± 0.001, which corresponds well with the value obtained from measurements with the redox couple $[Fe(CN)_6]^{3-}/[Fe(CN)_6]^{4-}$ (N=0.23); the small difference has been attributed to the non-ideal outward flow of O_2[23].

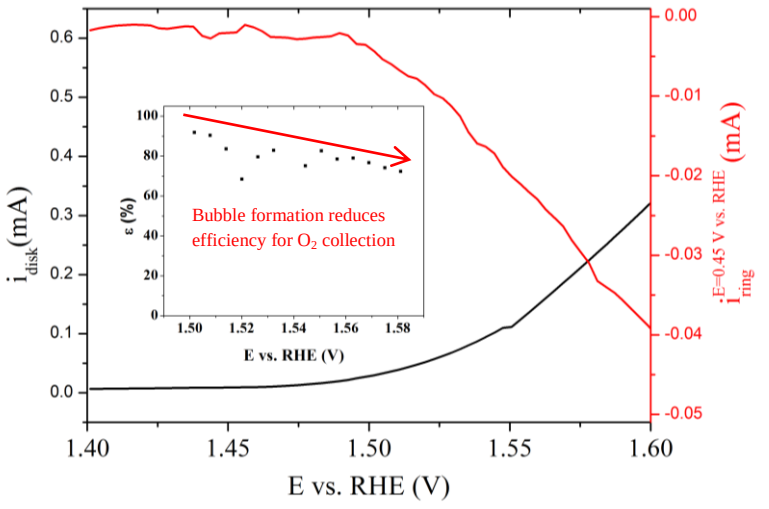

Figure E20. RRDE measurement of the catalytic activity of Ba_2PrIrO_6 towards water splitting in 0.1 M HClO4; measurements were performed by cyclic voltammetry at 0.01 V /s. Insert: Faradaic efficiency for water splitting.

Collection factor for O_2 detections in the RRDE configuration

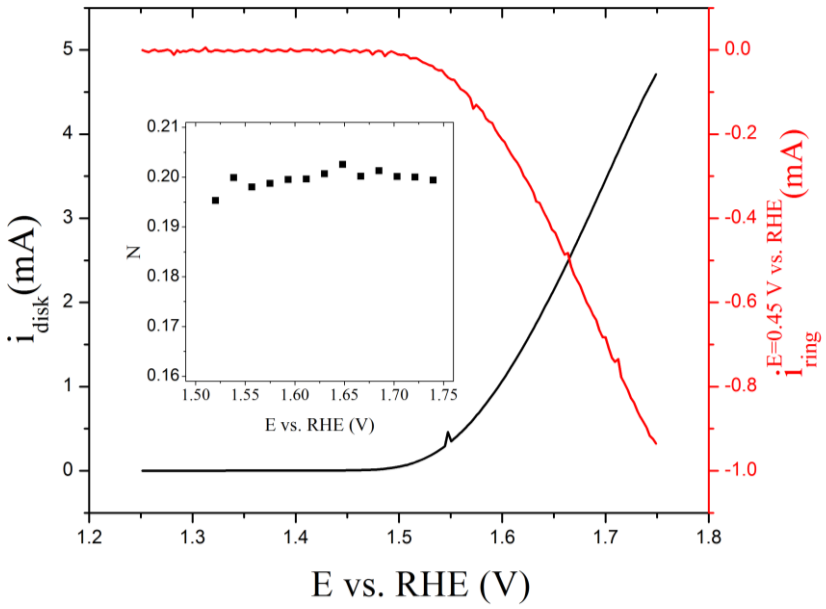

Figure E21. Oxygen collection factor measurement. Scan rate: 0.01 V/s, rotation rate: 1500 RPM.

The collection factor was measured assuming that oxygen is reduced to water ($O_2 + 4H^+ + 4e^- \rightarrow 2H_2O$)[22], according to the following equation[24]:

$$N = \frac{i_{ring}}{i_{disk}} \qquad \text{(E2)}$$

Elemental analysis of the dissolved components from the Ba_2PrIrO_6 double perovskite after electrochemical water oxidation at pH 1

The amount of dissolved components from the praseodymium-barium iridium double perovskite after electrochemical water oxidation experiments in 0.1 M $HClO_4$ was measured by means of inductively coupled plasma atomic emission spectroscopy (ICP-AES). These experiments were performed potentiostatically (1 h electrolysis) and in non-rotating conditions, using 10 mL of electrolyte. The double perovskite catalyst was drop-casted on a gold disk (950 $\mu g_{oxide}/cm_{disk}^2$ of Ba_2PrIrO_6), using the ethanol-based ink similar to the one described for the RRDE experiments but with higher perovskite content (30 mg_{oxide}/mL_{ink}). The electrolyte was analyzed directly in a Varian Vista-MPX CCD Simultaneous ICP-AES. Table E3 summarizes the ICP-AES results.

Table E3. Fraction of Ba, Pr and Ir dissolved from the Ba_2PrIrO_6 after 1 h of electrolysis at constant potential in $HClO_4$ 0.1 M.

E vs. RHE (V)	% Ba leached	% Ir leached	% Pr leached
1.45	12.7	0.6	9.5
1.55	14.2	0.8	11.3

The fraction of dissolved metal (% M leached) was calculated as follows:

$$\%\ \text{M leached} = \frac{m_M(mg)in\ solution}{m_M\ (mg)drop-casted} \times 100$$

In this equation m_M *(mg) in solution* was obtained from the ICP-AES analysis after the electrolysis experiment and m_M *(mg)drop-casted* corresponds to the mass of each component of the Ba_2PrIrO_6 double perovskite, calculated from its stoichiometry.

The results in table E2 show that approximately 10% of Ba and Pr are leached out from the double perovskite in the potential region 1.45 – 1.55 V vs. RHE, however, the dissolution of the noble metal is negligible.

REFERENCES

(1) Fu, W. T.; Ijdo, D. J. W. *J. Solid State Chem.* 2005, *178*, 1312.

(2) Meyer, H. M.; Hill, D. M.; Wagener, T. J.; Gao, Y.; Weaver, J. H.; Capone, D. W.; Goretta, K. C. *Phys. Rev. B* 1988, *38*, 6500.

(3) Fukuda, Y.; Nagoshi, M.; Suzuki, T.; Namba, Y.; Syono, Y.; Tachiki, M. *Phys. Rev. B* 1989, *39*, 11494.

(4) Miot, C.; Husson, E.; Proust, C.; Erre, R.; Coutures, J. P. *J. Mater. Res.* 1997, *12*, 2388.

(5) Mukhopadhyay, S. M.; Chen, T. C. S. *J. Mater. Res.* 1995, *10*, 1502.

(6) Moulder, J. F.; Chastain, J. *Handbook of X-ray Photoelectron Spectroscopy: A Reference Book of Standard Spectra for Identification and Interpretation of XPS Data*; Physical Electronics, 1995.

(7) Ogasawara, H.; Kotani, A.; Potze, R.; Sawatzky, G. A.; Thole, B. T. *Phys. Rev. B* 1991, *44*, 5465.

(8) Burroughs, P.; Hamnett, A.; Orchard, A. F.; Thornton, G. *J. Chem. Soc., Dalton Trans.* 1976, 1686.

(9) Sarma, D. D.; Rao, C. N. R. *J. Electron. Spectrosc. Relat. Phenom.* 1980, *20*, 25.

(10) Kruczek, M.; Talik, E.; Pawlak, D. A.; Kołodziejak, K.; Łukasiewicz, T. *J. Alloys Compd.* 2007, *442*, 255.

(11) Lutkehoff, S.; Neumann, M.; Slebarski, A. *Phys. Rev. B* 1995, *52*, 13808.

(12) Berthou, H.; Jørgensen, C. K.; Bonnelle, C. *Chem. Phys. Lett.* 1976, *38*, 199.

(13) Felner, I.; Yeshurun, Y.; Hilscher, G.; Holubar, T.; Schaudy, G.; Yaron, U.; Cohen, O.; Wolfus, Y.; Yacoby, E. R.; Klein, L.; Potter, F. H.; Rastomjee, C. S.; Egdell, R. G. *Phys. Rev. B* 1992, *46*, 9132.

(14) Atanasoska, L.; Atanasoski, R.; Trasatti, S. *Vacuum* 1990, *40*, 91.

(15) Peuckert, M. *Surf. Sci.* 1984, *144*, 451.

(16) Wertheim, G. K.; Guggenheim, H. J. *Phys. Rev. B* 1980, *22*, 4680.

(17) Kötz, R.; Neff, H.; Stucki, S. *J. Electrochem. Soc.* 1984, *131*, 72.

(18) Hara, M.; Asami, K.; Hashimoto, K.; Masumoto, T. *Electrochim. Acta* 1983, *28*, 1073.

(19) Fissel, A.; Dąbrowski, J.; Osten, H. J. *J. Appl. Phys.* 2002, *91*, 8986.

(20) Hall, H. Y.; Sherwood, P. M. A. *Journal of the Chemical Society, Faraday Transactions 1: Physical Chemistry in Condensed Phases* 1984, *80*, 135.

(21) Majjane, A.; Chahine, A.; Et-tabirou, M.; Echchahed, B.; Do, T.-O.; Breen, P. M. *Mater. Chem. Phys.* 2014, *143*, 779.

(22) Marković, N. M.; Schmidt, T. J.; Stamenković, V.; Ross, P. N. *Fuel Cells* 2001, *1*, 105.

(23) Lee, Y.; Suntivich, J.; May, K. J.; Perry, E. E.; Shao-Horn, Y. *The Journal of Physical Chemistry Letters* 2012, *3*, 399.

(24) Bard Allen J., F. L. R. *Electrochemical Methods: Fundamentals and Applications*; 2nd ed., 2001.